Summer 2024

DYNAMICS OF SEPARATED FLOWS IN DIFFUSERS WITH VORTEX GENERATORS

Sandeep Eldho James
University of Texas at Arlington

DYNAMICS OF SEPARATED FLOWS IN DIFFUSERS WITH VORTEX GENERATORS

by

SANDEEP ELDHO JAMES

Presented to the Faculty of the Graduate School of
The University of Texas at Arlington in Partial Fulfillment
of the Requirements
for the Degree of

DOCTOR OF PHILOSOPHY

THE UNIVERSITY OF TEXAS AT ARLINGTON

August 2024

Dedicated to my family.

ACKNOWLEDGEMENTS

I am profoundly grateful to my supervisors, Prof. Frank K. Lu and Prof. Liwei Zhang, whose exceptional guidance, unwavering support, and insightful feedback have been the cornerstone of my Ph.D. journey. Their dedication to mentoring and scholarly rigor have not only shaped this dissertation but also enriched my understanding in this area of research. I am thankful to them for the countless hours spent discussing ideas, reviewing drafts, and offering scholarly insights. I am deeply indebted to them for fostering an environment of intellectual curiosity and pushing me to achieve my best. I extend my sincere gratitude to my dissertation committee members: Prof. Zhen Xue Han, Prof. Ankur Jain and Prof. Habib Ahmari for their invaluable contributions to this research. Their meticulous attention to detail and constructive criticism have significantly enhanced the clarity, structure, and depth of this dissertation.

Financial support from the Department of Mechanical and Aerospace Engineering at UTA, through GTA positions, has played a crucial role in facilitating this research. I am deeply grateful for their commitment to supporting my academic endeavors, which has provided essential resources and opportunities to conduct thorough and impactful research. I extend my sincere appreciation to Prof. Lucca Maddalena and Prof. Vijay Gopal for selecting me as a GTA for the Aerodynamics and Fluids lab. Their support has been instrumental in advancing my academic and research pursuits.

I would like to express my sincere gratitude to my colleagues at the Aerodynamics Research Center Dr. Jiss J. Sebastian, Dr. Ananthkumar Jayamani, Mr.

Jayson Small and Mr. Himanshu Khatri, whose intellectual exchange, and unwavering support have created a stimulating academic environment. I am grateful for their encouragement, constructive feedback, and collaborative spirit, which have played a crucial role in shaping my research and giving me a sense of community. I am especially grateful to my friends, Dr. Jees Augustine, Dr. Abhishek Santra, Dr. Balan Ramesh, and Mr. Aby Cyriac, for their support, encouragement, and understanding, which have provided consistent strength throughout this challenging journey.

I owe an immense debt of gratitude to my parents, Mr. James A. J and Mrs. Elizabeth Paul, as well as to my brother, Dr. Sachin Paul James, and my sister-in-law, Dr. Maria K. Saji. Their support and sacrifices have been the foundation of my success. Their belief in my dreams and aspirations has fueled my determination and their relentless encouragement during moments of doubt has given me the strength to persevere.

To my dear wife, Jeena Kuriakose, your unwavering support, love, and understanding have been a constant source of strength and guidance throughout this challenging journey. Your belief in me, even during the most difficult times, has been a beacon of hope that kept me motivated and determined. I am deeply grateful for the countless sacrifices you have made, from late nights supporting my work to putting your own dreams on hold, all to see me succeed. I am thankful to have you by my side. I would also like to thank my daughter Rachel Eliza James, whose arrival has brought immense joy and motivation into my life. The delightful moments shared with you have provided me with the strength and inspiration needed to complete this dissertation.

July 16, 2024

ABSTRACT

DYNAMICS OF SEPARATED FLOWS IN DIFFUSERS WITH VORTEX GENERATORS

Sandeep Eldho James, Ph.D.

The University of Texas at Arlington, 2024

Supervising Professors: Frank K. Lu, Ph.D., P.E and Liwei Zhang, Ph.D.

Flow through curved diffusers is complicated due to the possibility of flow separation and secondary flows. Vortex generators (VGs) are a class of passive flow separation control devices used to improve the flow quality in curved diffusers by suppressing flow separation. However, the literature review demands an in-depth investigation on the physical mechanisms related to flow separation control. Thus, this study aims to improve the understanding of the underlying flow physics associated with VG-induced flow separation control in confined flows. The chosen geometry for this study is a well-documented asymmetric diffuser which exhibits a mild flow separation.

The theoretical formulation of this work is based on the three-dimensional, incompressible form of mass and momentum conservation equations, numerically solved across the computational domain using a finite-volume approach. The turbulence closure is achieved using two approaches: 1) SST $k-\omega$ based Reynolds-averaged Navier-Stokes (RANS) simulations and 2) dynamic Smagorinsky-Lilly model-based large eddy simulations (LES).

Firstly, a performance evaluation study was conducted using RANS approach. To suppress flow separation, improve pressure recovery and reduce distortion, different VG configurations were deployed upstream of the diffuser inlet. Analysis of skin friction lines in the downstream flowfield revealed various topological features, which helped identify separation and reattachment locations and determine the separation region size. The ramp-type VGs reduced the separation zone with increased total drag. While the upwash vanes consistently underperformed in distortion index across all cases, the downwash vanes with larger size decreased the distortion index without impacting total drag.

A pair of vanes that has demonstrated high performance was selected for further analysis using LES. Turbulence events at several probe locations close to the curved wall and the vertical centerline were analyzed using the normalized joint probability density functions. Under adverse pressure gradients, increased ejection and sweep events were detected near the trailing vortices. The heightened sweep events enhances momentum redistribution and energizes the near-wall flow to prevent flow separation. The trailing vortices from the VGs were visualized using iso-surfaces of the Q-criterion and streamlines on transverse planes. The downwash induced by the trailing vortices energized the near-wall flow, demonstrating a notable reduction in the separation region. By tracking the vortex size at various streamwise locations, a drastic increase in vortex size was detected, suggesting the onset of vortex breakdown. The breakdown location exhibited increased ejection and sweep events, velocity fluctuations, Reynolds stress, and turbulent kinetic energy (TKE) production. The peak TKE production shifted transversely and spanwise toward the high-momentum regions, aiding in the suppression of flow separation through enhanced momentum redistribution.

TABLE OF CONTENTS

LIST OF ILLUSTRATIONS

LIST OF TABLES

NOMENCLATURE

A	reference area for calculating drag parameter
C_D	$D \,/\, \frac{1}{2}\rho U^2 A$, drag coefficient
c_{f_x}	$\tau_{w_x} \,/\, \frac{1}{2}\rho U^2$, skin friction coefficient due to wall shear in the x direction
c_p	$(p - p_{ref}) \,/\, \frac{1}{2}\rho U^2$, pressure coefficient
CVP	counter-rotating vortex pair
D	drag
DI	$(p_{t,max} - p_{t,min})/p_{t,av}$, distortion index
F	force
H	half-height of the inlet channel
h	height of the vortex generator
l	length of the vortex generator
(N_x, N_y, N_z)	number of cells in the streamwise, wall-normal and spanwise direction
p	pressure
PFC	passive flow control
s	maximum spacing between vanes
U	average velocity at the inlet of the domain
VG	vortex generator
w	width of the vortex generator
(x, y, z)	streamwise, wall-normal and spanwise coordinates
α	half-opening angle of diffuser
δ	boundary-layer thickness
ΔC_D	$C_{D,VG} - C_{D,noVG}$, incremental change in drag coefficient of a control volume

$(\Delta x, \Delta y, \Delta z)$	computational cell sizes in the streamwise, wall-normal and spanwise direction
η	diffuser efficiency
μ	dynamic viscosity
ω_x	vorticity component in the x direction
Ω_x	normalized vorticity component in the x direction
Π	turbulent kinetic energy production
τ	shear stress

Subscripts

av	average value at a cross-plane
max	maximum value at a cross-plane
min	minimum value at a cross-plane
$noVG$	no vortex generator
p	pressure
ref	reference static pressure at $x = -3.4H$
t	total
VG	vortex generator
τ	shear

Superscripts

$\prime$	fluctuating quantity
$\bar{}$	mean quantity
$\sim$	filtered quantity

CHAPTER 1

INTRODUCTION

1.1 Background and Motivation

Flow separation is a phenomenon that occurs in both internal and external flows, triggered by an adverse pressure gradient along the streamwise direction. In external flows, such as on aircraft wings, flow separation can significantly reduce lift while increasing drag, a condition known as stall. Stall notably diminishes aerodynamic efficiency. Similarly, in power generation applications like wind turbines, mitigating flow separation is critical for enhancing performance. Flow separation is a serious concern in internal flows, such as those in aircraft inlets. Aircraft inlets, constrained by space limitations, may feature high divergence angles. These steep angles lead to severe adverse pressure gradients that can result in flow separation, poor pressure recovery, and heightened total pressure distortion. Since these inlet diffusers channel airflow to the compressor, the elevated total pressure distortion generates compressor loading non-uniformities. Additionally, the unsteadiness induced by flow separation can cause stalling or surging of the compressor. Figure. 1.1 [1, 2] shows the flow separation occurring within such an S-duct inlet, where the flow structures emanating from the separation point negatively impact compressor performance. The detrimental effects of flow separation in inlet diffusers are further discussed in McMartin et al. [8] and Nicoll et al. [9]. Moreover, severe turns, as commonly observed in heat exchangers, present another scenario where flow separation can degrade the device's performance. Given these adverse impacts, controlling flow separation is a critical topic in many flow applications.

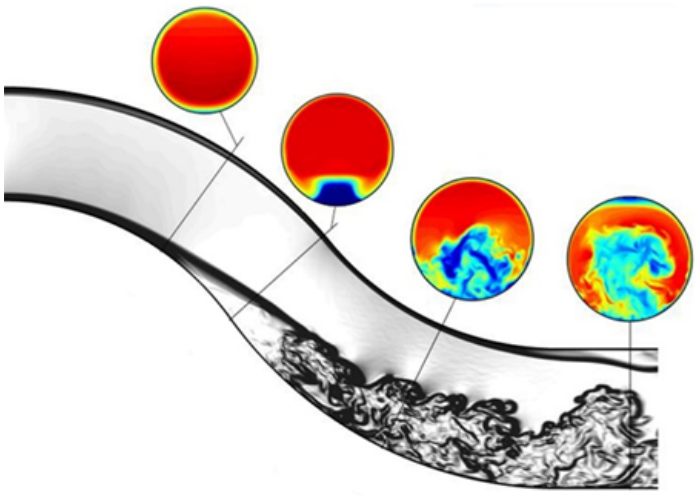

Figure 1.1: Flow separation in an S-duct geometry proposed by NASA [1, 2]

Among various flow separation control mechanisms, vortex generators are notable for their simplicity in design and ease of implementation, as well as their effective separation control capabilities. The trailing vortices shed from these devices play a pivotal role in strengthening the boundary layer, thereby suppressing flow separation. Given their practical importance, it is imperative to investigate the behavior of these trailing vortices under adverse pressure gradient conditions and to assess their impact on the separation region.

1.2 Literature Review

1.2.1 Flow Separation and Control

Flow separation control manipulates fluid flow for two primary objectives: enhancing aerodynamic surface performance and improving flow device functionality. The first objective involves reducing adverse effects, such as shifting the stall margin, delaying flow separation, and decreasing vibration. The second focuses on device performance, such as enhancing fluid mixing and augmenting heat transfer. This scientific domain, therefore, spans a broad spectrum of aerospace engineering, as discussed in reviews by Joslin and Miller [10] and Greenblatt et al. [11].

Based on the mode of operation, flow separation control methodologies are typically categorized as either active or passive. In active flow control (AFC), surface elements such as actuators are deployed to manipulate the flow. Other active techniques include suction, blowing, heating, and cooling. AFC may also involve energy deposition in the flow, usually through electromagnetic radiation. However, integrating such complex systems and equipment into aerodynamic surfaces is challenging due to the increased overall weight [11]. For instance, in high-lift aircraft wings, the added weight from AFC devices necessitates a more powerful propulsion system, further increasing the overall weight. According to Greenblatt et al. [11], the decision to deploy AFC is justified only when it provides a significant advantage over passive techniques.

Passive flow control (PFC) involves attaching small, low-drag elements to the surface. Common PFC devices include vortex generators (VGs), leading-edge slats, leading-edge serrations, riblets, boundary layer fences, and gurney flaps [12]. The principle behind PFC is to entrain high-momentum fluid in the freestream into the low-momentum region near the walls, thereby suppressing flow separation with min-

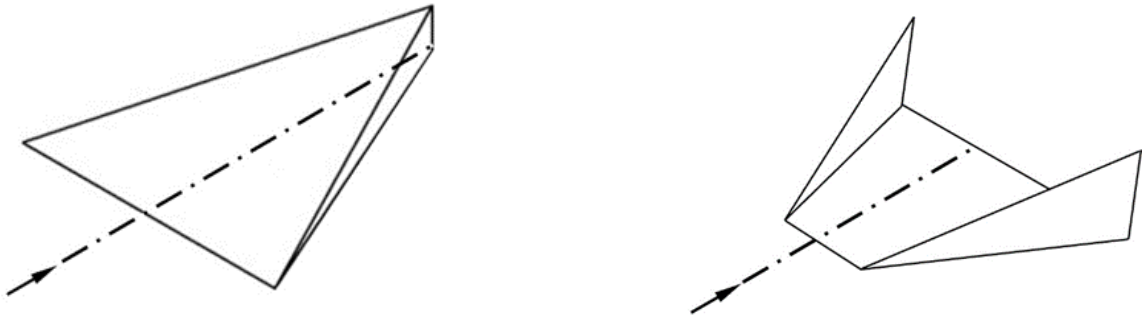

(a) Ramp-type [14] (b) Vane-type [3]

Figure 1.2: Commonly used VGs

imal performance penalty. PFC is a favored approach for both external and internal flows. Despite its maturity, ongoing research aims to further understand and enhance various PFC devices. For example, VGs, typically deployed in arrays on aero/hydrodynamic surfaces, are used to reduce or eliminate flow separation, enhance fluid mixing, or augment heat transfer. Ramp- and vane-types are among the commonly used VGs [13], illustrated in Fig.1.2. Of these, vane-type VGs are often preferred for their lower parasitic drag and blockage. These vanes, either constant or tapered chords, are mounted at an angle to the incoming flow and can be arranged to produce co-rotating or counter-rotating vortices, which generate either downflow or upflow in the region between the vanes. The subsequent section provides a literature review on the theoretical basis and applications of these techniques in various flow environments

1.2.2 Vortex Generators

The simplicity of design and implementation, along with effective flow separation control capabilities, have established VGs as practical options for flow control applications. The primary motivation for employing VGs is to delay or prevent flow separation. This action helps reduce drag, enhance pressure recovery and minimize flow distortions, depending on the specific application. VGs have been installed or suggested for various external flows, including aircraft wings [15, 16], fuselage tails [17, 18], rotor blades [19], and wind turbine blades [20] to mitigate separation in adverse pressure gradients at low speeds. The goals often include reducing drag or vibrations. Figure 1.3 shows the flow separation control achieved on a NACA 63-621 airfoil at a ten-degree angle of attack, with an array of vane-type VGs deployed over half of the airfoil span. The flow visualization clearly shows suppressed separation in the section of the airfoil equipped with VGs. VGs have also been employed in front of cockpits to reduce airframe noise by minimizing the separation bubble at the nose/cockpit intersection [21, 22, 23]. Furthermore, they are used ahead of tank pressure equalization ports on the underside of wings to abate airport noise [23]. A brief review of VGs implemented for internal flows will be discussed later. Given their broad applicability and the complex flow dynamics they influence, it is essential to explore the underlying physics of VG-induced flow separation control.

One of the flow phenomena induced by VGs is the counter-rotating vortex pair (CVP) emanating from the VGs, which bears an analogy to the wing tip vortices shed from an aircraft wing [24]. Figure 1.4a [25, 26] shows a pair of CVP generated by closing a pair of computer-controlled flaps. The CVP was then allowed to impinge on a wavy wall. Morris et al. [25, 26] used this experiment to study the ground effect of wing tip vortices. Figure 1.4b shows the wing tip vortices emanating from an

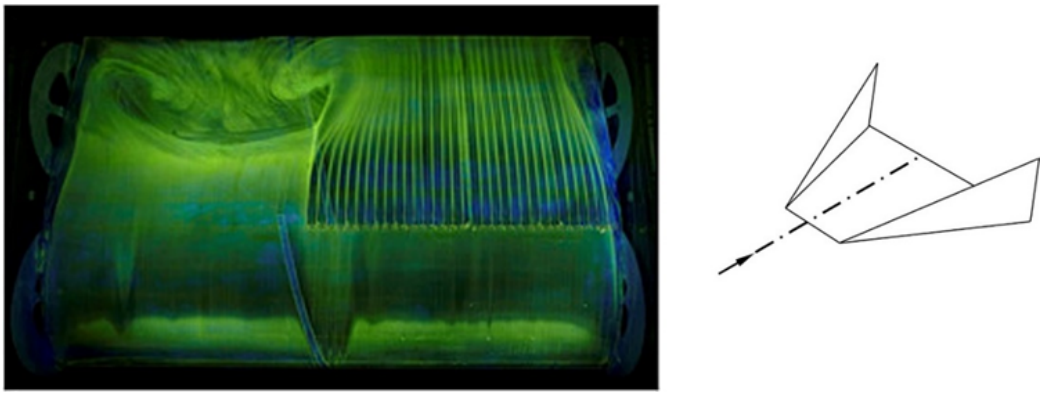

Figure 1.3: Flow separation control on NACA 630621 airfoil using VGs [3]

aircraft wing. The theoretical basis of CVPs can be traced to the Kelvin-Helmholtz vorticity theorems as exemplified in lifting-line theory [27]. The vorticity contained in the incoming boundary layer can be modeled as a vortex filament. When the flow confronts a VG, this vortex filament wraps around it to form the CVP. These streamwise CVPs, along with their co-rotating counterparts, are known to enhance mixing [28], and are utilized in various applications as mentioned above. The relative proximity of the vortices in the CVP, along with their strength and trajectory, are some of the critical parameters that govern the mixing enhancement. The investigation conducted by Park et al. [29] showed that by changing the taper angle of the VGs, the abovementioned parameters can be modified to improve mixing. The improved mixing promotes the redistribution of momentum between the fast- and slow-moving regions in the flowfield. Although these streamwise vortices are stubborn flow features, they eventually break down into smaller-scale motions and turbulence, even in zero pressure gradient conditions [30].

The enduring nature and the subsequent breakdown of streamwise vortices [31], render them particularly beneficial for applications aimed at delaying flow separation or enhancing flow properties such as mixing. These observations suggest that embed-

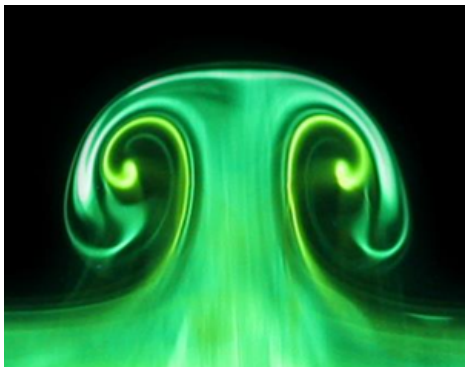

(a) CVP near a wall [25, 26]

(b) Wing tip vortices

Figure 1.4: Similarity of CVP with wing tip vortices

ding streamwise vortices in a boundary layer, especially in diffusers, can be beneficial to delay or prevent flow separation. The streamwise vortices emanating from VGs were first used in diffusers by H.D. Taylor in the late 1940s to eliminate flow separation.[1] A subsequent study by Schubauer and Spangenberg [32] on PFC devices, which they referred to as mixing devices, showed that these devices enhance the momentum of the near-wall fluid through large-scale mixing in both zero and adverse pressure gradient boundary layers. This increased momentum makes the flow more resistant to separation under adverse pressure gradients. The streamwise CVP is widely recognized for improving mixing by entraining freestream momentum into the near-wall region. This entrainment revitalizes the boundary layer, thus delaying the onset of separation. VGs are employed in both external and internal flows. For external applications, the height of VGs, h, is typically just above the boundary-layer thickness δ.

[1] Taylor, H. D. "The Elimination of Diffuser Separation by Vortex Generators," Research Department Report No. R-4012-3, United Aircraft Corporation, East Hartford, Connecticut, 1947.

— "Application of Vortex Generator Mixing Principles to Diffuser," Research Department Concluding Report No. R-15064-5, United Aircraft Corporation, East Hartford, Connecticut, 1948.

— "Summary Report on Vortex Generators," Research Department Report No. R-05280-9, United Aircraft Corporation, East Hartford, Connecticut, 1950.

However, sub-boundary-layer VGs, commonly termed micro vortex generators, have also been effective [14]. Ichikawa et al. [33] found vanes with a height of 9.6δ to be effective, though they noted that the most effective vanes were only half that height.

Depending on the arrangement of VGs, CVPs can induce either downflow or upflow [34, 35, 36]. Additionally, some VGs alignments facilitate the creation of co-rotating vortices. A notable optimization study by Godard and Stanislas [37] compared VG-induced co- and counter-rotating vortices, finding that counter-rotating setups are twice as effective as co-rotating ones in reducing wall shear stress. This study also concluded that triangular vanes outperform rectangular vanes in both vortex strength and drag reduction, with an optimum angle of attack of 18 degrees for the blades, aligning with findings by Pauley and Eaton [36]. Despite the size and arrangements of the VGs, the CVPs they induce are part of a broader family of horseshoe vortices shed from protuberances, a subject that has been extensively studied [38, 39, 40, 41]. VGs are effectively designed protuberances aimed at achieving low drag and high circulation [30]. Early analyses of CVPs-induced flow employed concepts similar to lifting-line theory in aerodynamics [42, 43, 44]. The influence of the wall was accounted for using the method of images [45]. However, experimental observations did not confirm the inviscid model predictions of CVP trajectories deviating from the surface.

A pseudo-viscous model that reproduced the experimental trajectories of CVP was proposed by Lödgberg et al. [34]. The model employs an empirical expression to gradually diminish vortex strength with increasing downstream distance. Despite this attenuation, experiments showed that vortex cores were detected nearly $300h$ downstream, highlighting their resilience against viscous damping. This persistence, particularly their proximity to the surface up to $500h$ downstream from the VGs, underscores their potential utility in flow control applications. The authors pointed out

that while VGs enhance surface adherence and vortex persistence, they also introduce a tradeoff by increasing drag. They recorded a spanwise-averaged skin friction coefficient that remained elevated beyond the natural flow values up to 300h downstream from the VGs, translating to increased drag on a flat plate. Although undesirable in well-behaved flows, this increase can be beneficial in preventing flow separation in external flows, potentially reducing overall drag. Nevertheless, the implications for internal diffuser flows require further investigation, suggesting a possible limitation of VGs in these contexts.

As the CVP advances into an adverse pressure gradient region, the stream surface enclosing the vortex suddenly retards and diverges, a phenomenon commonly referred to as vortex breakdown [46, 47]. Preliminary evidence of vortex breakdown was obtained during an investigation conducted by Peckham and Atkinson [48] on the flow over highly swept wings at high angles of attack. Depending on the flow conditions, Sarpkaya [49] and Faler et al. [50] observed various modes of vortex breakdown, including spiral, bubble, and double helix. Figure 1.5 shows the visualization of different vortex breakdown modes. In a spiral breakdown, as shown in Fig. 1.5a, the vortex filament undergoes sudden stagnation, which results in the formation of kinks. These kinks then rotate with the vortex and subsequently break down into turbulence. Figure 1.5b shows the bubble breakdown, which is a severe form of breakdown. In this case, an abrupt stagnation is observed in the vortex trajectory, followed by the bulging of the vortex to form a bubble-like structure. Bubble breakdown is also known as axisymmetric breakdown due to the axisymmetric nature of the bubble structure [49, 51]. Unlike the spiral and bubble breakdown, the double-helix breakdown mode may not have a stagnation point. The structure resembles two strings emanating from the vortex to form a helical shape. The structure of a double helix

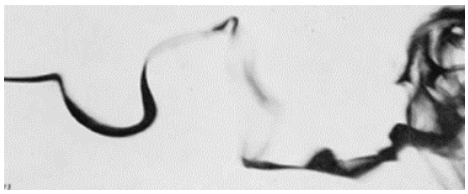

(a) Spiral breakdown [52]

(b) Bubble breakdown [53]

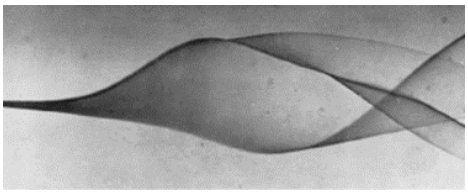

(c) Double-helix breakdown [52]

Figure 1.5: Modes of vortex breakdown

vortex breakdown is shown in Fig. 1.5c. Sarpkaya noted that the double-helix mode is extremely sensitive to upstream and downstream disturbances [49].

The prospect of vortex breakdown depends on the severity of adverse pressure gradients caused by geometric changes such as channel divergence. Beyond a certain degree of divergence, the adverse pressure gradient becomes strong enough to induce flow separation. In these instances, the separation streamlines act like a wall, albeit with less divergence than the physical wall. The perceived divergence by the flow upstream reduces the impact of the adverse pressure gradient on the CVP, potentially avoiding vortex breakdown [53]. In cases of mild separation, however, the separation streamlines may not significantly affect the breakdown of the CVP. Comprehensive reviews of the vortex breakdown phenomenon were provided Lucca-Negro et al. [52] and by Délery [54].

Another mechanism responsible for vortex breakdown is the swirling motion of the vortex. At a high degree of swirl, the tangential velocity of the vortex is significantly higher than its axial velocity. As a result, the vortex tends to diverge from its original shape and eventually breaks down. According to Hall et al. [46],

a high centrifugal force caused by swirling motions can induce vortex breakdown. The swirl-induced vortex breakdown is usually observed in applications with varying degrees of swirl. This scenario can be seen when the vortices generated using a swirl generator are used for flame stabilization in furnaces and combustion chambers. Similar applications of confined vortices in different flow machinery is detailed in the study by Escudier [55]. Note that, in such cases, a breakdown can occur even without an adverse pressure gradient.

As mentioned in the previous discussions, the VG-induced CVPs can be used to suppress or delay flow separation in both internal and external flows. The subsequent sections include a comprehensive discussion on the application of VG-induced CVPs in controlling flow separation and improving the performance of diffusers.

1.2.3 Diffuser Flows

Diffusers are flow devices used extensively to decelerate fluid flow and raise static pressure, a process termed "pressure recovery". They play a pivotal role in turbomachinery. During the diffusion process, an adverse axial pressure gradient is present, heightening the risk of flow separation even in well-designed diffusers. This susceptibility can be exacerbated by changes in operating conditions. Further, exceptional scenarios necessitate deviation from these norms. Such cases include wide-angle diffusers as shown in Fig. 1.6, installation at bends, configurations in densely packed turbomachinery, and S-duct diffusers in airbreathing engines inlets. In these cases, the flow undergoes significant distortion and compromised pressure recovery.

To obtain the desired performance, diffusers are engineered to abide by rigorous standards tailored to their specific applications. Schlichting [56] summarized data from various sources, demonstrating that the efficiency of both straight and curved conical diffusers is heavily influenced by the angle of divergence and the thickness

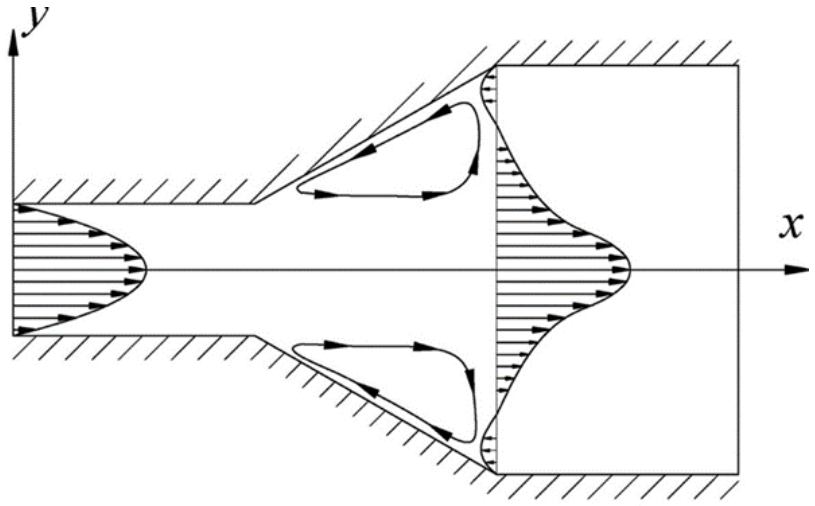

Figure 1.6: Schematic of flow through a wide-angle diffuser [4]

of the incoming turbulent boundary layer. They noted that the optimum half-angle for diffuser efficiency is narrowly confined to a range of $\alpha = 2- 8$ deg. Additionally, performance is strongly dependent on the ratio of the boundary layer displacement thickness to the diffuser entry diameter, denoted as δ^*/D_1. When this ratio and α are small, diffuser efficiency can reach as high as 0.9. However, achieving high efficiency is challenging due to the stringent requirement of a small half-angle. In many practical applications, space constraints necessitate wide opening angles or the use of curved or asymmetrical diffusers. Schlichting's data indicated that efficiency dropped to about 55% and 50% for curved diffusers with $\alpha = 7.5$ and 15 degrees, respectively, and accompanied by thick boundary layers, where $\delta^*/D_1 \approx 0.02$

Various reasons are attributed to the poor performance of wide-angled and asymmetrical diffusers. One is the flow separation, which is often caused by the severe adverse pressure gradient at a large divergence angle. Figure 1.7 shows the flow separation in a serpentine diffuser. Sovran and Klomp [57], citing Kline et al. [58], presented flow-regime charts for two-dimensional, conical, and annular diffusers. Specifically for two-dimensional diffusers, they identified four possible flow regimes:

1) attached flow, 2) mild stall, 3) large transitory stall, and 4) jet formation. These regimes depend on the half-angle and the ratio of the diffuser length to the inlet width in the diverging direction. The transition from attached flow to stall is gradual, a characteristic Sovran and Klomp found noteworthy for certain diffuser applications. Similar trends were observed in conical diffusers by McDonald and Fox [59]. A comprehensive collection of diffuser data, which is beneficial for design consideration, is available in several studies [60, 61, 62, 63, 64]. For design purposes, it is crucial to predict whether boundary-layer separation will occur in a diffuser.

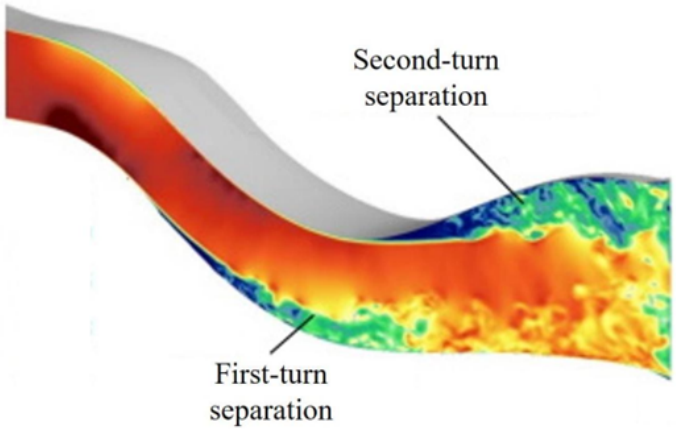

Figure 1.7: Flow separation in a serpentine diffuser [5]

Several methods for identifying flow separation in diffusers have been proposed. Sandborn and Kline [65] suggested that the boundary-layer shape factor at the intermittent transitory detachment (ITD) location, which is situated just upstream of the separation location, behaves in accordance with

$$\equiv \frac{\delta^*}{\theta} = 1 + \left(1 - \frac{\delta^*}{\delta}\right)^{-1} \tag{1.1}$$

where the flow was reversed 20% of the time [66]. Subsequently, Kline et al. [67] showed that $H = 2.7$ and 4 at the ITD and the fully separated location, respectively.

Since flow separation is triggered by an adverse pressure gradient, Castillo et al. [68] simplified the above relationship to $H = 2.76 \pm 0.23$, which is in close agreement with the ITD, and proposed a separation criterion

$$\Lambda_\theta \equiv \frac{\theta}{\rho U_\infty^2 d\theta/dx} \frac{dp_\infty}{dx} = 0.21 \pm 0.01 \tag{1.2}$$

For practical purposes, these criteria provide useful guidance in diffuser design by highlighting the potential for separation, thereby enhancing overall diffuser performance.

Another phenomenon affecting diffuser performance is the secondary flow, which occurs due to the streamline curvature during a turn in the diffuser. Figure 1.8 shows the secondary flow pattern in a curved channel. Turns are frequently necessitated by space constraints in applications such as turbomachinery or industrial ducting. The head losses associated with turns have been extensively studied in piping design [69]. Flow through the S-duct diffuser showcases the combined effect of adverse pressure gradient and streamline curvature affecting the flow quality [70]. The severe curvature of S-duct diffusers results in high centrifugal force acting in the wall-normal direction, resulting in a crossflow. The term "secondary flow" is also used interchangeably with "crossflow" to describe this phenomenon. When the flow encounters a curved surface, the presence of crossflow along with the streamwise flow results in the formation of Görtler vortices [71]. The studies conducted by Bandyopadhyay et al. [70] and Lopes et al. [72] confirmed the presence of Görtler vortices in S-duct diffusers. In addition to the crossflow, the adverse pressure gradient in the S-duct diffuser leads to flow separation. The crossflows, along with flow separation in S-duct diffusers, introduce additional flow distortion. Sovran et al. [57] found that S-duct diffusers experience

exacerbated losses if they are wide-angled or have a rectangular cross-section, which intensifies distortion from secondary corner flows [73].

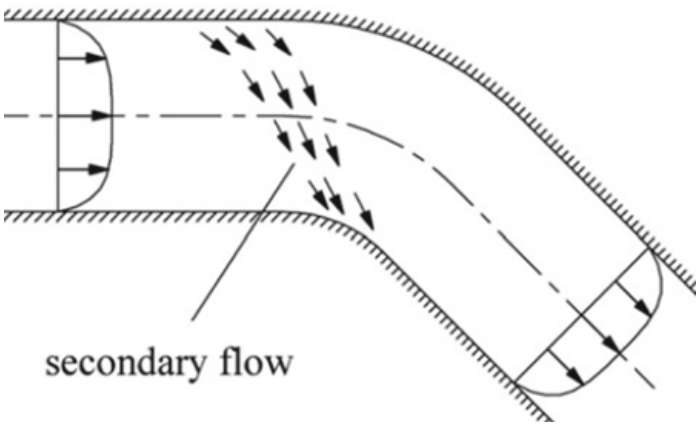

Figure 1.8: Secondary flow pattern in a curved channel [6]

To enhance performance, the flow within S-duct diffusers should be improved. One approach is to install VGs either before or directly within the turn. VGs improve the diffuser performance by diminishing or preventing flow separation in such challenging environments. For internal flows, VGs have been effectively utilized in inlet diffusers to optimize airflow into engines [74, 75, 76, 77] and on compressor cascades [78], as shown in Fig. 1.9.

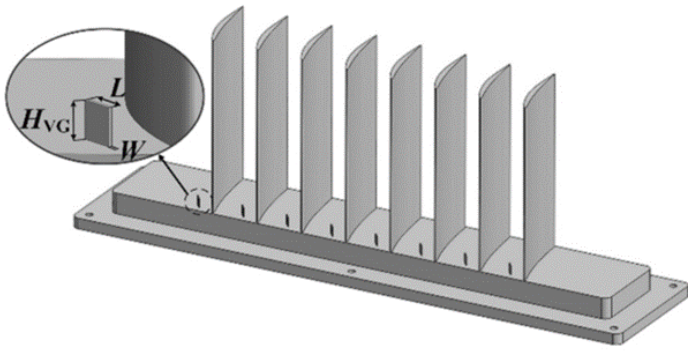

Figure 1.9: VGs deployed in a compressor cascade to avoid corner separation [7]

Several investigations have been conducted to study the performance enhancement of S-duct diffusers using VGs. The study by Reichert and Wendt [79] examined 20 configurations of co- and counter-rotating VG arrays in a diffusing S-duct with a circular section. They explored both wishbone and tapered-fin type VGs and found that the latter significantly improved pressure recovery, reducing distortion by up to 50%. They attributed the enhanced aerodynamic performance not to the re-energization of the boundary layer by axial vortices but rather to the effective suppression of detrimental crossflows through flow redirection. To investigate the effects of crossflows, Sullerey et al. [80] introduced fences along the curved sections of an S-duct diffuser with a rectangular cross-section. These fences, long thin barriers with a height of 1.2δ and fixed length, were installed in configurations ranging from one to four fences. The study also included experiments with wishbone and tapered-fin type VGs. Similar to findings by Reichert and Wendt, tapered-fin VGs outperformed wishbone. However, fences yielded superior performance compared to tapered-fin VGs in diffusers with larger radius ratios, defined as the ratio of the centerline radius to the half-width (or radius) of the duct.

Similar to conventional VGs, various arrangements of low-profile VGs, also known as submerged or micro VGs, were found to improve the flow in a rectangular S-duct diffuser. In a study by Paul et al. [81], a pair of triangular vanes, with their trailing edges spaced further apart than the tips, a configuration recommended by Velte et al. [82] and Godard and Stanislas [37] for wing applications was used. This geometry directed the flow downward between the CVPs. As discussed earlier, VGs are believed to entrain high-momentum freestream into the low-momentum wall region through streamwise vortices, resulting in a reduced separation and increased pressure recovery. The study reported a 27% improvement in static pressure recovery and a 14% reduction in total pressure loss with the optimal configuration. Addi-

tionally, the distortion index improved by 27%, compared to Sullery et al.'s result of 9% [83]. The authors also noted that these low-profile VGs reduced crossflow and decreased the momentum thickness at the exit plane, along with a reduction in the separation zone.

Another scenario that demonstrates the combined effect of adverse pressure gradient and curvature is the intermediate turbine ducts. Future designs of large turbofans often include an intermediate turbine duct that features a pronounced turn between the high and low-pressure turbines. This design choice, aimed at reducing weight, size, and cost reasons, results in a complex flowfield characterized by separation and crossflows within the duct. Santner et al. [84] introduced an array of low-profile VGs to mitigate these issues, drawing on results mainly obtained from two-dimensional external flows without crossflows [14, 83]. They also studied a simplified S-shaped rectangular duct with strong curvature under high subsonic Mach number and steady inflow conditions, where they noted contradictory results: while the simplified configuration showed reduced flow separation and improved pressure recovery, the actual configuration did not exhibit a decrease in the separation zone, and even displayed increased losses. The researchers speculated that the wakes from upstream high-pressure blades might hinder the development of streamwise vortices from the VGs, and strong tip leakage could further diminish VG performance. Despite the ineffectiveness of low-profile VGs in this specific context, they proved beneficial in other applications, particularly where the diffuser is positioned upstream of the turbomachinery. Santner et al. suggested that further studies should consider an annular duct with an unsteady inflow to further understand these dynamics.

An extreme example of a curved diffuser is one that makes a right-angle turn, as often encountered in closed-circuit wind tunnels. These setups, due to their stringent flow quality requirement, necessitate meticulous consideration of crossflow distortion.

In a related study, Chong et al. [85] assessed the effectiveness of VG arrays, guide vanes, honeycombs, and screens in managing airflow in bare diffusers. Their findings indicated that VG arrays were generally ineffective in the presence of significant centrifugal forces, showing no substantial improvement in reducing or eliminating separation zones during severe turns.

1.3 Objectives and Literature Contributions

1.3.1 Objectives and Outline of Dissertation

The review above indicates that VGs are well established. However, their applications to curved diffusers is challenging. Thus, understanding the flow physics and performance of VGs in a simpler geometry with slight separation is crucial. The chosen geometry for this study is a welldocumented asymmetric diffuser exhibiting mild flow separation [86, 87]. Many researchers have used an asymmetric diffuser with mild separation to investigate incipient separation conditions [88, 89, 90]. This numerical study examines the effect of two families of vanes and a swept ramp. The VGs are placed upstream of the diffuser, and the downstream flowfield is analyzed through skin friction topology to identify different flow features. Subsequently, performance parameters such as overall drag, pressure recovery, and flow distortion are presented and discussed.

A pair of VGs that has demonstrated effective performance-namely, reduction in separation region, improvement in pressure recovery, and reduction in distortion index are selected for further analysis. The flowfield downstream of the VGs is studied using large eddy simulations to gain insights into the underlying flow physics of flow separation control. Two modes of momentum transfer are identified: 1) downwash from the trailing vortices shed by the VGs and 2) an increase in velocity fluctuation due to the breakdown of the trailing vortices. From the literature review shown above, the effect of vortex breakdown on flow separation control has been relatively unexplored. This study aims to detect vortex breakdown and analyze its associated effects, such as the increase in turbulent kinetic energy production.

The work is organized into six chapters. Chapter 2 covers the theoretical formulation and discusses the turbulence closure methods adopted in this study. Chapter

3 focuses on the numerical methods, including the finite volume approach, gradient evaluation schemes, evaluations of inviscid and viscous fluxes, temporal discretization, and boundary conditions. The results from the performance evaluation study are presented in Chapter 4. Chapter 5 elaborates on the detection of vortex breakdown and its impact on flow separation control. Finally, Chapter 6 provides a summary of the work and offers recommendations for future research.

1.3.2 Literature Contributions

The present work has resulted in the following contributions to the literature.

- James, S.E. and Zhang, L., Lu, F.K., "Flowfield Downstream of a Vane-Type Vortex generator in an Asymmetric Diffuser." (In progress).
- Lu, F.K., James, S.E. and Zhang, L., 2023. "Flow Separation Control and Performance Evaluation of an Asymmetric Diffuser Using Vortex Generators." Aerospace Science and Technology, 136, p.108237. https://doi.org/10.1016/j.ast.2023.108237.
- James, S.E., Zhang, L. and Lu, F.K., 2022."Flow Separation Control and Drag Reduction in an Asymmetric Diffuser Using Vortex Generators," AIAA 2022-1067, AIAA SciTech Forum, January 2022. https://doi.org/10.2514/6.2022-1067
- James, S.E., Zhang, L. and Lu, F.K., 2021. "Numerical Study of Drag Reduction by Conventional and Micro Vortex Generators," AIAA 2021-2857, AIAA Aviation Forum, August 2021. https://doi.org/10.2514/6.2021-2857

CHAPTER 2

THEORETICAL FORMULATION

2.1 Governing Equations

Fluid flow is governed by conservation equations encompassing mass, momentum, and energy. The current investigation focuses on incompressible flows. The theoretical formulation is based on the incompressible form of mass and momentum conservation equations in the Cartesian coordinate system, which are as follows:

$$\frac{\partial u_j}{\partial x_j} = 0 \tag{2.1}$$

$$\frac{\partial u_i}{\partial t} + u_j \frac{\partial u_i}{\partial x_j} = \frac{1}{\rho}\left(-\frac{\partial p}{\partial x_i} + \frac{\partial \tau_{ij}}{\partial x_j}\right) \tag{2.2}$$

where $i(= 1, 2, \text{ and } 3)$ is the spatial coordinate index and $j(= 1, 2, \text{ and } 3)$ is the dummy index to spatial coordinate. The incompressibility assumption decouples the energy equation which is not required to solve the flow. The velocity component along the Cartesian coordinate direction x_i is denoted as u_i and the viscous stress tensor is denoted as τ_{ij}. The equations above can be written in vector form as follows:

$$\frac{\partial \vec{Q}}{\partial t} + \frac{\partial\left(\vec{E} - \vec{E}_v\right)}{\partial x} + \frac{\partial\left(\vec{F} - \vec{F}_v\right)}{\partial y} + \frac{\partial\left(\vec{G} - \vec{G}_v\right)}{\partial z} = 0 \tag{2.3}$$

where the terms $\vec{Q}, \vec{E}, \vec{F}$, and $\vec{G}$ are the inviscid fluxes and $\vec{E}_v, \vec{F}_v$, and $\vec{G}_v$ are the viscous fluxes. The expressions of these terms differ depending on the turbulence closure methods chosen. The details are explained in the subsequent sections and in Chapter 3, section 3.1.

2.2 Turbulence Closure

Turbulent flows exhibit flow structures characterized by diverse lengths and time scales. In turbulent flows, the largest structures have a characteristic length corresponding to the geometry involved. These structures are inherently unstable and eventually disintegrate, transferring their turbulent kinetic energy to smaller structures. This energy transfer process is referred to as energy cascading. Below a certain length scale known as the Taylor microscale, the viscous dissipation starts to become dominant [91, 92]. The cascading mechanism persists until, at the smallest scale, the turbulent kinetic energy contained in the eddies is dissipated to internal energy due to viscous action [93]. These smallest scales of flow structures are recognized as the Kolmogorov scale. The length and time scales of small eddies are dependent on the Reynolds number. The smallest scales become finer as the Reynolds number increases. The turbulence treatment methods applied in the current study are detailed in the subsequent sections.

2.2.1 Reynolds-Averaged Navier-Stokes (RANS) Equations

One of the characteristics of turbulent flows is the spatial and temporal fluctuations. To analyze turbulent flows, the fluctuating components of the flow variables are separated from their mean using Reynolds decomposition, where the instantaneous velocity $u_i(\vec{r}, t)$ is decomposed as

$$u_i(\vec{r}, t) = \bar{u}_i(\vec{r}) + {u_i}'(\vec{r}, t) \tag{2.4}$$

where $\bar{u}_i(\vec{r})$ is the mean velocity and ${u_i}'(\vec{r}, t)$ is the fluctuating velocity. Note that both the instantaneous velocity and the fluctuating velocity are functions of space $\vec{r}$ and time t.

Applying Reynolds decomposition to Eq. 2.1 and Eq. 2.2 yields the incompressible form of the Reynolds-averaged continuity and momentum equations as

$$\frac{\partial \bar{u}_j}{\partial x_j} = 0 \tag{2.5}$$

$$\frac{\partial \bar{u}_i}{\partial t} + \bar{u}_j \frac{\partial \bar{u}_i}{\partial x_j} = \frac{1}{\rho}\left(-\frac{\partial \bar{p}}{\partial x_i}\delta_{ij} + \frac{\partial \bar{\tau}_{ij}}{\partial x_j} - \rho \frac{\partial \left(\overline{u_i' u_j'}\right)}{\partial x_j} \right) \tag{2.6}$$

The overbar indicates time-averaged, and the prime indicates the fluctuating component.

The averaging process used in the RANS approach results in an additional term known as the Reynolds stress tensor $\left(-\rho\overline{u_i' u_j'}\right)$, which is a symmetric tensor with six individual stress components known as Reynolds stresses. The diagonal terms of this tensor represent the normal stresses, and the off-diagonal terms represent the shear stresses. The Reynolds stresses lead to an unbalanced set of equations to be solved for the flow field. One approach to resolve this issue is to model the Reynolds stress term using a turbulence model.

In the present study, the $\kappa - \omega$ SST (shear stress transport) model [94], falling under the eddy viscosity category, is utilized. The baseline forms of the $\kappa - \omega$ and SST $\kappa - \omega$ models were introduced as modifications to the $\kappa - \epsilon$ model. Notably, the $\kappa - \epsilon$ model encountered accuracy issues in predicting flow separation. To address this, a baseline version of the $\kappa - \omega$ model was introduced, wherein the $\kappa - \omega$ formulation was applied in the near-wall region, while the $\kappa - \epsilon$ model was employed for cells away from the wall. A hyperbolic tangent blending function was implemented to facilitate a seamless transition between the $\kappa - \omega$ and $\kappa - \epsilon$ models.

In validation studies, it was observed that the baseline $\kappa - \omega$ model exhibited sensitivity to freestream values of ω, resulting in a high wall shear stress compared to

experimental values. This elevated wall shear stress hindered the accurate prediction of flow separation from a smooth surface. To address this challenge, a modification was introduced by incorporating a viscosity limiter, leading to the development of the SST $\kappa - \omega$ model. The viscosity limiter, implemented as a hyperbolic tangent function of the distance from the nearest wall, played a crucial role. In regions near a wall, the limiter adeptly curtailed the eddy viscosity, resulting in a reduction of wall shear stress. This adjustment contributed to a more accurate prediction of flow separation, rectifying the issues encountered with the baseline $\kappa - \omega$ model.

The transport equations for the $\kappa - \omega$ SST model are

$$\frac{\partial k}{\partial t} + u_i \frac{\partial k}{\partial x_i} = \frac{1}{\rho}\left[\frac{\partial}{\partial x_i}\left(\Gamma_k \frac{\partial k}{\partial x_j}\right) + \tilde{G}_k - Y_k + S_k\right] \tag{2.7}$$

$$\frac{\partial \omega}{\partial t} + u_i \frac{\partial \omega}{\partial x_i} = \frac{1}{\rho}\left[\frac{\partial}{\partial x_i}\left(\Gamma_\omega \frac{\partial \omega}{\partial x_j}\right) + G_\omega - Y_\omega + D_\omega + S_\omega\right] \tag{2.8}$$

The effective diffusivities are modeled as

$$\Gamma_k = \mu + (\mu_t / Pr_k) \tag{2.9}$$

$$\Gamma_\omega = \mu + (\mu_t / Pr_\omega) \tag{2.10}$$

where μ_t is the turbulent viscosity, Pr_k and Pr_ω are the turbulent Prandtl numbers corresponding to k and ω. The production and dissipation terms of k and ω are defined as

$$\tilde{G}_k = \min\left(G_k, 10\rho\beta^* k\omega\right) \tag{2.11}$$

$$G_\omega = \tilde{G}_k \left(\alpha / v_t\right) \tag{2.12}$$

$$Y_k = \rho\beta^* k\omega \tag{2.13}$$

$$Y_\omega = \rho\beta\omega^2 \tag{2.14}$$

where G_k is the turbulence production in the standard $\kappa - \omega$ model, ρ is the density, α is the damping coefficient for turbulent viscosity, β^* and β are constants. The cross-diffusion term in the transport equation for ω is defined as

$$D_\omega = 2.336\rho\,(1 - F_1)\,\frac{1}{\omega}\frac{\partial k}{\partial x_j}\frac{\partial \omega}{\partial x_j} \tag{2.15}$$

where F_1 is a blending function used to blend the standard $\kappa - \omega$ model and the standard $\kappa - \varepsilon$ model. The source terms S_k and S_ω takes any user-defined form depending on the nature of the problem.

Recollecting Eq. 2.3, the inviscid and viscous flux terms involved in the above-mentioned RANS approach are listed below.

$$\begin{aligned}
\vec{Q} &= (0, \bar{u}, \bar{v}, \bar{w}, k, \omega)^T \\
\vec{E} &= \left(\bar{u}, \bar{u}^2 + \bar{p}/\rho, \bar{u}\bar{v}, \bar{u}\bar{w}, uk, u\omega\right)^T \\
\vec{F} &= \left(\bar{v}, \bar{u}\bar{v}, \bar{v}^2 + \bar{p}/\rho, \bar{v}\bar{w}, vk, v\omega\right)^T \\
\vec{G} &= \left(\bar{w}, \bar{u}\bar{w}, \bar{v}\bar{w}, \bar{w}^2 + \bar{p}/\rho, wk, w\omega\right)^T \\
\vec{E}_v &= (0, \bar{\tau}_{xx}, \bar{\tau}_{yx}, \bar{\tau}_{zx}, k_{xx}, k_{yx}, k_{zx}, \omega_{xx}, \omega_{yx}, \omega_{zx})^T \\
\vec{F}_v &= (0, \bar{\tau}_{xy}, \bar{\tau}_{yy}, \bar{\tau}_{zy}, k_{xy}, k_{yy}, k_{zy}, \omega_{xy}, \omega_{yy}, \omega_{zy})^T \\
\vec{G}_v &= (0, \bar{\tau}_{xz}, \bar{\tau}_{yz}, \bar{\tau}_{zz}, k_{xz}, k_{yz}, k_{zz}, \omega_{xz}, \omega_{yz}, \omega_{zz})^T
\end{aligned} \tag{2.16}$$

2.2.2 Large Eddy Simulation (LES)

In the analysis of turbulent flows, LES remains a prominent method. In this approach, the large three-dimensional structures are explicitly resolved, while the smaller eddies are separated using a spatial filter and are modeled to capture their effect. Due to its capability to resolve threedimensional fluid motion, LES is a widely accepted method to extract the underlying flow physics in many applications.

2.2.2.1 Filtering Operation

A filter is employed to decompose the velocity field. The filter width is proportional to the grid size. This decomposition results in two components: a filtered velocity field and a residual velocity field. The filtered velocity field, being three-dimensional and time-dependent, captures the motion of large-scale structures within the flowfield. The eddies that traverse through the filter are then modeled using subgrid-scale (SGS) models. The general filtering operation used in LES is defined by

$$\tilde{\varphi}(x) = \int_D \varphi\left(x'\right) F\left(x, x'\right) dx' \tag{2.17}$$

The symbol $\tilde{\varphi}$ and φ in Eq. 2.17 represent the filtered and unfiltered flow variables, respectively. Note that the filter F is applied throughout the fluid domain D, and hence, the integration in Eq. 2.17 is performed on the entire computational domain.

In the finite volume approach used in the present study (discussed in the next chapter), the filtered flow variables can be represented as

$$\tilde{\varphi}(x) = \frac{1}{\Delta V} \int_{\Delta V} \varphi\left(x'\right) dx' \tag{2.18}$$

where ΔV is the volume of the computational cell. Eddies with a size greater than the filter width are resolved, and the eddies smaller than that are filtered out.

2.2.2.2 Filtered Governing Equations

The filtered Navier-Stokes equations for incompressible flows are defined as

$$\frac{\partial \tilde{u}_j}{\partial x_j} = 0 \tag{2.19}$$

$$\frac{\partial \tilde{u}_j}{\partial t} + \frac{\partial \left(\tilde{u}_i \tilde{u}_j\right)}{\partial x_j} = \frac{1}{\rho}\left(\frac{\partial \tilde{\tau}_{ij}}{\partial x_j} - \frac{\partial \tilde{p}}{\partial x_i} - \frac{\partial \tau_{ij}^{sgs}}{\partial x_j}\right) \tag{2.20}$$

where the viscous stress tensor $\tilde{\tau}_{ij}$ and the SGS stress ${\tau_{ij}}^{\text{sgs}}$ are defined as

$$\tilde{\tau}_{ij} \equiv \mu\left(\frac{\partial \tilde{u}_i}{\partial x_j} + \frac{\partial \tilde{u}_j}{\partial x_i}\right) \tag{2.21}$$

$${\tau_{ij}}^{sgs} \equiv \rho\left(\widetilde{u_i \tilde{u}_J} - \tilde{u}_i \tilde{u}_j\right) \tag{2.22}$$

The shear stress due to the eddies that are not resolved is accounted for using SGS models. The SGS stress ${\tau_{ij}}^{\text{sgs}}$, defined using Boussinesq hypothesis is

$${\tau_{ij}}^{sgs} = -2\mu_t \tilde{S}_{ij} \tag{2.23}$$

where, μ_t is the SGS turbulent viscosity, also known as eddy viscosity and $\tilde{S}_{ij}$ is the strain rate tensor for the filtered scales.

The inviscid and viscous fluxes for the three-dimensional unsteady filtered Navier-Stokes equations can be expressed as

$$
\begin{aligned}
\vec{Q} &= (0, \tilde{u}, \tilde{v}, \widetilde{w})^T \\
\vec{E} &= \left(\tilde{u}, \tilde{u}^2 + \tilde{p}/\rho, \tilde{u}\tilde{v}, \tilde{u}\widetilde{w}\right)^T \\
\vec{F} &= \left(\tilde{v}, \tilde{u}\tilde{v}, \tilde{v}^2 + \tilde{p}/\rho, \tilde{v}\widetilde{w}\right)^T \\
\vec{G} &= \left(\widetilde{w}, \tilde{u}\widetilde{w}, \tilde{v}\widetilde{w}, \widetilde{w}^2 + \tilde{p}/\rho\right)^T \\
\vec{E}_v &= (0, \tilde{\tau}_{xx} - {\tau_{xx}}^{sgs}, \tilde{\tau}_{yx} - \tau_{yx}sgs, \tilde{\tau}_{zx} - \tau_{zx}sgs)^T \\
\vec{F}_v &= (0, \tilde{\tau}_{xy} - {\tau_{xy}}^{sgs}, \tilde{\tau}_{yy} - {\tau_{yy}}^{sgs}, \tilde{\tau}_{zy} - {\tau_{zy}}^{sgs})^T \\
\vec{G}_v &= (0, \tilde{\tau}_{xz} - \tau_{xz}sgs, \tilde{\tau}_{yz} - \tau_{yz}sgs, \tilde{\tau}_{zz} - \tau_{zz}sgs)^T
\end{aligned}
\tag{2.24}
$$

2.2.2.3 Subgrid-Scale Models

One of the commonly used SGS models is the static Smagorinsky-Lilly model [95], where the SGS turbulent viscosity is defined as

$$
\mu_t = \rho L_s^2 |\tilde{S}| \tag{2.25}
$$

where $|\tilde{S}| = \sqrt{2\tilde{S}_{ij}\tilde{S}_{ij}}$ and $L_S = \min(kd, C_S\Delta)$ is the mixing length for the unresolved scales. Here, k is the von Karman constant, d is the distance to the closest wall, C_S is the Smagorinsky constant and $\Delta = \sqrt[3]{V}$ is the local grid scale. In the context of homogeneous isotropic turbulence within the inertial sub-range, C_S assumes a constant value. The treatment of C_S as a constant result in suppressing the large-scale turbulent fluctuations near the wall, making this model less suitable for applications near the wall. To overcome this, a modified version known as the dynamic Smagorinsky-Lilly model [96, 97] was used in the present study.

In the dynamic Smagorinsky-Lilly model, the eddies that are resolved using the grid filter (F) are again subdivided into two groups (large resolved eddies and small resolved eddies) using a test filter. The size of the test filter is twice that of the grid

filter. It is assumed that the interaction between the large resolved eddies and the small resolved eddies is similar to the interaction between small resolved eddies and unresolved eddies (see Fig. 2.1). The value of C_s is dynamically computed, leveraging information obtained from the small resolved eddies. This dynamic approach enhances the model's applicability, and it has been successfully utilized by Kaltenbach et al. [87] in simulating the flow through an asymmetric diffuser.

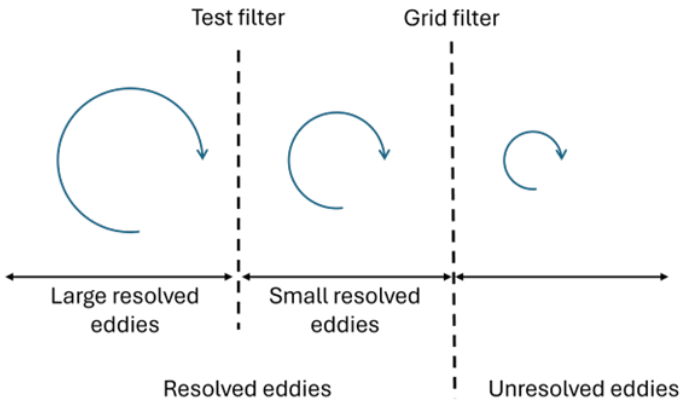

Figure 2.1: Filtering process in dynamic Smagorinsky-Lilly model

CHAPTER 3

NUMERICAL METHOD

3.1 Finite Volume Approach

In the finite volume approach [98], the continuity and momentum equations are integrated over a control volume enclosed by the surfaces of the physical domain. This involves partitioning the computational domain into finite-sized, non-overlapping subdomains or finite volumes using the mesh. The advantage of this approach is the flexibility to discretize complex geometries without any constraints on the shape of the control volume. The three-dimensional unsteady Navier-Stokes equation with no source term is given as:

$$\frac{\partial \vec{Q}}{\partial t} + \frac{\partial \left(\vec{E} - \vec{E}_v\right)}{\partial x} + \frac{\partial \left(\vec{F} - \vec{F}_v\right)}{\partial y} + \frac{\partial \left(\vec{G} - \vec{G}_v\right)}{\partial z} = 0 \tag{3.1}$$

The vectors in Eq (3.1) are described in sections 2.2.1 and 2.2.2 of Chapter 2.

Figure 3.1 shows a schematic of a finite-volume cell in the body-fitted general coordinate system (ξ, η, ψ). By integrating Eq. 3.1 over each finite-volume cell, the modified equation can be expressed as:

$$\iiint_V \left[\frac{\partial \vec{Q}}{\partial t} + \frac{\partial \left(\vec{E} - \vec{E}_v\right)}{\partial x} + \frac{\partial \left(\vec{F} - \vec{F}_v\right)}{\partial y} + \frac{\partial \left(\vec{G} - \vec{G}_v\right)}{\partial z} \right] dV = 0 \tag{3.2}$$

Using the Gauss divergence theorem, the volume integrals of the spatial derivatives in Eq. 3.2 are converted into surface integrals as

$$\iiint_V \frac{\partial \vec{Q}}{\partial t} dV + \int_{A_\xi} \vec{M} \cdot \hat{n}_\xi dA_\xi + \int_{A_\eta} \vec{M} \cdot \hat{n}_\eta dA_\eta + \int_{A_\psi} \vec{M} \cdot \hat{n}_\psi dA_\psi = 0 \tag{3.3}$$

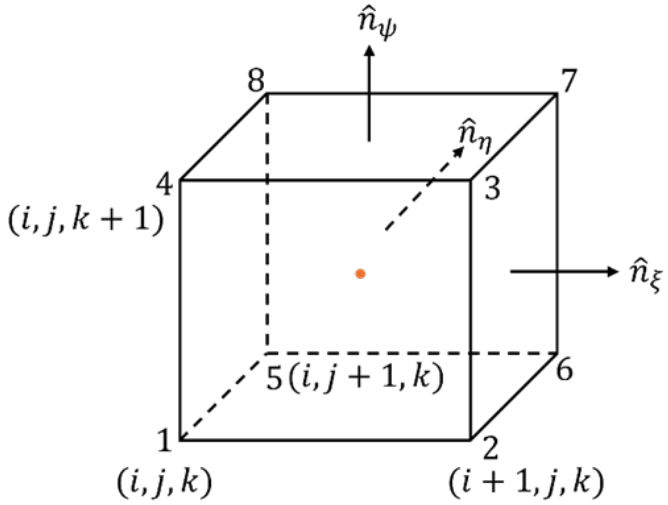

Figure 3.1: Schematic of a finite-volume cell in the general coordinate system (ξ, η, ψ)

where

$$\vec{M} = \left(\vec{E} - \vec{E}_v\right)\hat{\imath} + \left(\vec{F} - \vec{F}_v\right)\hat{\jmath} + \left(\vec{G} - \vec{G}_v\right)\hat{k} \tag{3.4}$$

and $\hat{n}_\xi, \hat{n}_\eta$ and $\hat{n}_\psi$ are the unit normal vectors in the ξ, η, and ψ directions, respectively. The surface area vectors are defined as

$$\begin{aligned} \vec{A}_\xi &= A_{\xi x}\hat{\imath} + A_{\xi y}\hat{\jmath} + A_{\xi z}\hat{k} \\ \vec{A}_\eta &= A_{\eta x}\hat{\imath} + A_{\eta y}\hat{\jmath} + A_{\eta z}\hat{k} \\ \vec{A}_\psi &= A_{\psi x}\hat{\imath} + A_{\psi y}\hat{\jmath} + A_{\psi z}\hat{k} \end{aligned} \tag{3.5}$$

The velocity components in the generalized coordinate direction can be expressed as:

$$\begin{aligned} U &= A_{\xi x}u + A_{\xi y}v + A_{\xi z}w \\ V &= A_{\eta x}u + A_{\eta y}v + A_{\eta z}w \\ W &= A_{\psi x}u + A_{\psi y}v + A_{\psi z}w \end{aligned} \tag{3.6}$$

Using the expression of $\vec{M}$ and the definition of normal vectors, Eq. 3.3 can be written as

$$\frac{\Delta Q}{\Delta t}\Delta V + \left(\vec{E}_\xi - \vec{E}_{\xi v}\right)\Big|_{i-1/2,2,j,k}^{i+1/2,j,k} + \left(\vec{F}_\xi - \vec{F}_{\eta v}\right)\Big|_{i,j-1/2,k}^{i,j+1/2,k} + \left(\vec{G}_\xi - \vec{G}_{\psi v}\right)\Big|_{i,j,k-1/2}^{i,j,k+1/2} = 0 \tag{3.7}$$

where the inviscid fluxes $\left(\vec{E}_\xi, \vec{F}_\xi, \vec{G}_\xi\right)$ and viscous fluxes $\left(\vec{E}_{\xi v}, \vec{F}_{\xi v}, \vec{G}_{\xi v}\right)$ can be expressed as follows

$$\begin{aligned}
\vec{E}_\xi &= A_{\xi x}\vec{E} + A_{\xi y}\vec{F} + A_{\xi z}\vec{G} \\
\vec{F}_\eta &= A_{\eta x}\vec{E} + A_{\eta y}\vec{F} + A_{\eta z}\vec{G} \\
\vec{G}_\psi &= A_{\psi x}\vec{E} + A_{\psi y}\vec{F} + A_{\psi z}\vec{G} \\
\vec{E}_{\xi v} &= A_{\xi x}\vec{E}_v + A_{\xi y}\vec{F}_v + A_{\xi z}\vec{G}_v \\
\vec{F}_{\eta v} &= A_{\eta x}\vec{E}_v + A_{\eta y}\vec{F}_v + A_{\eta z}\vec{G}_v \\
\vec{G}_{\psi v} &= A_{\psi x}\vec{E}_v + A_{\psi y}\vec{F}_v + A_{\psi z}\vec{G}_v
\end{aligned} \tag{3.8}$$

A detailed discussion about the finite volume approach can be found in the work by Zhang [99].

3.2 Gradient Calculation

The gradients of flow variables, such as velocity and pressure, are required to evaluate the fluxes in Eq. 3.7. There are several different methods for calculating these gradients:

- Green-Gauss node-based gradient evaluation
- Green-Gauss cell-based gradient evaluation
- Least Square cell-based gradient evaluation

Among the methods above, the least square cell-based method has been employed in the current work due to its simplicity and computational efficiency. In this

approach, the gradients of flow variables are computed at the cell centroid. Consider the schematic of a quadrilateral cell as shown in Fig. 3.2. The values of any flow variables φ at the target cell and the neighboring cells are denoted as φ_t and φ_i respectively. Since there are four neighboring cells for the target cell, $i = 1, 2, 3$ and 4.

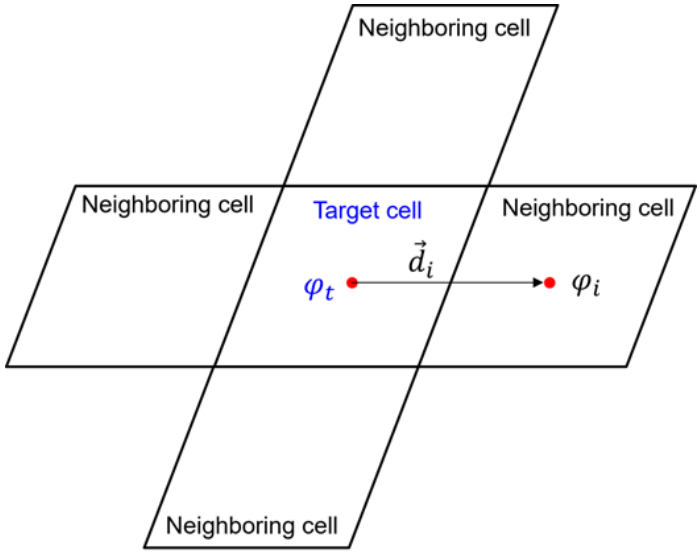

Figure 3.2: Schematic of least square cell-based gradient evaluation

The change in cell-center values of φ can be written as

$$\varphi_i - \varphi_t = \vec{d}_i \cdot (\nabla\varphi)_t \tag{3.9}$$

where $\vec{d}_i$ is the distance between the centroids of neighboring and target cells. The gradient of φ at the target cell centroid is denoted as $(\nabla\varphi)_t$. By taking an initial guess for the value of $(\nabla\varphi)_t$, an approximate solution for the system of equations can be obtained. Since the value of $(\nabla\varphi)_t$ is not correct, there will be an error associated with this, which is given by:

$$e_i = \varphi_i - \left[\varphi_t + \overrightarrow{d_l} \cdot (\nabla\varphi)_t\right] \tag{3.10}$$

The sum of squares of these errors is minimized to obtain the correct gradients at each cell center.

3.3 Evaluation of Inviscid Fluxes

The spatial discretization of the inviscid fluxes is carried out using upwind schemes. In this approach, the face value E_f of the inviscid flux E are obtained from the cell located upstream. The selection of upstream and downstream locations is based on the direction of the normal velocity vector. For a first-order accurate scheme, the face value of any variable E_f is equal to the cell center value of the cell at an upstream location. In a first-order upwind scheme, the cell center value of E is considered as the cell average, which remains constant throughout the cell. Consequently, face values are identical to the cell center values of the upstream cell and can be expressed as:

$$E_{f,i} \approx \begin{cases} E_{i+1} & : m_{f,i} > 0 \text{ (mass flow out)} \\ E_{i-1} & : m_{f,i} < 0 \text{ (mass flow in)} \end{cases} \tag{3.11}$$

where $m_{f,i}$ is the mass flux through the target cell face.

In a second-order upwind scheme, the variation of E_f is determined by

$$E_{f,i} = E_{i-1} + \nabla E_{i-1} \cdot \vec{r}_{i-1} \tag{3.12}$$

where ∇E_{i-1} is the gradient of E at the upstream location and $\vec{r}$ is the displacement vector from the cell centroid of the upstream cell to the face centroid.

3.4 Evaluation of Viscous Fluxes

The central differencing scheme [100], a second-order accurate method, is employed for spatially discretizing viscous flux terms. In this scheme, the face values of any viscous fluxes E_{vf} are determined from the cell center values of adjacent cells sharing the same face f, expressed as

$$E_{vf} = \frac{1}{2}\left(E_{vA} + E_{vB}\right) + \frac{1}{2}\left(\nabla E_{vA} \cdot \vec{r}_A + \nabla E_{vB} \cdot \vec{r}_B\right) \tag{3.13}$$

where E_{vA} and E_{vB} represent the values of E_v at the cell centers of the cells sharing the face f, ∇E_{vA} and ∇E_{vB} are the gradients at cell centers A and B, and $\vec{r}_A$ and $\vec{r}_B$ are vectors directed to the face centroid from the cell centroid.

However, the central differencing scheme may lead to unbounded solutions, introducing stability issues. To address this, a modification is employed by combining the upwind and central differencing schemes as follows:

$$E_{vf} = E_{vf,\,\text{upwind}} + \left(E_{vf,\,\text{central}} - E_{vf,\,\text{upwind}}\right) \tag{3.14}$$

The central differencing scheme, despite its comparatively low numerical dissipation, can result in unwanted oscillations in the solution. In the present work, a combination of three different schemes, 1) pure central differencing, 2) a blended scheme of central differencing and secondorder upwind differencing schemes and 3) a first-order upwind scheme was utilized to overcome this issue. This approach is known as the bounded central differencing method.

3.5 Temporal Integration

Performing a transient simulation requires the discretization of the governing equations both spatially and temporally. Spatial discretization methods are consistent

across both steady and unsteady simulations. Temporal integration of the governing equation involves the integration of all terms in the governing equations at each time instant. Considering the three-dimensional unsteady form of incompressible Navier-Stokes equations with no source term presented in Eq. 3.1, all the terms except the first one are spatial derivatives. Let $F(\chi)$ denote all the temporal discretization terms in Eq. 3.1 such that:

$$\frac{\partial Q}{\partial t} = F(\chi) \tag{3.15}$$

where χ denotes all the spatial derivatives.

The discretized form of the time derivative is given by

$$\frac{Q^{n+1} - Q^n}{\Delta t} = F(\chi) \tag{3.16}$$

where n denotes the current time step and $n+1$ denotes the time step corresponding to $t + \Delta t$. The unknown velocity at a future time step can be represented as

$$Q^{n+1} = Q^n + \Delta t F(\chi) \tag{3.17}$$

By knowing the values of $\Delta t, Q^n$ and $F(\chi)$, the value of Q^{n+1} can be determined. Based on the way the value of $F(\chi)$ is obtained, time integration methods can be classified as explicit and implicit approaches. The present study utilized the implicit approach.

In the implicit approach, $F(\chi)$ is determined from the current time step as

$$Q^{n+1} = Q^n + \Delta t F\left(\chi^{n+1}\right) \tag{3.18}$$

As $F\left(\chi^{n+1}\right)$ is unknown at the current time step, an iterative approach is employed to determine $F\left(\chi^{n+1}\right)$. In the iterative time advancement scheme, all governing equa-

tions are solved iteratively for each time step until convergence criteria are satisfied. While this approach can be computationally intensive due to the need for multiple iterations, it offers increased accuracy compared to non-iterative time advancement schemes. The present study uses a second-order discretization method for the transient derivative, which can be expressed as:

$$\frac{3Q^{n+1} - 4Q^n + Q^{n-1}}{2\Delta t} = F(\chi) \tag{3.19}$$

3.6 Boundary Conditions

Velocity inlet: Used to define the fluid properties at the inlet of the computational domain. The pressure corresponding to the specified inlet velocity is calculated by the solver and assigned to the inlet plane. This boundary condition is applicable only in incompressible flows.

Outflow: Models the flow exits by extrapolating the information from inside the computational domain to the exit plane. Here, the diffusion fluxes corresponding to all the flow variables in the direction normal to the exit plane are set to zero, and an overall mass balance correction is made.

Periodic: Used when the geometry and flow pattern exhibit a periodic nature. Note that it can be used only between a pair of boundaries. In the present study, a translationally periodic boundary condition is used on the sides of the computational domain.

No-slip wall: Used at the interface between fluid and solid regions. This boundary condition can either be used as a stationary or moving wall, depending on the physical nature of the problem. In a stationary wall, the fluid velocity is zero at the

wall, whereas in a moving wall scenario, the fluid velocity at the wall should be equal to the velocity of the wall.

3.7 Parallel Computing

The present work utilized Cadence Pointwise to generate the mesh and ANSYS Fluent to conduct all the simulations. A Corsair MZ32-AR0-00 workstation equipped with a sixteen-core AMD EPYC 7F52 processor and 64 GB RAM was used to perform all the simulations.

CHAPTER 4

PERFORMANCE EVALUATION OF AN ASYMMETRIC DIFFUSER USING RANS

4.1 Case Description

Among the vast literature on flow through asymmetric diffusers, the experimental work by Buice et al. [86] and the LES study by Kaltenbach et al. [87] are particularly notable due to their comprehensive nature. Thus, these works were chosen as the baseline in the present study. Figure 4.1 is a schematic of the diffuser section used in the present study. The diffuser is similar to the geometry of Buice et al. and Kaltenbach et al., except for the rounded corners. The half-height of the inlet channel H(7.5 mm) was used as the reference length scale per Kaltenbach et al. The computational domain consisted of a straight inlet channel of length $220H$ (1650 mm), height $2H$(15 mm), and width $8H$(60 mm) followed by a diffuser with a divergence of ten degrees and an exit duct. The total streamwise extent of the domain was $300H$(2250 mm). The inlet channel length was chosen so that a fully developed turbulent flow enters the diffuser. To reduce losses due to the presence of sharp turns, the upstream and downstream corners were rounded with a radius of $8.6H$. As shown in Fig. 4.1, the (x, y, z) coordinate system is located at the plane of symmetry and at the intersection of the tangents of the incoming and diverging surface where x points in the incoming streamwise direction.

The present work studied both ramp- and vane-type VGs to understand how they affect the performance of a diffuser with a large separated flow. Figure 4.2shows the schematics of the three types of VGs studied. "R" indicates ramp-type VGs,

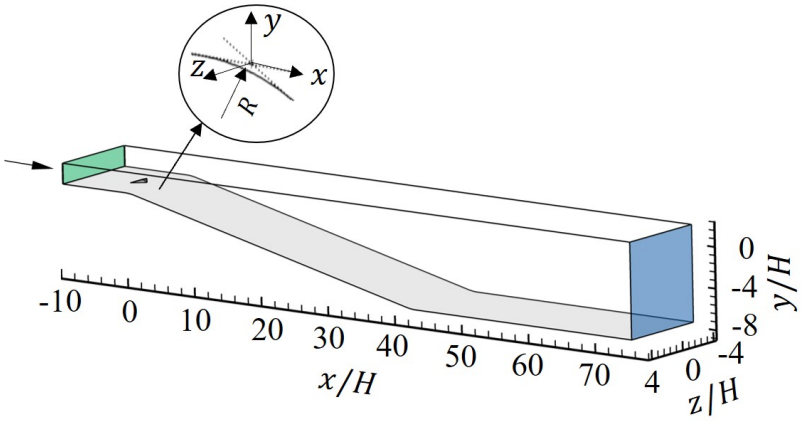

Figure 4.1: Schematic of the diffuser geometry.

"Vu" and "Vd" indicate vane-type VGs that develop an upwash or a downwash, respectively in the channel between them. Their geometric specifications are listed in Table 4.1. Table 4.1 shows four of each configurations for a total of twelve cases. The distance $s/H = 3.6$ separates the widest points of the vanes. The length and width of the VGs were changed in proportion to the height. For ramp-type VGs, the length and width were selected as four times their height. For the vane type, the length was kept four times the height and the leading edge of the vanes was at an angle of attack of 22 degrees with the incoming flow. The thickness of each vane was 0.3 mm [101]. The vanes were arranged in a tapered fashion such that a pair of counter-rotating vortices emanated from the vane with a downwash near the center plane and an upwash near the side walls for the "Vd" type and the opposite for the "Vu" type. The VGs were placed in the inlet channel such that its trailing edge was located at $x = -2H$.

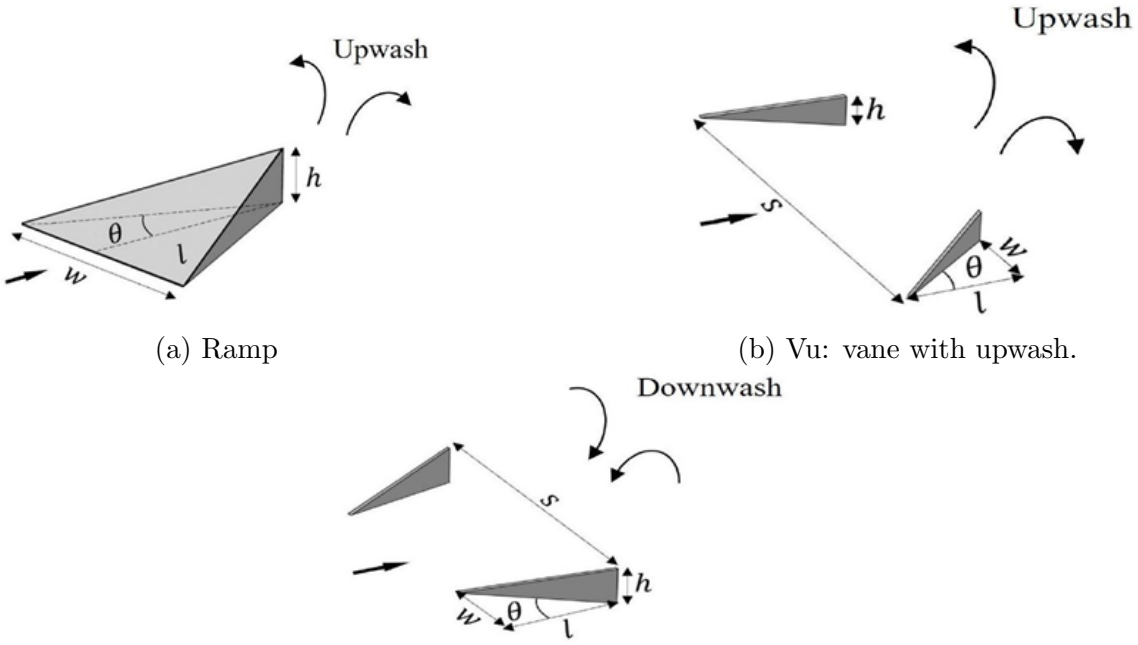

(a) Ramp

(b) Vu: vane with upwash.

(c) Vd: vane with downwash.

Figure 4.2: Vortex generator schematics.

Table 4.1: VG specifications.

VG	h/H	l/H	w/H			
R1, Vu1, Vd1	0.05	0.2	R1	0.2	Vu1, Vd1	0.08
R2, Vu2, Vd2	0.1	0.4	R2	0.4	Vu2, Vd2	0.16
R3, Vu3, Vd3	0.2	0.8	R3	0.8	Vu3, Vd3	0.32
R4, Vu4, Vd5	0.4	1.6	R4	1.2	Vu4, Vd4	0.64

4.2 Model Validation and Verification

4.2.1 Grid Generation and Grid Independence Study

Using Cadence Pointwise, the three-dimensional computational domain was treated with a hybrid mesh: unstructured grid in the vicinity of VGs to avoid the highly skewed cells at the sharp corners and structured grid in all other regions. For the structured mesh, the spanwise grids were distributed with equal spacing. A high grid density near the wall resolved the steep velocity gradients. The smallest grid

spacing for all the cases was fixed at 0.1 mm , corresponding to $y^+ = 3$, which is within the viscous sublayer. A monotonic rational quadratic spline (MRQS) grid distribution was implemented to attain a monotonic and smooth transition between the high- and low-grid density regions [102].

A grid independence study (GIS) was conducted to ascertain a grid distribution that provided acceptable accuracy while maintaining computational efficiency. The asymmetric diffuser without the presence of any VGs was chosen for this purpose. Coarse, medium, and fine grids were generated with the cell counts shown in Table 4.2. Starting from the coarse grid, a grid refinement ratio of 1.5 was applied in each coordinate direction to generate finer grids successively. Table 4.2 displays average grid spacing for the entire domain and shows dense clustering where the VGs would eventually be located, as well as the average spacing in the divergent section.

Table 4.2: Grid information. All dimensions in mm.

Grid	No. of cells $\{N_x, N_y, N_z\}$	Av. grid spacing, entire domain	Av. grid spacing, VG location	Av. grid spacing, divergent section
Coarse	$\{460, 30, 20\}$	$4.89 \times 0.50 \times 1.50$	$1.22 \times 0.50 \times 3.00$	$2.05 \times 1.42 \times 3.00$
Medium	$\{678, 46, 30\}$	$3.31 \times 0.32 \times 1.00$	$0.83 \times 0.32 \times 2.00$	$1.36 \times 0.92 \times 2.00$
Fine	$\{1008, 70, 46\}$	$2.23 \times 0.21 \times 0.65$	$0.57 \times 0.21 \times 1.30$	$0.90 \times 0.61 \times 1.30$

A commonly used measure to quantify grid convergence is the grid convergence index (GCI) defined by [103]

$$GCI_{i,i+1} \equiv \frac{F_S \left|\varepsilon_{i,i+1}\right|}{r^{\Pi} - 1} \tag{4.1}$$

where F_S is the factor of safety with a recommended value of 1.25 for comparing two or more grids. The relative error in the measurement of any quantity f between two grids is given by

$$\varepsilon_{i,i+1} = \frac{|f_i - f_{i+1}|}{f_i} \tag{4.2}$$

Grid $i+1$ is finer than grid i. The parameter Π is the order of convergence that will be elaborated later. The quantity f in the present study is the normalized location of flow reattachment, that is, the streamwise location at which the value of wall shear stress in the x-direction $\tau_{w_x} = 0$. The values of f_1, f_2, and f_3 were $61.59, 59.70$, and 58.63 , respectively. The relative error values corresponding to these f values were $\varepsilon_{1,2} = 0.031$ and $\varepsilon_{2,3} = 0.018$.

The order of convergence is defined as

$$\Pi \triangleq \frac{\ln\left[\left(f_1 - f_2\right) / \left(f_2 - f_3\right)\right]}{\ln r} \tag{4.3}$$

where r is the grid refinement ratio. The value of Π was found to be 1.41 , which is less than the theoretical value of 2 due to the specific boundary conditions and numerical methods used in different simulations. The present values of $GCI_{1,2} = 0.050$ and $GCI_{2,3} = 0.029$. Grid independence was achieved when

$$\frac{GCI_{1,2}}{r^{\Pi} GCI_{2,3}} \approx 1 \tag{4.4}$$

The present values satisfied the relationship of Eq. 4.4 with a value of 0.973.

The medium grid was considered acceptable for performing further studies. For illustration, the grid distribution for the medium grid on the symmetry plane is shown in Fig. 4.3a. The grid distribution close to the vane- and ramp-type VGs are also shown in Fig. 4.3b and 4.3c.

The velocity profiles at different streamwise locations, along with the streamwise distribution of the pressure coefficient c_p

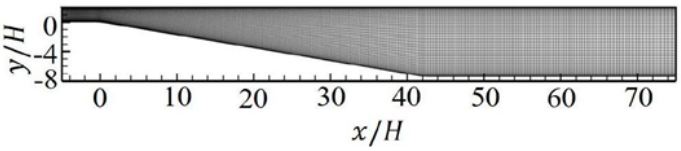

(a) Grid distribution for the baseline diffuser.

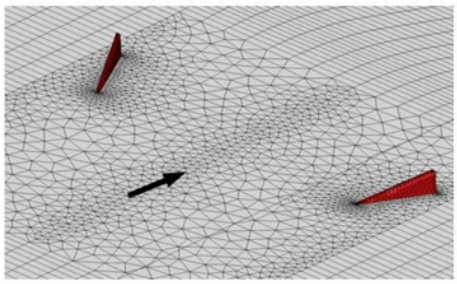

(b) Surface grid distribution near "Vd" type VGs.

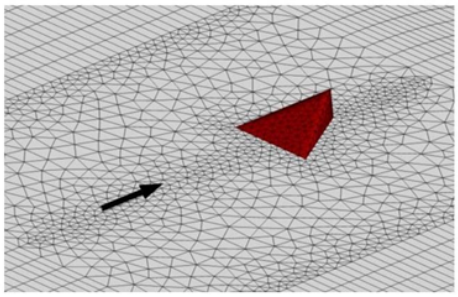

(c) Surface grid distribution near "R" type VG.

Figure 4.3: Grids used in the numerical simulations.

$$c_p = \frac{p - p_{ref}}{\frac{1}{2}\rho U^2} \tag{4.5}$$

where the ref is $x = -3.4H$[1], and the axial skin friction distribution on the deflected wall

$$c_{f_x} = \frac{\tau_{w_x}}{\frac{1}{2}\rho U^2} \tag{4.6}$$

were used to examine grid convergence. The data were generated with an incoming uniform velocity of 20 m/s and a two percent freestream turbulence intensity. Figure 4.4 compares the normalized velocity profiles with the results of [86, 87]. The ordinate of all the velocity profile plots was kept the same as that of the height of the exit duct at $9.4H$. Inspection of the data before the diffuser entrance at -4.02 H showed good agreement in the coarse through fine meshes with the data from [86, 87]. In the diffuser section, the medium and fine grids showed agreement between themselves and with their experimental and LES counterparts.

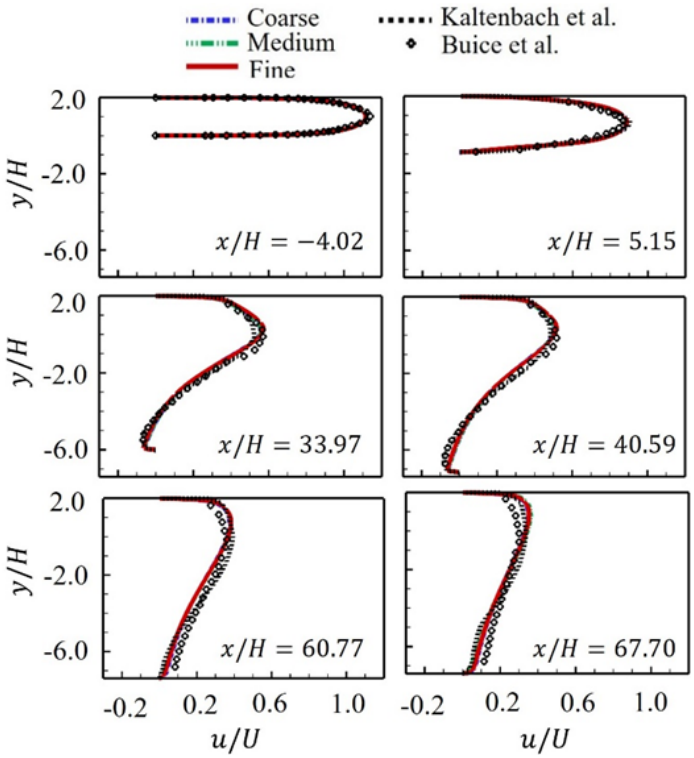

Figure 4.4: Comparison of normalized velocity profiles at different streamwise locations; data taken at the plane of symmetry

The c_p distribution obtained for medium and fine grids showed agreement among themselves and with the LES and the experimental results. However, the skin friction data showed that the present study over predicted the separation size regardless of the grid. Based on the current study, the separation location was at $x = 4H$, which was upstream of the experimental and LES results of $x = 12H$ and $12.1H$, respectively. Nonetheless, despite this discrepancy in the separation location with those of previous investigators, it was deemed that the present simulations were acceptable for studying the effect of VGs on the diffuser flow.

The streamline pattern of the baseline diffuser revealing the separated flow is shown in Fig. 4.6. The separation and reattachment points are indicated by (S) and (R), respectively. The isoline if $u = 0$ is shown in white. Figures 4.5 and 4.6 indicate

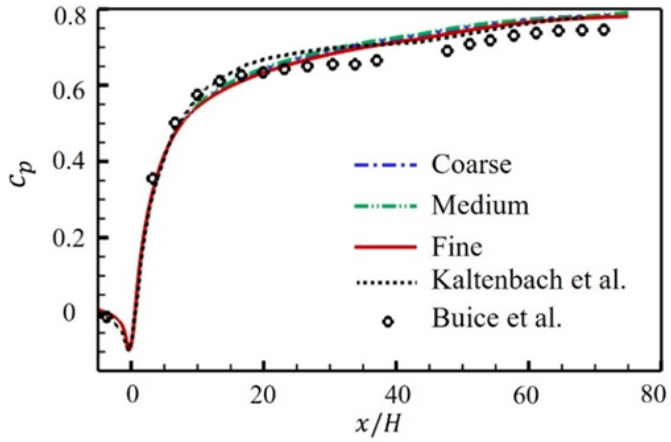

(a) Pressure coefficient.

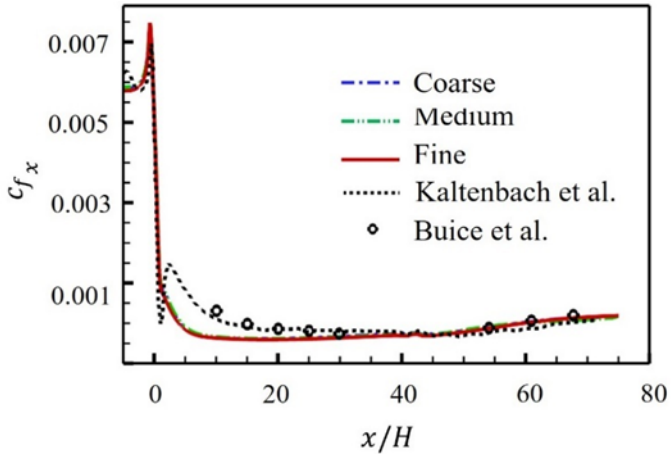

(b) Skin friction coefficient.

Figure 4.5: Distribution of c_p and c_{f_x} in the streamwise direction of the bare diffuser; data taken at the plane of symmetry.

that the geometry yields an incipient stall condition based on Kline's classification of symmetric, two-dimensional, plane-walled diffusers [104].

The steady, incompressible Reynolds-averaged continuity and momentum equations with no body forces were solved numerically using the ANSYS Fluent commercial solver. The SST (shear-stress transport) $k-\omega$ turbulence model [94] was used due to its ability to capture the separation and attachment locations with reasonable accuracy. The SIMPLE (semi-implicit method for pressure-linked equations)

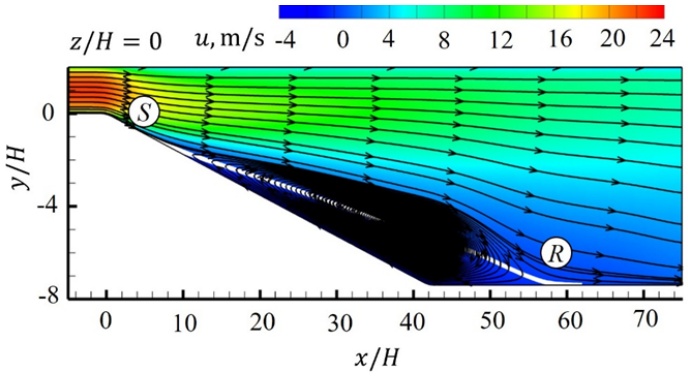

Figure 4.6: Streamlines of the baseline diffuser. Note the stretched ordinate.

pressure-velocity coupling algorithm was used to calculate the pressure field. A first-order upwind scheme was used to spatially discretize the turbulent kinetic energy k and the specific dissipation rate ω, while a second-order upwind scheme was used for pressure and momentum. Pertinent properties of air at 1 atm and 288K are a density of 1.225kg/m^3, a dynamic viscosity of 1.789×10^{-5} Pa $\cdot$ s, a specific heat at constant pressure of 1006.4 J/(kg$\cdot$K) and a thermal conductivity of 0.0242 W/(m$\cdot$K). Further details regarding the turbulence model are mentioned in Chapter 2

In practice, an array of VGs are deployed on the geometry to control flow separation. In this numerical study, however, a single VG configuration was used in each simulation with a periodic boundary condition implemented on the side walls to understand the effect on the flow. A no-slip boundary condition was specified on the VGs as well as on the top (flat wall) and bottom (deflected wall) boundaries, whereas an outflow boundary condition was given at the outlet of the computational domain.

4.2.2 Model Validation

A uniform velocity of 20 m/s and a freestream turbulence intensity of two percent were specified at the inlet of the computational domain located at $x = -200H$. The length of the inlet channel was chosen such that the flow became fully devel-

oped before reaching the diffuser inlet [86]. Figure 4.7 shows the normalized velocity profiles at different streamwise locations in the inlet channel. The velocity profiles collapsed into a single profile at streamwise locations near the diffuser entrance, which meant that the flow was fully developed. Also, note that a fully-developed turbulent flow entered the diffuser. Figure 4.8 shows the incoming profiles in wall coordinates where $y^+ = yu_\tau/v_w, u^+ = u/u_\tau$ and $u_\tau = \sqrt{\tau_w/\rho}$ is the friction velocity, plotted from the wall to the diffuser centerline. The figure also plots the equations for the sublayer and the law-of-the-wall:

$$u^+ = y^+ \tag{4.7}$$

$$u^+ = \frac{1}{K}\log y^+ + C \tag{4.8}$$

where $K = 0.4$ and $C = 5.1$. Figure 4.7 shows that the entrant flow at $x/H = -200$ possessed a uniform core and thus appeared to take on a boundary layer type of profile. This is seen in the distinct "wake" profile in Fig. 4.8. Further downstream, from $x/H = -100$ to the end of the uniform channel, the normalized velocity profiles shown in Fig. 4.7 were self-similar, indicating that it was fully-developed. Moreover, Fig. 4.8 shows that these fully-developed channel profiles collapsed with a small departure from the law of the wall near the middle of the channel, as observed by Wei and Willmarth [105].

4.3 Asymmetric Diffuser

4.3.1 Flow Characteristics

The fully-developed turbulent flow from the inlet channel enters the expansion region and separates at $x/H = 4$. Figure. 4.9 shows the limiting streamline distribu-

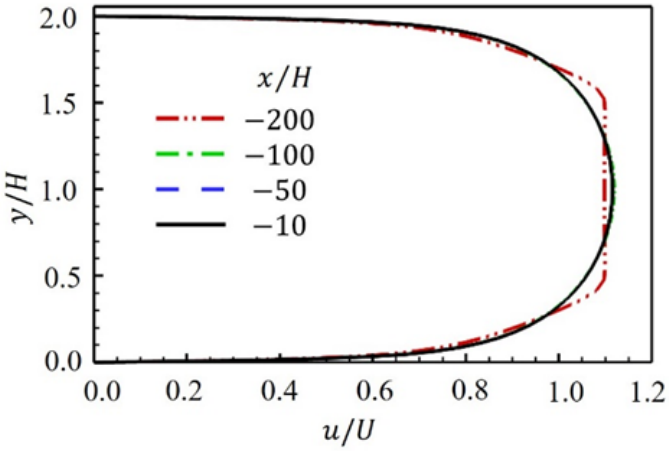

Figure 4.7: Velocity profiles in the inlet channel.

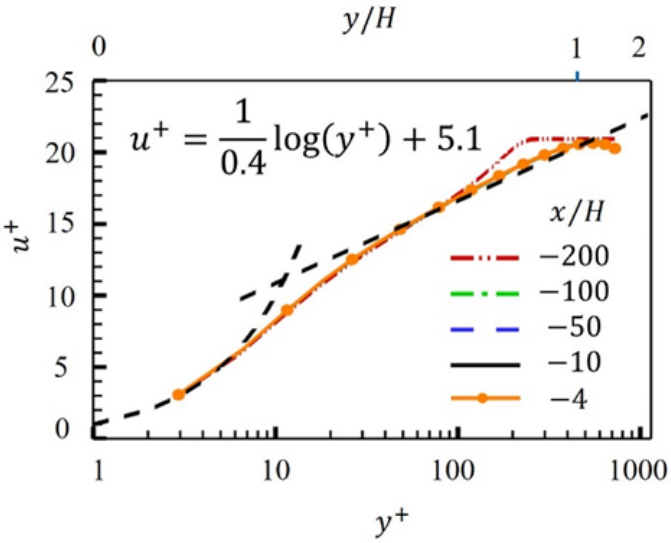

Figure 4.8: Velocity profiles in the inlet channel in wall coordinates.

tion on the deflected wall of the diffuser. Due to the two-dimensional nature of the flow through this diffuser, the separation line appears as a straight line at $x/H = 4$. If the flowfield was not two-dimensional, the separation location at each spanwise location would have been different. It can also be noted that the flow reattaches at $x/H = 60$. The region between the separation and attachment lines has a light blue contour, which indicates the negative values of the skin friction coefficient. The

discussion regarding pressure and skin friction distribution on the deflected wall at symmetry location are shown in Figs. 4.5a and 4.5b, respectively.

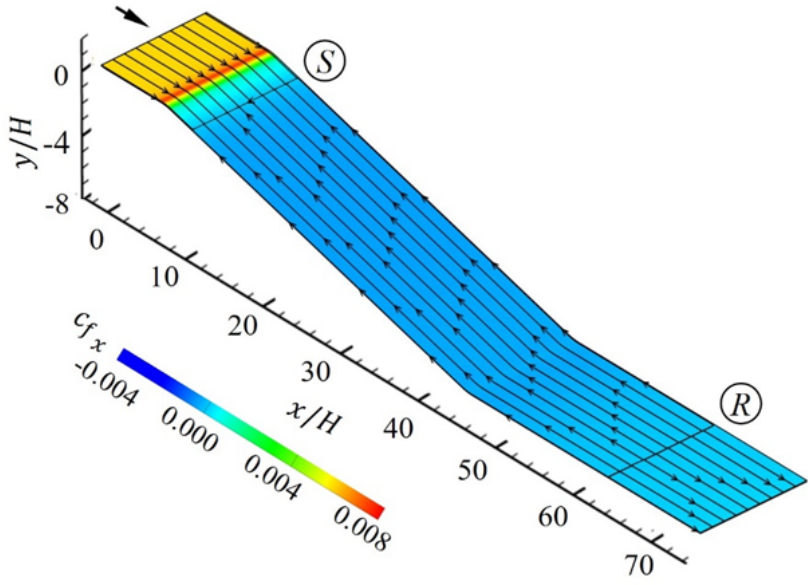

Figure 4.9: Limiting streamlines for the baseline case.

4.3.2 Performance Matrix

Based on the Society of Automotive Engineers (SAE) Aerospace Recommended Practice for a circular engine face, a measure of diffuser performance is the distortion index [106, 107]. It is defined here as

$$DI \triangleq \frac{p_{t,\,\max} - p_{t,\,\min}}{p_{t,av}} \tag{4.9}$$

where P_t is the total pressure. The subscripts max, min, and av refer to the maximum, minimum, and average values, respectively. The distortion index indicates the uniformity of the total pressure distribution across a cross-section. One of the applications of DI is in the flow through compressors. A flow with a high DI leads to

nonuniform loading in the compressor, resulting in poor compression and increased vibration. The DI values are calculated at $x/H = 70$, the last station considered in the control volume analysis.

Another performance measure is the diffuser efficiency, η_D [56]

$$\eta_D \triangleq \frac{p_{2,av} - p_{1,av}}{\frac{1}{2}\rho\left(u_{1,av}^2 - u_{2,av}^2\right)} \tag{4.10}$$

where the subscripts 1 and 2 refer to the inlet and exit planes at $x/H = -10$ and 70, respectively. The diffuser efficiency depends strongly on the divergence angle of the diffuser and the incoming turbulent boundary layer thickness. For the baseline case, the DI and η_D were determined to be 0.151 and 0.785, respectively. These values serve as a baseline to evaluate the performance of different VG configurations.

4.4 Asymmetric Diffuser with Vortex Generators

4.4.1 Flow Characteristics

A VG produces a streamwise CVP and localized separation zones in the diffuser, creating a topologically complex flow [108], as evidenced in Figs. 4.10 through 4.12. The surface topology reveals the presence of saddle points along the separation and (re)attachment lines and foci on either side of the channel. Off the surface, the strong CVP shed by the VGs is evident, as well as other singularities. An analysis of the topological features is beyond the scope of this paper.

A qualitative understanding of the flow features can help establish how the VG and the associated CVP function to control flow separation. To start, consider the surface topology. For computational studies, "limiting streamlines" are used to visualize the surface footprint, which is analogous to experimental skin friction lines [109]. These are projections of the streamlines at the first cell height onto the

wall. The accuracy of the limiting streamline concept diminishes near separation and (re)attachment lines but does not impact the qualitative interpretation of the results.

The limiting streamlines of the flow past a ramp will be described first, followed by brief descriptions of the same for a vane pair producing upwash and downwash, respectively, in the channel between them. This sequence generally follows the expected disruption of the bare diffuser flow, from minor to major, with an increase in the VG dimensions. Recall from Table 4.1 that the VG height increases from $0.05 - 0.4$ of the half height of the incoming channel.

Figure 4.10 shows the limiting streamline pattern for the no-ramp and the four ramp VGs cases labeled R1 through R4. The no-VG case presents a simple, two-dimensional pattern. The degenerate flow pattern yields a singular separation point S that is representative of the separation line perpendicular to the incoming flow; see also Fig. 4.6. At S, the skin friction vanishes, and the limiting streamlines lift off the surface to form the separation streamline. For this no-VG case, the separation is closed, and the separation streamline reattaches at the reattachment point R, which is also a singularity with vanishing skin friction. The alternate situation when the separation streamlines do not reattach to result in an open separation pattern [108] does not occur in the present results.

The ramp generates a CVP that causes a downwash at spanwise locations away from the mid plane, as shown in Fig. 4.10. As a result, the separation region size is reduced only at these locations. Also, the upwash created near the midplane results in an upstream shift of the separation line from $x/H \approx 4$ to ≈ 2. This observation can be substantiated by the dark blue shade shown by the c_{f_x} contour at the midplane, which means that its value is reduced due to the upwash.

More flow features are seen with the larger ramps. These larger ramps are chosen to provide a strong CVP but at the same time not to induce excessive drag.

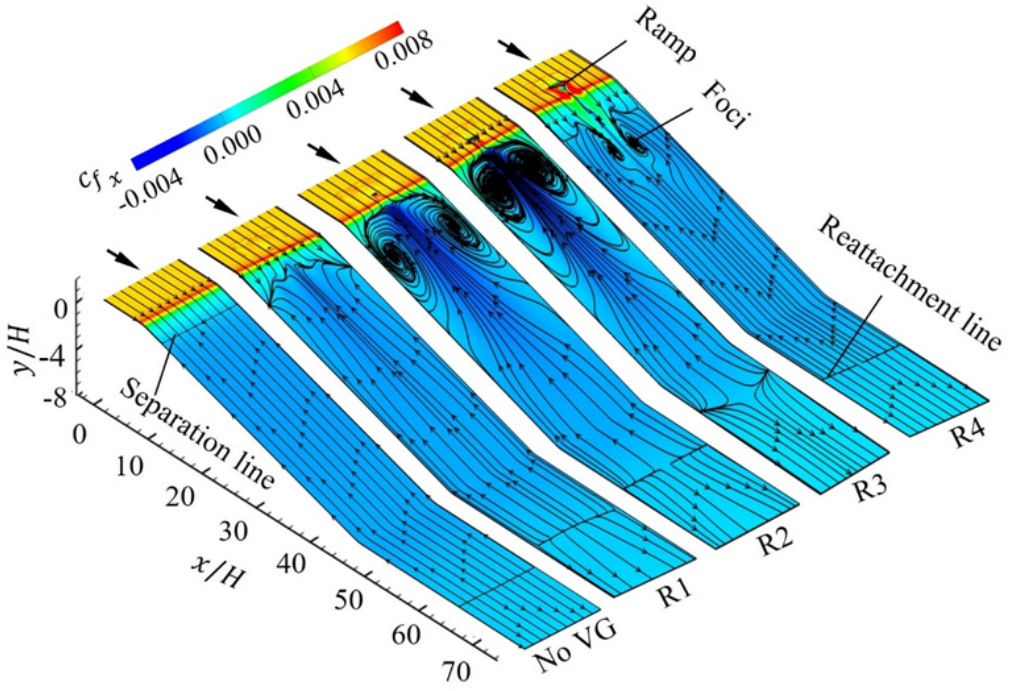

Figure 4.10: Limiting streamlines for ramp-type VG.

A pair of foci appears near the side boundaries for R2 and R3. This feature was experimentally observed [84]. When the size of the VG increases to $0.4H$, the two foci move close to the midplane and become vastly decreased. Another pair of foci appear immediately downstream of R4 near the midplane. It can be noted that R3 results in an early reattachment of the separated flow. Based on observations of the limiting streamlines, R3 appears to be the most promising in reducing the average separation zone with the possibility of improving the performance of the diffuser.

The limiting streamline patterns for vane-type VGs are shown in Figs. 4.11 and 4.12. The small Vu1 and Vd1 produce small changes to the limiting streamline pattern, similar to R1. However, the limiting streamline patterns for Vu2 and Vd2 show distortions that include two upstream protrusions that can be regarded as foci

of opposite signs as for R2. The upstream protrusions indicate that the CVP in these cases produces a stronger effect than R2.

The limiting streamline pattern for the large upwash vane Vu3 showed a strengthening of the weak foci observed in Vu2 while the pattern in Vu4 showed that the foci almost merged. The large downwash vanes, Vd3 and Vd4 , produced a distinctly different limiting streamline pattern. It appears that the increasing downwash separated the foci further. For Vd4, there appeared to be severe disruption of the separation bubble. Unlike the smaller Vd vanes, the limiting streamlines in Vd4 appeared to be primarily moving downstream. The reattachment line appeared to be eliminated.

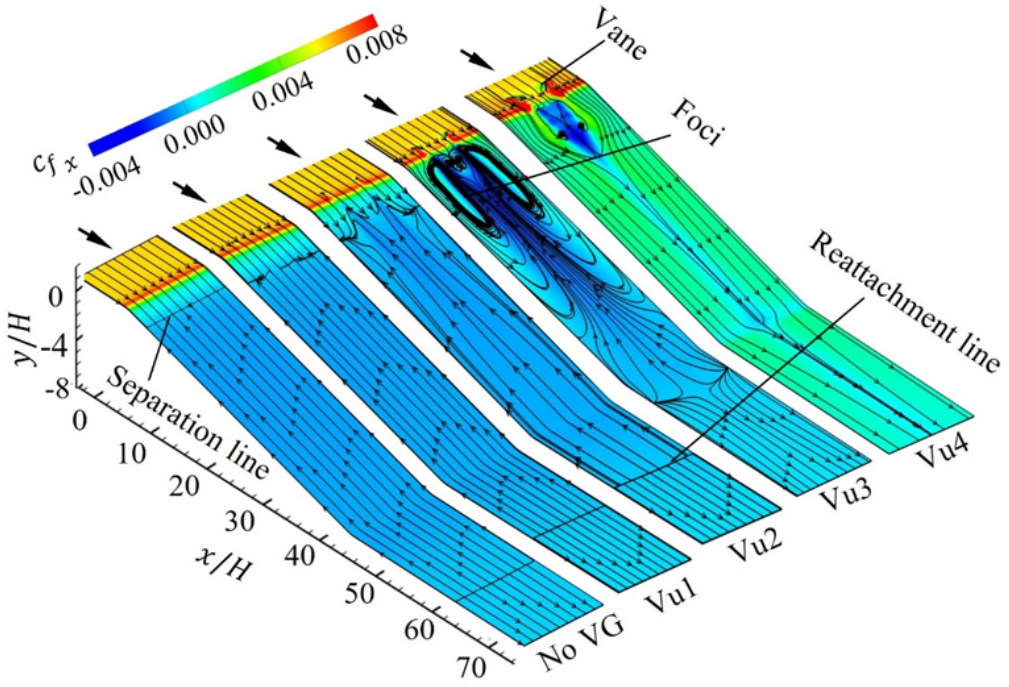

Figure 4.11: Limiting streamlines for Vu.

The strong downwash due to Vd3 and Vd4 merits further examination. Figure 4.13 shows the streamline patterns in the crosswise plane with contours of the normalized streamwise vorticity.

$$\Omega_x = \frac{\omega_x H}{U} \tag{4.11}$$

The normalized streamwise vorticity is useful for tracking the CVP. For both of these vanes, the wake shows the growth of the CVP, with Vd4 being stronger based on Ω_x. The vortex cores for both vanes appear to be weak at $x/H = 20$ and entirely vanish at $x/H = 50$. This can be expressed as $x/h = 200$, which is consistent with the results of others [34]. However, the crosswise streamlines still show a downwash pattern. This downwash is thought to energize the flow nearest the wall, thereby reducing the separation zone. Flow separation in the vicinity of the midplane appears to be partially and completely eliminated in Vd3 and Vd4, respectively.

4.4.2 Performance Matrix

4.4.2.1 Flow Separation Control

The limiting streamline patterns shown in Figs. 4.10 through 4.12 give a qualitative understanding of the separation and attachment location. Since one of the purposes of installing VGs is to reduce or eliminate the separation bubble, it appears that they are able to accomplish this purpose, particularly with the larger vanes Vu4, Vd3 and Vd4. Further evidence of separation bubble reduction is provided by the pressure recovery as characterized by the surface pressure coefficient c_p and the streamwise skin friction distribution c_{f_x}. For this discussion, the streamwise distributions of these parameters are shown for $z/H = 0, 1, 2, 3$ in Figs. 4.14 through 4.16. The baseline, no-VG case is included for comparison. The surface pressure distribu-

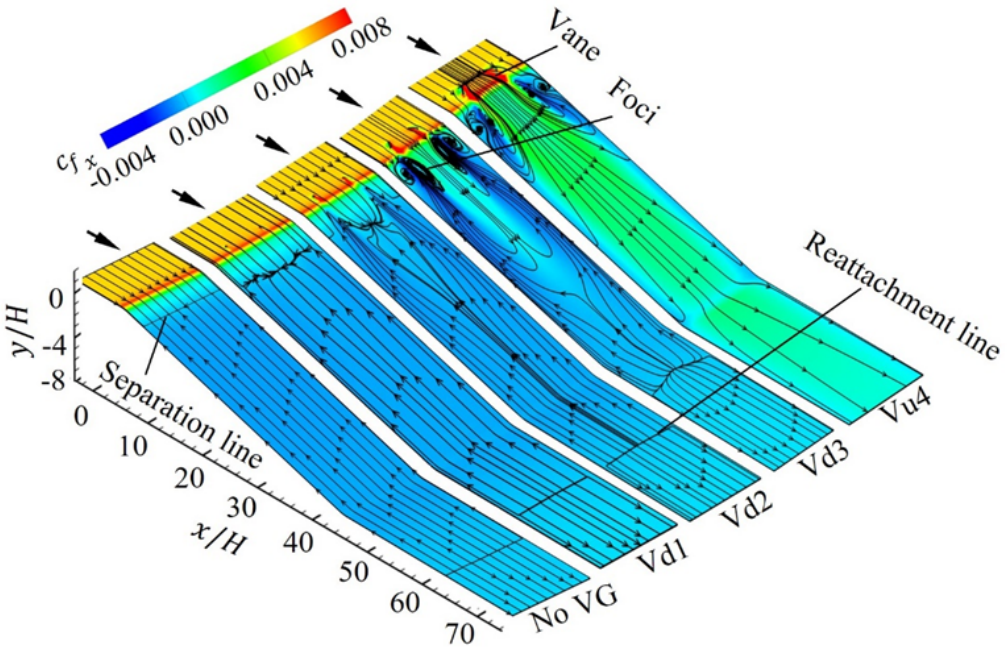

Figure 4.12: Limiting streamlines for Vd.

tion is shown in the left panel of Fig. 4.14. Despite the distortions in the limiting streamline patterns, the pressure distribution appears to be two-dimensional for all the ramps. There does not appear to be significant pressure recovery for R1 or R4 .

The c_{f_x} distribution is shown in the right panel of Fig. 4.14. The three-dimensionality is particularly noticeable for R2 and R3. Interestingly, the distortion is reduced for R4, which is consistent with the observations of the limiting streamlines. Beyond $x/H \approx 30$, the three-dimensionality appears to be insignificant. Moreover, even though Fig. 4.10 shows that the reattachment line is further downstream, the longitudinal skin friction distribution shows that $c_{f_x} \approx 0$ closer to the corner, thereby effectively rendering a smaller separation bubble. This occurs at $x/H \approx 10$ for R 4 .

The CVP from the ramp induces an upwash near the midplane and a downwash further outboard. The flow topology indicates that the outboard downwash forces

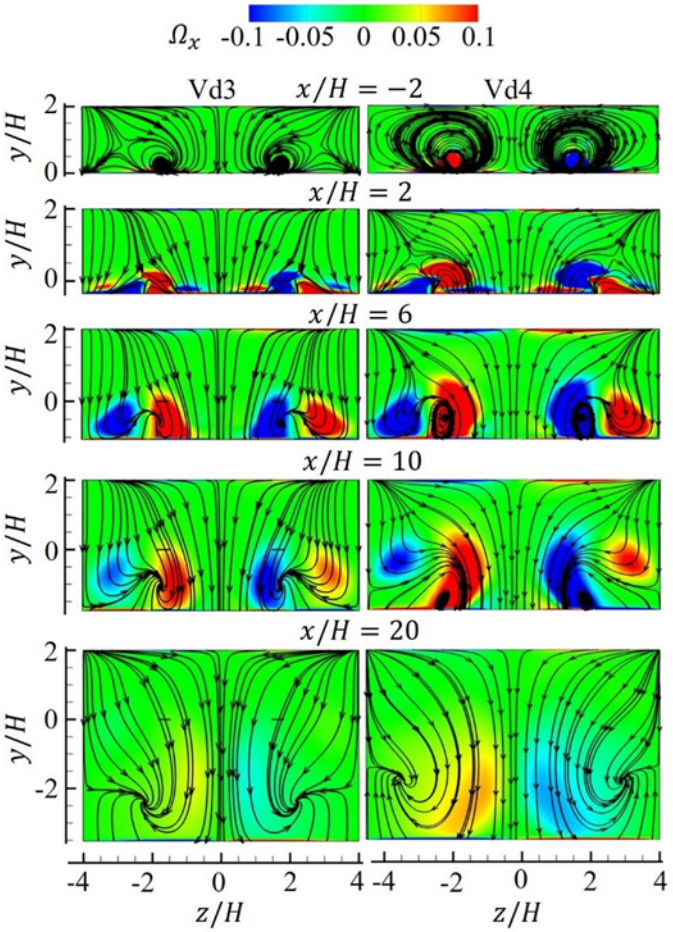

Figure 4.13: Crosswise streamlines and vorticity contours for Vd3 and Vd4.

the foci toward the middle. It appears that this flow pattern increases the surface shear upstream that is reflected by increased flow distortion, as is also displayed in the limiting streamline patterns in R2 and R3 , see Fig. 4.10.

The surface pressure coefficient presented in the left panel of Fig. 4.15 shows that Vu1 and Vu2 yield similar results as that of the ramps with only a very slight improvement in pressure recovery. The skin friction in the axial direction, presented in the right panel, also shows very small improvements. However, the larger Vu3 and Vu4 vanes show an initial improvement in the surface pressure distribution as early as $x/H \approx 2$. In particular, the Vu4 distribution way surpasses the baseline

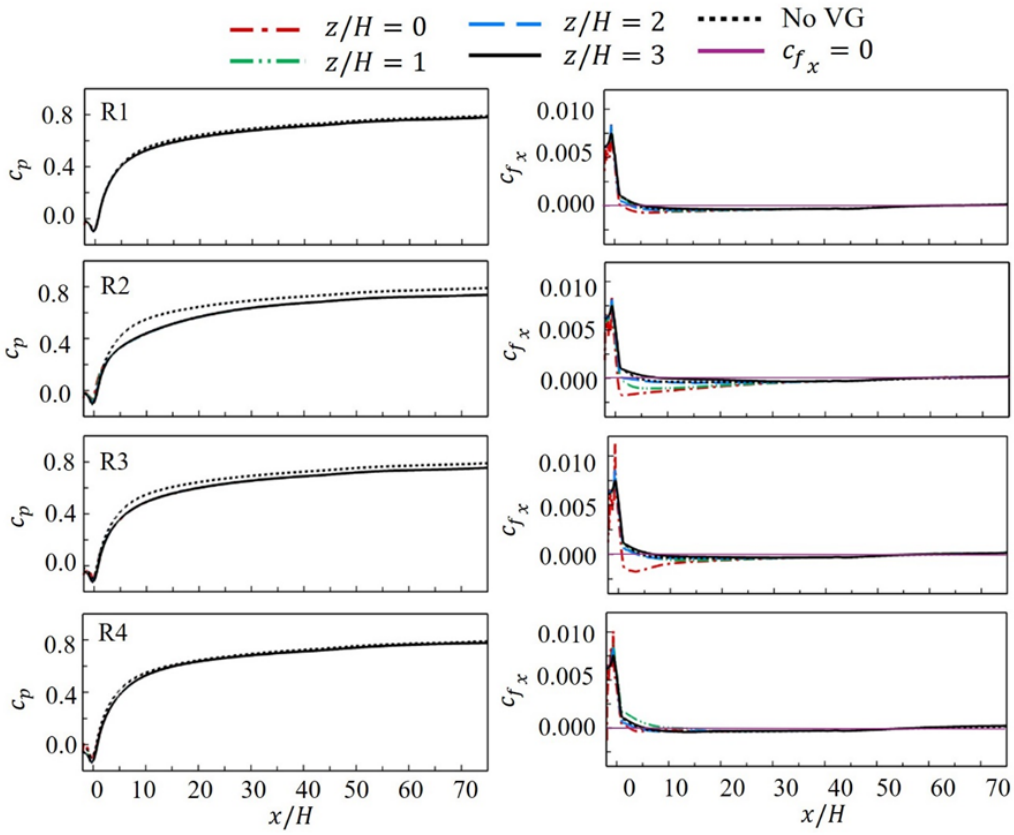

Figure 4.14: Streamwise distributions of c_p and c_{f_x} for the ramp cases.

distribution in this early stage. However, the performance gains became negligible when $x/H \gtrsim 35$.

The c_{f_x} distribution for the smaller vanes Vu1 and Vu2 indicates they have a weak effect on the separation region, see also Fig. 4.11. However, large negative values are seen for Vu3. This provides further evidence of strong upstream flow near the middle of the channel, which is counteracted by strong downstream flow at the sides, as also evidenced in Fig. 4.11. These topological features are found in the presence of strong crossflows. For the strongest Vu4 case, the two foci seen in Fig. 4.11 draw close to each other, causing the outboard limiting streamlines to flow downstream, leading to large positive values of c_{f_x}. Positive skin friction values occur in all the

z/H locations examined for $x/H \gtrsim 15$. This implies an increase in frictional drag and has implications in the use of such vanes for improving the performance of short diffusers.

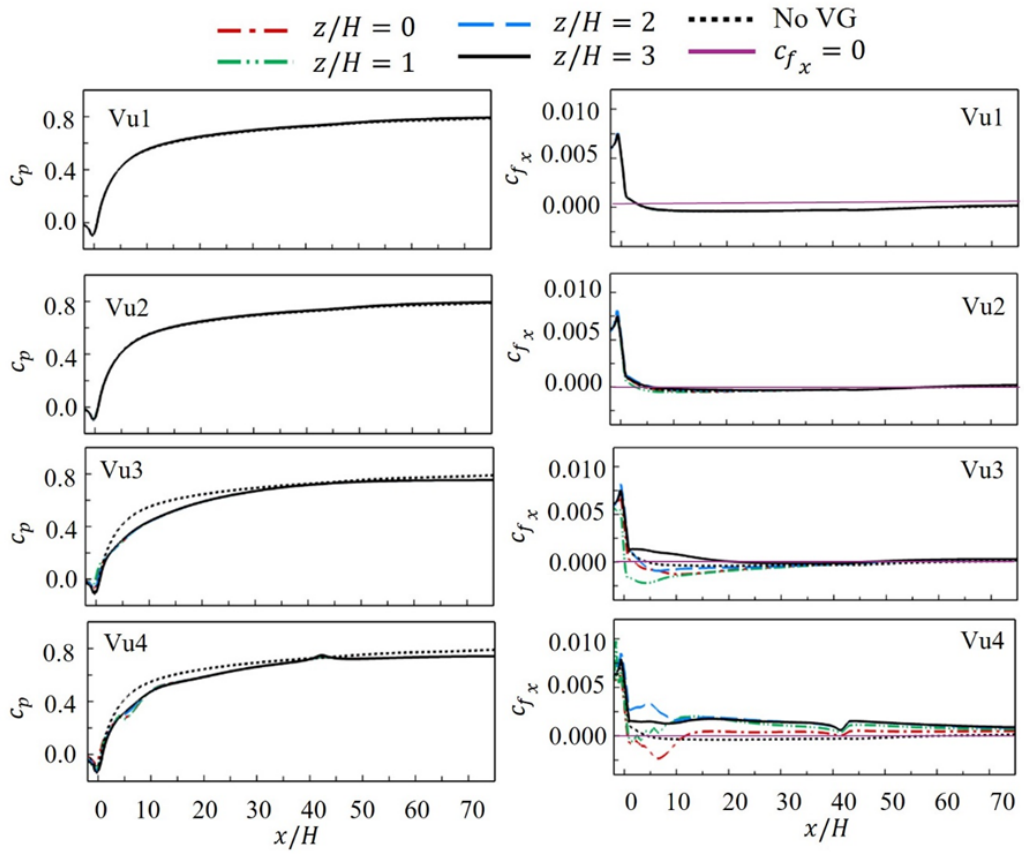

Figure 4.15: Streamwise distributions of c_p and c_{f_x} for the Vu cases.

It is expected that the Vd series of vanes will produce the best improvement since the downwash from the CVP will bring more energetic flow toward the deflected surface. While the discussion later shows that this is the case, there may be other considerations to provide an overall performance figure of merit. The weaker Vd1 and Vd2 vanes do not show a marked influence on the diffuser flow, similar to the previous cases. The surface pressure and axial skin friction distributions appear similar to

those of Vu1 and Vu2 . However, the larger Vd3 and Vd4 cases produce limiting streamlines that flow downstream through large portions of the middle. This is in marked contrast to the corresponding Vu3 and Vu4 cases. The upwash or downwash effects are significant with larger vanes, tending to drive the limiting streamlines to flow downstream. This is especially the situation for the Vd4 case where negative values of c_{f_x} are small and found in the outboard locations. The strong downstream limiting flow in the middle portion of the diverging surface and the weak upstream limiting flow on both sides are a consequence of the two foci just after the corner at $x/H = 0$. As remarked earlier for Vu3 and Vu4, this situation adds to the drag for the long diffuser. Thus the use of such vanes may be restricted to short diffusers.

4.4.2.2 Distortion Index and Efficiency

For the present study, a fully-developed turbulent flow entered the diffuser. Therefore, there is no boundary layer effect and only the divergence angle. Schlichting [56] indicated that the optimum half-angle lies between a narrow range of $\alpha = 2 - 8$ deg, which can achieve a high diffuser efficiency exceeding 0.9. As discussed in section 4.1, this particular diffuser with a divergence angle of 10 deg produces a mildly separated flow. Thus, it is expected that performance improvements can be achieved through installing VGs.

The DI and η data are presented in Table 4.3. In terms of the DI, the best-performing VGs are R4, Vu3, Vd3 and Vd4. The reduction in distortion index is 20.5, 13.9, 21.8, and 46.3 percent, respectively. It can also be noted that some of these VGs such as R2 and Vu4 increase the DI, rendering them ineffective. As expected, the presence of VGs reduced the diffuser efficiency. However, due to the additional blockage created by the VGs, the efficiency of the diffuser with them was less than

the baseline case. In particular, also considering the DI, it appears that Vd3 and Vd4 are suitable candidates for improving the performance of this diffuser.

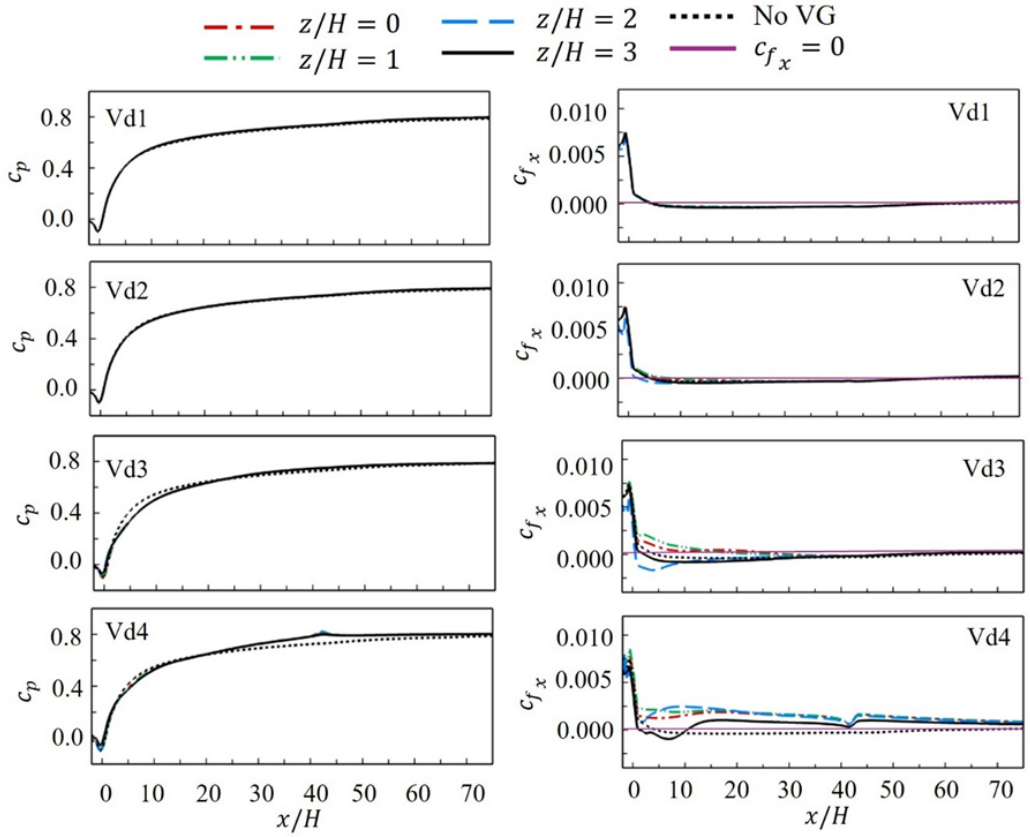

Figure 4.16: Streamwise distributions of c_p and c_{f_x} for the Vd cases.

Table 4.3: VG performance.

	no VG	R1	R2	R3	R4	Vu1	Vu2	Vu3	Vu4	Vd1	Vd2	Vd3	Vd4
DI	0.151	0.148	0.164	0.139	0.120	0.157	0.155	0.130	0.179	0.156	0.157	0.118	0.081
η_D	0.785	0.765	0.724	0.725	0.767	0.752	0.747	0.730	0.760	0.752	0.747	0.745	0.776

4.4.3 Control Volume Analysis

As discussed in the above section, the introduction of a VG causes a change in the pressure and skin friction distribution. These changes, together with those at the entrance and exit planes, determine the effectiveness of the VGs in improving diffuser performance, which can be characterized by the reduction of total drag. A control volume analysis is used to determine the total drag through a momentum balance; see, for example, [90].

A control volume is constructed to include the VGs and the separation region within it. Since the VGs are included in the control volume, no changes in the control volume formulation are needed to account for the size of the VGs. Figure 4.17 shows a schematic of the control volume. The upstream face of the control volume ADCB (1) is located at $x/H = -10$. The downstream face EHGF = (2) is allowed to displace axially $x/H = \{60, 70, 2\}$, thereby allowing the effect of the streamwise extent of the control volume on the total drag to be examined. The spanwise boundaries of the control volume are marked by the faces AEHD and BCGF. The faces DHGC and ABFE are the boundaries on the flat wall and the deflected wall, respectively.

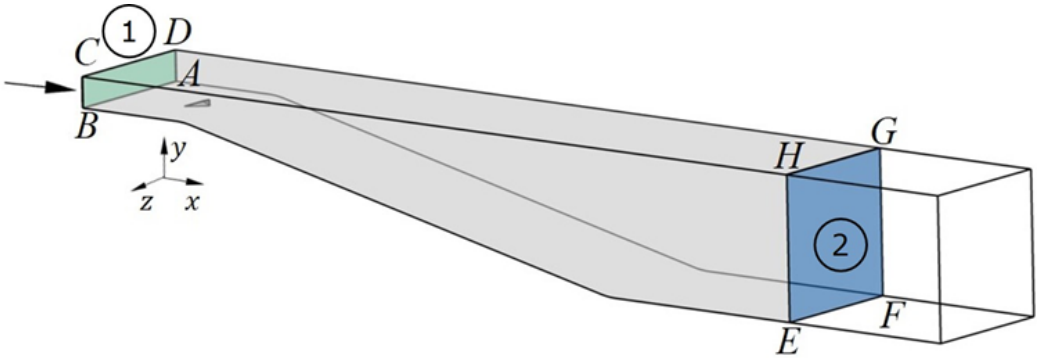

Figure 4.17: Schematic of the control volume.

Consider for the moment an axisymmetric diffuser. A control volume analysis will consider the drag to arise from the reaction to the friction and pressure on the conical frustum. By analogy, the axial friction and pressure forces on the DCGH and ABFE are included in the drag D. The x momentum balance yields

$$D = \int_1 \left(\rho u^2 + p\right) dydz - \int_2 \left(\rho u^2 + p\right) dydz \tag{4.12}$$

This approach is convenient for the present study to account for the effect of the VGs on friction and pressure drag within a diffuser channel. For ease of comparison, the reduction in total drag is represented as a non-dimensional drag parameter

$$\Delta C_D = \frac{D_{VG} - D_{noVG}}{\frac{1}{2}\rho U^2 A} \tag{4.13}$$

where U is the average velocity at the entrance ABCD and A is the projected area DCGH. The drag parameter is plotted for the four different ramp cases as shown in Fig. 4.18, The value of ΔC_D is positive for all the ramps throughout the streamwise locations. This indicates that the ramps are not effective in reducing the total drag. For the streamwise location considered, ΔC_D for R1 and R2 reaches a constant value, indicating that these ramps add to the drag. However, ΔC_D for R3 and R4 show slight decreases. Note that R3 also presents a reduction in the separation region, but this by itself is insufficient to reduce the total drag. The interference drag from these larger ramps exceeds any benefit from their presence.

Figures 4.19 and 4.20 show the incremental drag coefficient ΔC_D for Vu and Vd types of vanes. The incremental drag coefficient for these types of VG is far lower than for the ramps. The plots show that the drag increments for $\{\mathrm{Vu3}, \mathrm{Vu4}\}$ and $\{\mathrm{Vd1}, \mathrm{Vd2}, \mathrm{Vd3}\}$ are the same, indicating an asymptotic behavior in the downstream distances considered. Of specific interest are Vu1 and Vd4, which show no increase

at all. This means that the drag induced by these devices is balanced by their flow separation control benefits. While there did not appear to be any benefit in terms of drag, further consideration is provided below on the potential of VGs to reduce distortion.

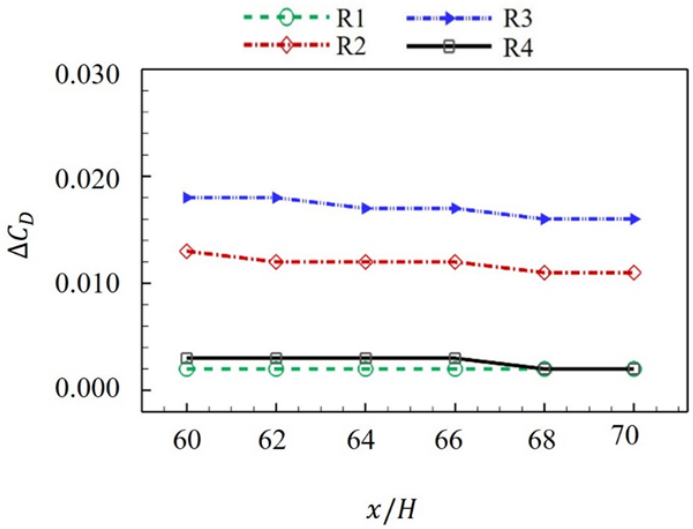

Figure 4.18: ΔC_D versus x/H for the ramp cases.

4.4.4 Summary

The mildly separated flow through an asymmetric diffuser was simulated using a steady RANS approach. The velocity profiles, surface pressure, and skin friction were validated against other investigators' experimental and LES results. Despite the slight over prediction of separation region size, the plots agreed well with the reference documents. To suppress flow separation and to improve pressure recovery, a single vortex generator, either in the shape of a ramp or as a pair of vanes, was deployed at an upstream location of the diffuser inlet. Even though some of the ramp-type VGs were able to reduce the separation zone, this was not sufficient to reduce the total

drag. When the size of the ramp was increased, it created excessive blockage to the flow, which eventually resulted in higher device drag.

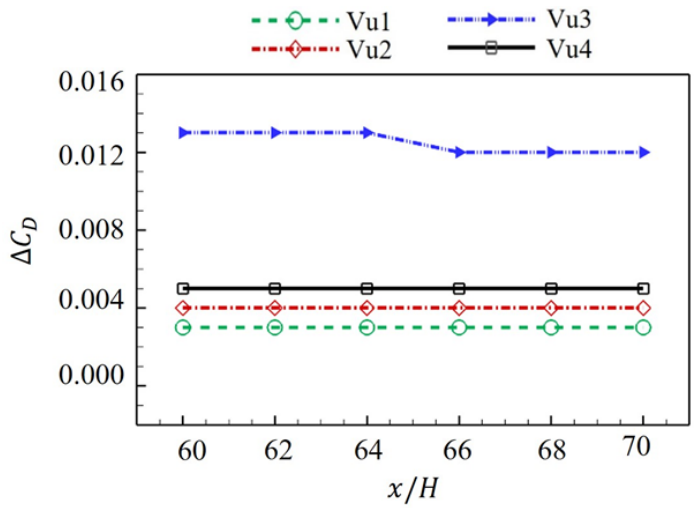

Figure 4.19: ΔC_D versus x/H for the Vu ramp cases.

Vanes that induced upwash and downwash at the diffuser midplane were also examined. The performance of the upwash vanes in terms of the distortion index and diffuser efficiency is poor for all cases studied. However, the performance of vanes that induced downwash in the channel between them was generally good, with the best performance achieved by the largest vanes studied. The vanes Vd3 and Vd4 were able to reduce the distortion index by 21 and 46 percent, respectively. The largest vane also yielded no change in total drag. Even though the vanes were of the same scale as that of the ramps, they offered less resistance to the flow due to the presence of the channel between the vanes. This may be a reason why the vanes perform slightly better than ramps in terms of drag reduction.

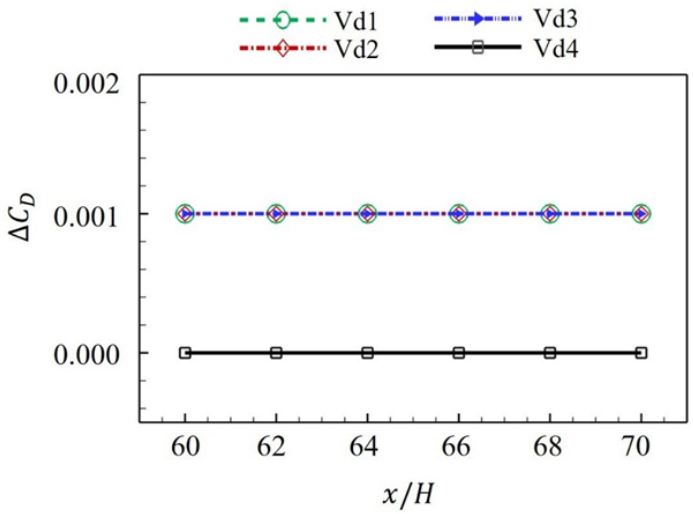

Figure 4.20: ΔC_D versus x/H for the Vd ramp cases.

CHAPTER 5

DYNAMICS OF SEPARATED FLOWS IN DIFFUSERS USING LES

5.1 Case Description

To facilitate comparison with diffuser flow under adverse pressure gradients and to understand the effect of adverse pressure gradient, initial simulations analyzed flow through a straight channel, both with and without VGs. Figure 5.1a shows the computational domain of the straight channel. The half-height of the channel, denoted as H, is 7.5 mm and serves as the reference length scale. The domain dimensions are 15 mm in height, 60 mm in width, and 600 mm in length, corresponding to $2H, 8H$, and $80H$, respectively.

To induce mildly separated flow, an asymmetric diffuser, depicted in Fig. 5.1b, was employed in this study. The geometry and computational domain are consistent with those in previous studies by Buice et al. [86] and Kaltenbach et al. [87]. Understanding the flow dynamics in the diffuser prior to the deployment of VGs is essential for assessing the effects of the VGs. Consequently, an initial simulation without VGs was performed to validate the solver and explore the nature of the separation region. The computational domain includes a constant-area inlet channel, measuring $2H$ in height, $8H$ in width, and $5H$ in length, followed by a divergent section with a 10-degree expansion angle and a constant-area tail duct. The total streamwise extent of the computational domain is $80H$, matching that of the straight channel. The coordinate origin is set at the diverging point of the deflected wall. According to studies by Patterson [110], rounding the corners can enhance diffuser performance;

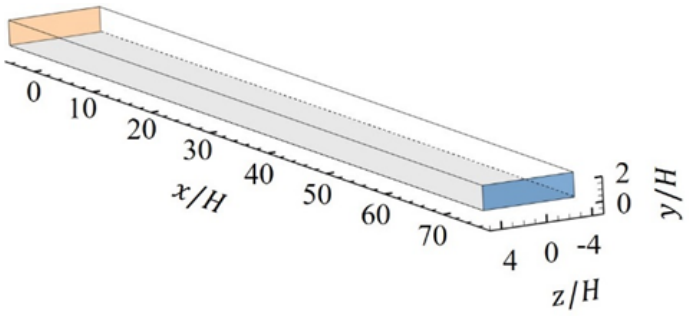

(a) Straight channel

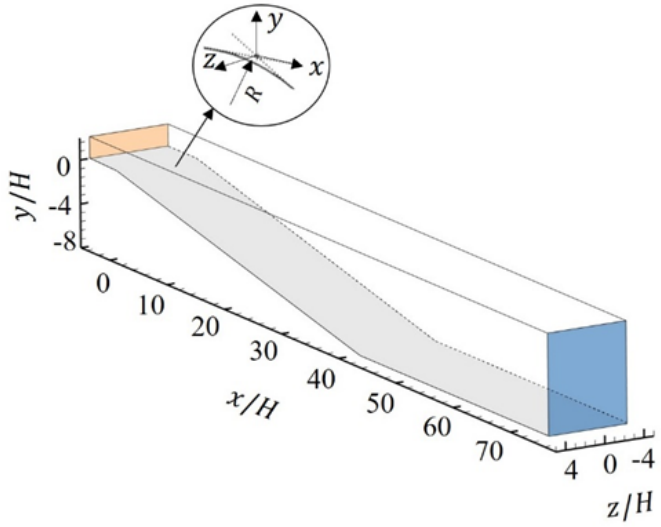

(b) Asymmetric diffuser

Figure 5.1: Computational domain: (a) straight channel and (b) asymmetric diffuser

hence, both upstream and downstream corners along the deflected wall were rounded with a radius of $8.6H$ [87].

Investigations conducted by Lu et al. [111] identified two VG configurations that suppress flow separation and enhance diffuser performance. Figure 5.2 is a schematic of the vane-type VGs selected for this study. Two identical vanes measure $0.2H$ in height, $0.8H$ in length, and have a thickness of 0.3 mm [101]. They are positioned with their trailing edges at a streamwise location of $-2H$. The vanes are arranged in a tapered configuration, with their leading edges set at an angle of attack of 22

degrees relative to the incoming flow. Due to their compact dimensions, these vanes induce a weak CVP that is prone to breakdown, which prompted their selection for investigating vortex breakdown in the current study.

For all the cases mentioned, periodic boundary conditions were applied to the spanwise planes of the computational domain, while an outflow boundary condition was imposed at the outlet plane. The surfaces of the vanes, along with the top and bottom walls of the domain, were treated as no-slip surfaces. To establish the inlet conditions for the LES simulations, a precursor steady RANS simulation of an unillustrated straight channel was conducted using a pressure-based flow solver and the SST (shear-stress transport) $k - \omega$ turbulence model [94]. A uniform velocity of $U_0 = 20$ m/s and a turbulence intensity of 2% were implemented at the channel inlet. This channel was designed with a length of 2 m to ensure a fully developed turbulent flow at the exit. Flow conditions, including velocity components, turbulence intensity, and turbulence dissipation rate, were extracted from a plane located 1.65 m downstream from the channel entrance [87]. These conditions were then used as the inlet conditions for the LES simulations.

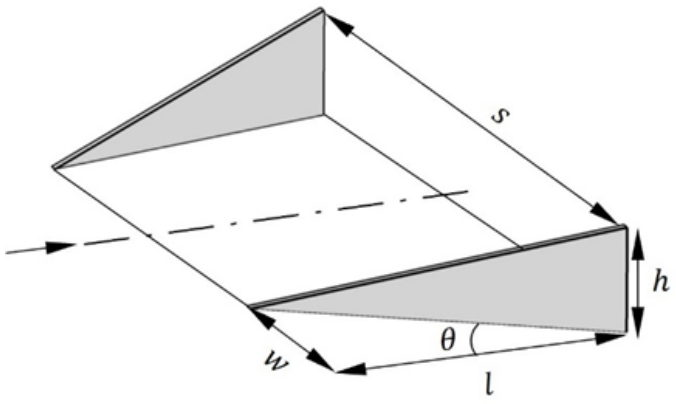

Figure 5.2: Vane-type VGs

5.2 Model Validation and Verification

5.2.1 Grid Generation and Grid Independence Study

The computational domain was partitioned into several subdomains to enhance control over the grid generation process. For cases without VGs, structured grids were used throughout the domain due to the simplicity of the geometry. However, the sharp edges of the vanes in cases with VGs posed challenges for structured grid implementation. To avoid highly skewed cells near the vanes, unstructured grids were utilized in the blocks adjacent to the vanes, while structured grids were maintained in the rest of the domain. Figure 5.3 shows the grid distributions on the spanwise center plane of the diffuser, a three-dimensional view of the grids at the diffuser entrance, and a close-up view of the unstructured grids near the vanes.

The wall shear stress at a streamwise location of $-4H$, located upstream of the vanes, was used to determine the friction velocity and consequently establish the initial grid spacing. The initial grid spacing near the walls was set at 0.01 mm , corresponding to a wall distance of $y^+ = 1$. To ensure a smooth and monotonic distribution of grids while refining them in regions of steep flow gradients, a monotonic rational quadratic spline (MRQS) [102] distribution was employed in the wall-normal and streamwise directions. A comprehensive grid independence study, detailed in a previous paper [111], is omitted here for brevity. Table 5.1 summarizes the number of cells and the average grid spacings in the streamwise, wall-normal, and spanwise directions for all cases discussed in the subsequent sections. These grid parameters are comparable to those used in the LES study by Kaltenbach et al. [87], also presented in Table 5.1. Assuming the largest eddies in the flowfield have a size comparable to half the inlet channel height, H, the Taylor microscale can be estimated as $\lambda = H \cdot \sqrt{15}\,(\mathrm{Re}_H)^{-\frac{1}{2}} = 2.9 \times 10^{-4}$ m, where $\mathrm{Re}_H = \rho U_0 H/\mu = 1.0 \times 10^4$. The grid

resolution in all cases is sufficient to resolve flow structures larger than the Taylor microscale.

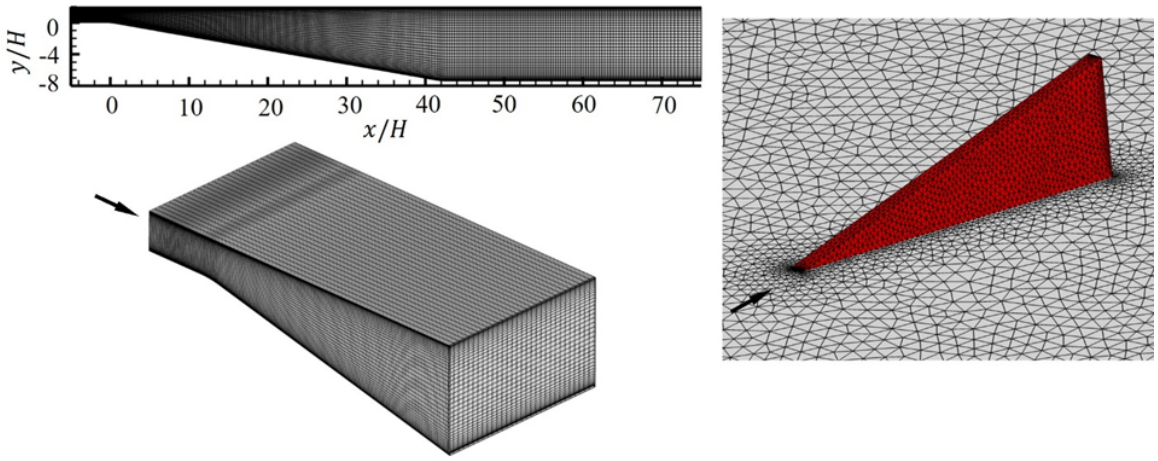

Figure 5.3: Grid distribution in the asymmetric diffuser and near a vane

Table 5.1: Grid information.

Cases	$N_x \times N_y \times N_z$	Average grid spacing $\left(\frac{\Delta x}{H} \times \frac{\Delta y}{H} \times \frac{\Delta z}{H}\right)$	$\Delta x/H$					$\frac{\Delta z}{H}$
			$\frac{x}{H} = -5$	0	10	30	50	
straight channel	$365 \times 70 \times 130$	$0.22 \times 0.028 \times 0.062$	0.06	0.04	0.17	0.26	0.46	0.062
straight channel with VGs	$365 \times 70 \times 130$	$0.22 \times 0.028 \times 0.062$	0.06	0.04	0.17	0.26	0.46	0.062
diffuser	$375 \times 70 \times 130$	$0.21 \times 0.028 \times 0.062$	0.06	0.04	0.17	0.24	0.48	0.062
diffuser with VGs	$365 \times 70 \times 130$	$0.22 \times 0.028 \times 0.062$	0.06	0.04	0.17	0.26	0.46	0.062
Kaltenbach et al. [2]	$352 \times 64 \times 128$	$0.22 \times 0.031 \times 0.063$	0.063	0.052	0.17	0.41	0.60	0.063

5.2.2 Model Validation

Using a diffuser length of 600 mm and a uniform velocity of $U_0 = 20$ m/s, the flow-through time within the computational domain was estimated to be 0.03 s . In this study, all the LES cases were computed for more than six flow-through times. Analysis of preliminary simulations revealed a transient phase during the initial flow-

through time. Consequently, data recorded within this period was disregarded when calculating time-averaged properties. The time steps in all LES cases are fixed at 4×10^{-6} s, a value less than the Taylor microscale $t_\lambda = \lambda/U_0 = 1.5 \times 10^{-5}$ s.

Figure 5.4 compares the normalized time-averaged streamwise velocity profiles at various streamwise locations among the current LES case, a previous RANS study [111], experimental data from Buice et al. [86], and LES results from Kaltenbach et al. [87]. The velocity profiles in the constant-area inlet channel and tail duct exhibit good agreement with the results from [87, 111, 112]. In the divergent section, good agreement is observed in the near-wall region, whereas noticeable differences are observed in the center region. This deviation can be attributed to the relatively coarse grid in the regions away from the walls. Given that the focus of the present study is on the influence of downwash and vortex breakdown on flow separation control in the diffuser-both occurring close to the bottom wall—a refined grid is implemented in this region to capture the physical phenomena accurately. The maximum deviation, approximately 16%, is observed at a location $8H$ above the bottom wall in the divergent section. Since this region is away from the separation zone, it is considered safe to proceed with the simulation without compromising the discussion on separation control.

5.3 Diffuser Flow without VGs

5.3.1 Flow Characteristics

Figure 5.5 shows the contours of instantaneous streamwise velocity, u, on the mid-span plane in the straight channel and the diffuser, respectively. In the straight channel, where no adverse pressure gradient is present, the flow remains attached to the top and bottom walls. A discussion of turbulence activities will follow later in

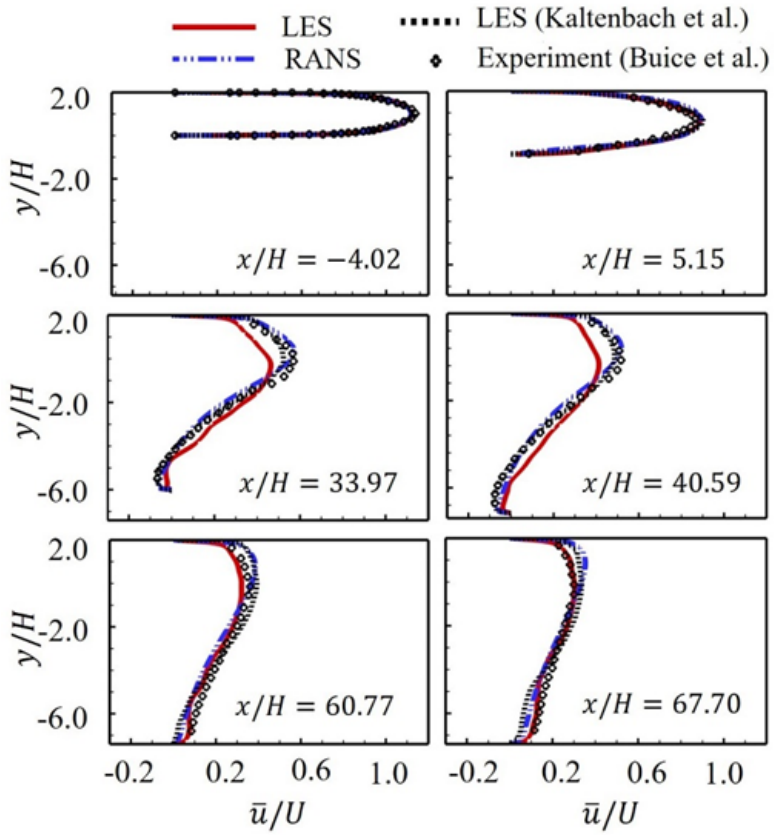

Figure 5.4: Profiles of normalized time-averaged streamwise velocity at different streamwise locations for the diffuser case.

this section. In the diffuser, the flow encounters an adverse pressure gradient in the streamwise direction, resulting in mild flow separation. To identify the separation region, Fig. 5.5b marks the iso-lines of $u = 0$ with solid black lines. Small recirculation regions are evident in the early divergent section at $x = 4H$, an observation that aligns with previous findings by Kaltenbach et al. [87]. Downstream of these intermittent small recirculation regions, a substantial recirculation zone emerges, exhibiting temporal variations in both its shape and extent. As shown in Fig. 5.5b this primary recirculation zone indicates that near-wall flow separates at $x = 12H$ and reattaches at $x = 58H$.

To better understand flow separation in the diffuser, Fig. 5.6 shows the contours of time-averaged streamwise velocity, $\bar{u}$, and wall-normal velocity, $\bar{v}$. The time-averaging process spanned 0.12 s . Due to the nature of time averaging, certain small recirculation regions within the flowfield are eliminated. Consequently, the size of the separation region identified from a specific contour of instantaneous velocities may slightly differ from that obtained from the contour of time-averaged velocities. In the divergent section, flow separation occurs at a distance of $16H$ from the diverging point, and reattachment takes place at $58H$. Hence, the separation region spans a streamwise extent of $42H$, aligning closely with the findings of Buice et al. [86]. When comparing configurations with sharp versus rounded corners, employing rounded corners at the junction between the inlet channel and the divergent section facilitates a more gradual interaction of the flow with the divergence, thereby mitigating flow separation at the corner [110]. Regardless of the corner's shape, the divergence introduces a wall-normal pressure gradient that creates a low pressure region near the wall and a high-pressure region farther from the wall. Consequently, fluid tends to move towards the wall, resulting in a negative time-averaged wall-normal velocity, $\bar{v}$, as observed by the dark blue region near the corner in the contour of $\bar{v}$. This phenomenon is supported by previous investigations [86, 87, 111] in the region near the corner.

5.3.2 Analysis of Turbulence Events

In both the straight channel and the diffuser, instantaneous data are recorded at multiple locations both near the bottom wall and in the diffuser center. Following the quadrant analysis method outlined by Wallace et al. [113, 114, 115], the velocity fluctuations u' and v' at each probe are calculated and normalized by their respective standard deviations, denoted as $\sigma_{u'}$ and $\sigma_{v'}$, to analyze local turbulence events. Based

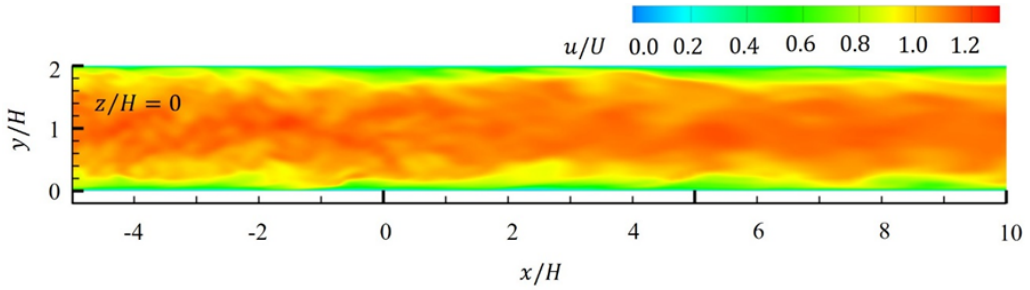

(a) Straight channel

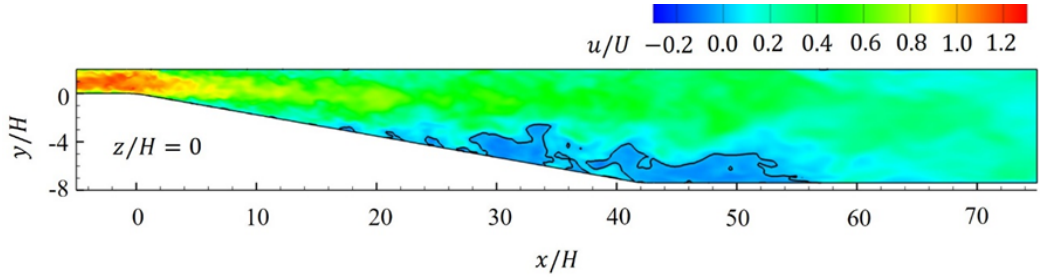

(b) Diffuser

Figure 5.5: Contour of instantaneous streamwise velocity (a) in the straight channel and (b) in the diffuser.

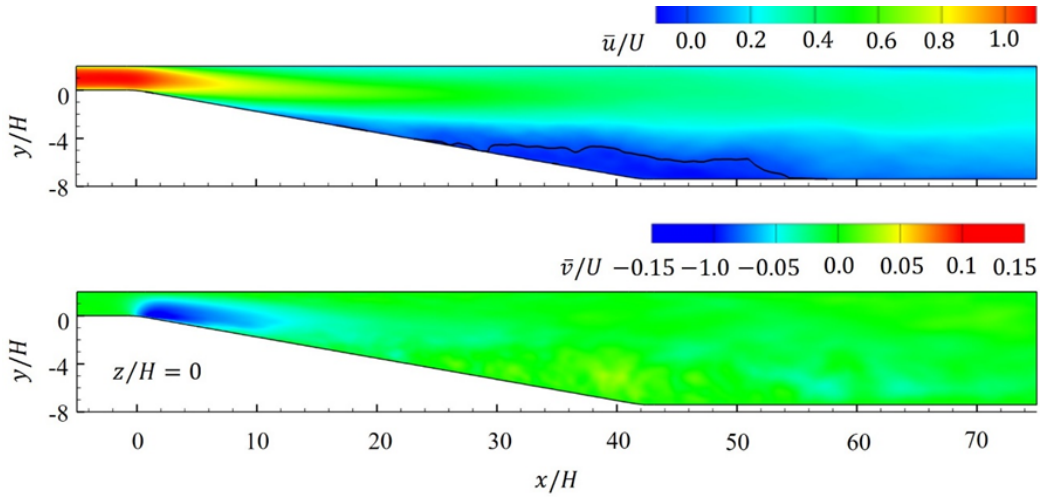

Figure 5.6: Contours of time-averaged streamwise and transverse velocities in diffuser

on the signs of these velocity fluctuations, fluid motions are categorized into four quadrants representing distinct turbulence events: outward interactions (Q_1), ejection (Q_2), inward interactions (Q_3), and sweep (Q_4). Figure 5.7a illustrates these events

near a wall. To quantify the contribution of each event to overall turbulence activity, the joint probability density function (JPDF) of u' and v' is computed at each probe. Figures 5.7b and 5.7c show the distributions of these JPDFs, normalized by the maximum values at each probe location. Additionally, the unnormalized JPDFs are integrated over each quadrant, and the contributions from the four types of turbulence events are quantified, with values for Q_1, Q_2, Q_3, and Q_4 marked on the figures.

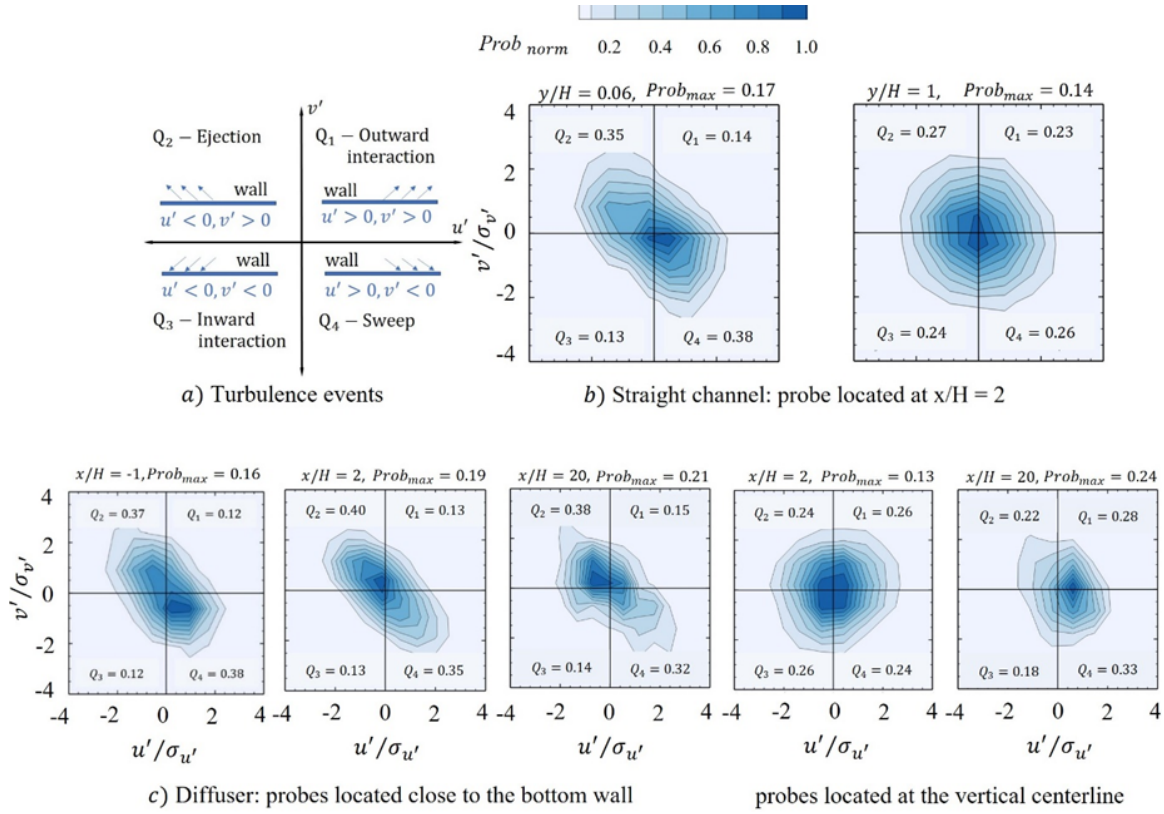

Figure 5.7: Contours of JPDFs and quadrant contributions of fluctuating velocities at probes located on the mid-span plane: (a) turbulence events (b) in the straight channel (top row), and (c) in the diffuser (bottom row).

In the straight channel, probes at the streamwise location of $x = 2H$ are of particular interest, as this location coincides with the breakdown of trailing vortices from the VG when deployed. At the probe positioned $0.06H$ above the bottom wall,

approximately 73% of the total turbulence activity is attributed to ejection and sweep events. The flowfield near the wall contains vortical structures that undergo continuous bursting, leading to increased ejection and sweep events [116]. However, these vortical structures are absent at locations away from the wall, resulting in a diminished occurrence of pronounced ejection and sweep events at $y/H = 1$. Instead, there is a nearly symmetric distribution of quadrant events, and all four turbulence events contribute nearly equally to the total turbulence activity, consistent with observations in Hajaali et al. [117].

In the diffuser, as the flow approaches the divergent section, the ejection and sweep events are slightly intensified, as evidenced at $x = -H$. Upon encountering an adverse pressure gradient, it becomes challenging for the flow structures near the wall to progress in the streamwise direction, leading to increased bursting of these structures. Consequently, there is an enhancement in the contribution from ejection and sweep events. At $x = 2H$, the ejection event exhibits an approximate 5% increase compared to that in the straight channel. However, the over contribution of ejection and sweep events is about 75%, only marginally higher than in the straight channel. The results otherwise closely resemble those in the straight channel. The similarities in the JPDF shapes and the quadrant contributions between the straight channel and the diffuser can be attributed to the mildly separated flow present in the diffuser. In the separated region at $x = 20H$, ejection becomes the dominant event near the wall, while sweep and outward interaction are more pronounced near the diffuser centerline.

5.4 Diffuser Flow with VGs

5.4.1 Flow Characteristics

To suppress flow separation, a pair of vane-type VGs, introduced in Section Error! Reference source not found., was deployed upstream of the diverging point of the diffuser. It was hypothesized that the streamwise vortices generated by these vanes would redistribute momentum within the downstream flowfield, thus controlling flow separation. The following sections discuss the modifications in the flowfield resulting from the VGs and investigate the effects of various physical phenomena, including vortex breakdown, on the suppression of flow separation.

Figure 5.8 shows the trailing vortices immediately downstream of the VGs in both the straight channel and the diffuser. Also shown are streamlines on three cross-stream planes at $x/H = -2, 0$, and 2 , specifically for the right vane. In the straight channel, the VG's trailing edge is positioned at a streamwise location of $x/H = -2$ and a spanwise location of $z/H = 1.8$. The streamline patterns reveal downward fluid movements between the vanes, referred to as downwash, and upward fluid movements outside the vanes, known as upwash. In the absence of an adverse pressure gradient, these trailing vortices continue downstream to further stations without significant alterations in their shape or size, as observed by [34]. In the diffuser, the downwash and upwash patterns at the VG trailing edge ($x/H = -2$) closely resemble those in the straight channel. However, at the entrance of the divergent section ($x/H = 0$), upwash is primarily observed immediately outside the vanes. The discussion on the rounded corner elucidates that the divergence of the diffuser induces a downward flow, driven by the wall-normal pressure gradient. Further downstream in the divergent section ($x/H = 2$), the adverse pressure gradient weakens the trailing vortices significantly, causing the fluid to move towards the bottom wall. It is postulated that

vortex breakdown occurs near this streamwise location.

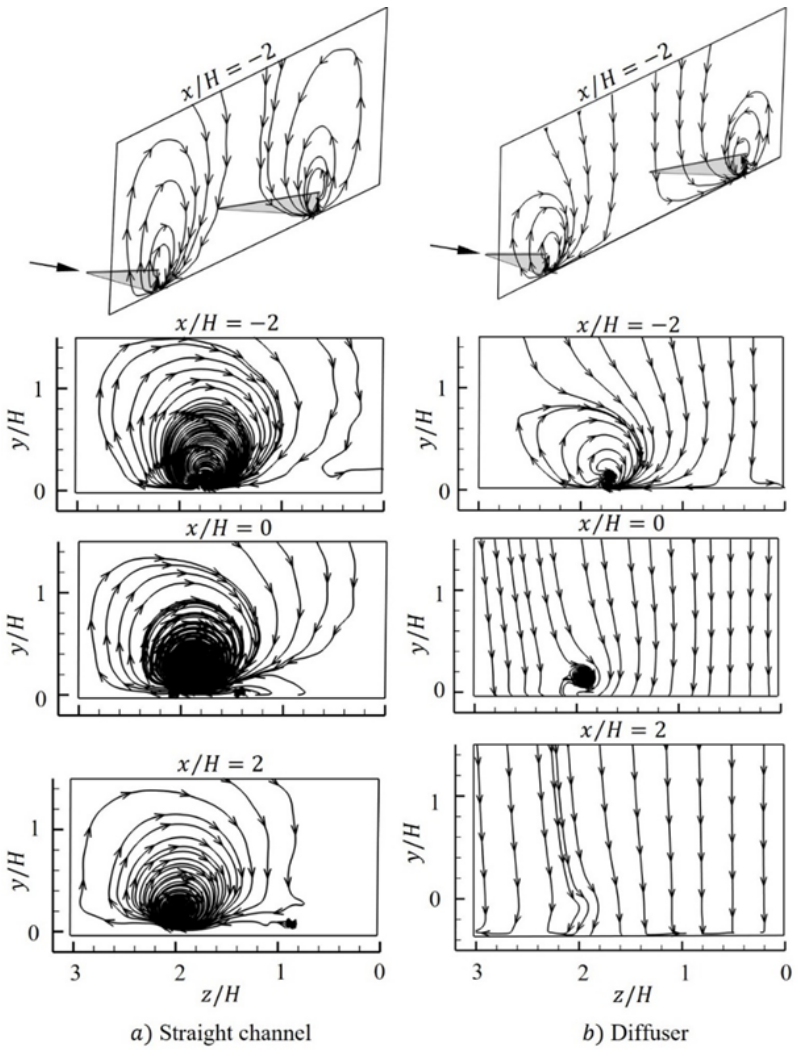

Figure 5.8: Visualization of trailing vortices behind VGs, along with streamlines on three cross-stream planes for the right vane (when viewed from an upstream location): (a) in the straight channel, and (b) in the diffuser

Before addressing the diffuser equipped with VGs, it is crucial to examine the behavior of trailing CVP under zero-pressure gradient conditions. In the current work, a straight channel was used to establish a zero-pressure gradient, and VGs

were installed on the channel's bottom wall. These VGs create a series of CVP, resulting in a flowfield dominated by downwash between the vanes and upwash outside these regions. Figure 5.9 shows the contours of instantaneous streamwise velocity at various spanwise locations in the straight channel with VGs. In regions dominated by downwash ($z/H = 2$), the near-wall fluid exhibits increased kinetic energy due to momentum redistribution, leading to a narrow low-velocity region adjacent to the wall. Conversely, in the upwash-dominated regions ($z/H = 3$), low-velocity streaks appear near the wall, attributable to the upward motion of low-velocity fluid.

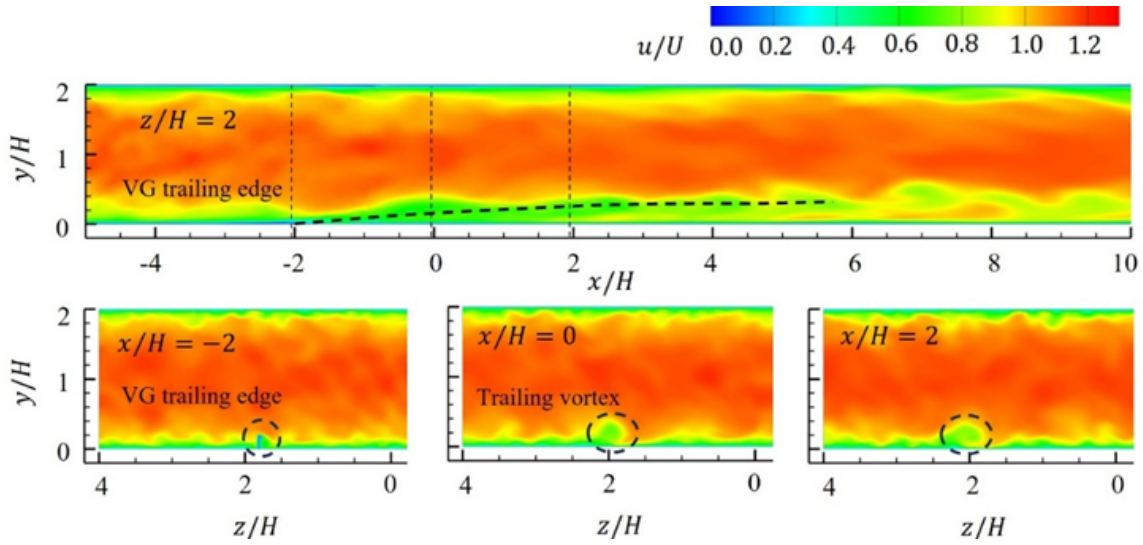

Figure 5.9: Contours of instantaneous streamwise velocity in the straight channel with VGs

In the diffuser-only configuration, the size of the separation region was observed to remain consistent across various spanwise locations, indicating a two-dimensional flowfield. However, the introduction of VGs at the entrance of the divergent section disrupted this two-dimensionality, leading to variations in the extent of separation across different spanwise locations. Figures 5.10 show the contours of instantaneous streamwise velocity at several spanwise locations in the diffuser equipped with VGs,

overlaid with the solid black iso-lines of $u = 0$. Small recirculation regions appear at streamwise locations ranging from $8H$ to $70H$, with the smallest separation region noted at the mid-span. Owing to the temporal variability of these recirculation regions, time-averaged velocity contours, as shown in Fig. 5.11, were used to elucidate the spanwise distribution of the separation region. The separation region is noticeably smaller near the mid-span plane and enlarges at more distant spanwise locations. The mid-span is characterized by a region where the downwash from both vanes contributes almost equally, while at other spanwise stations, the downwash from one vane decreases as it increases from the opposite vane.

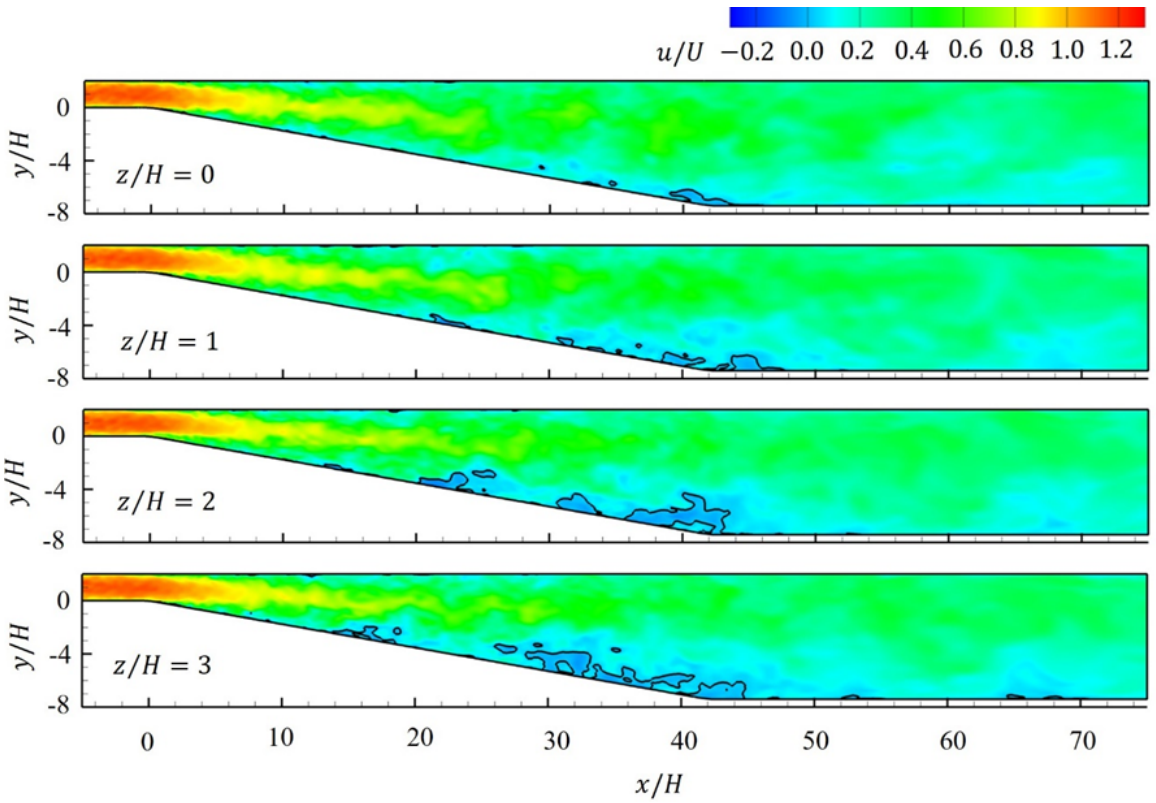

Figure 5.10: Contours of instantaneous streamwise velocity u and isolines of $u = 0$ in the diffuser with VGs

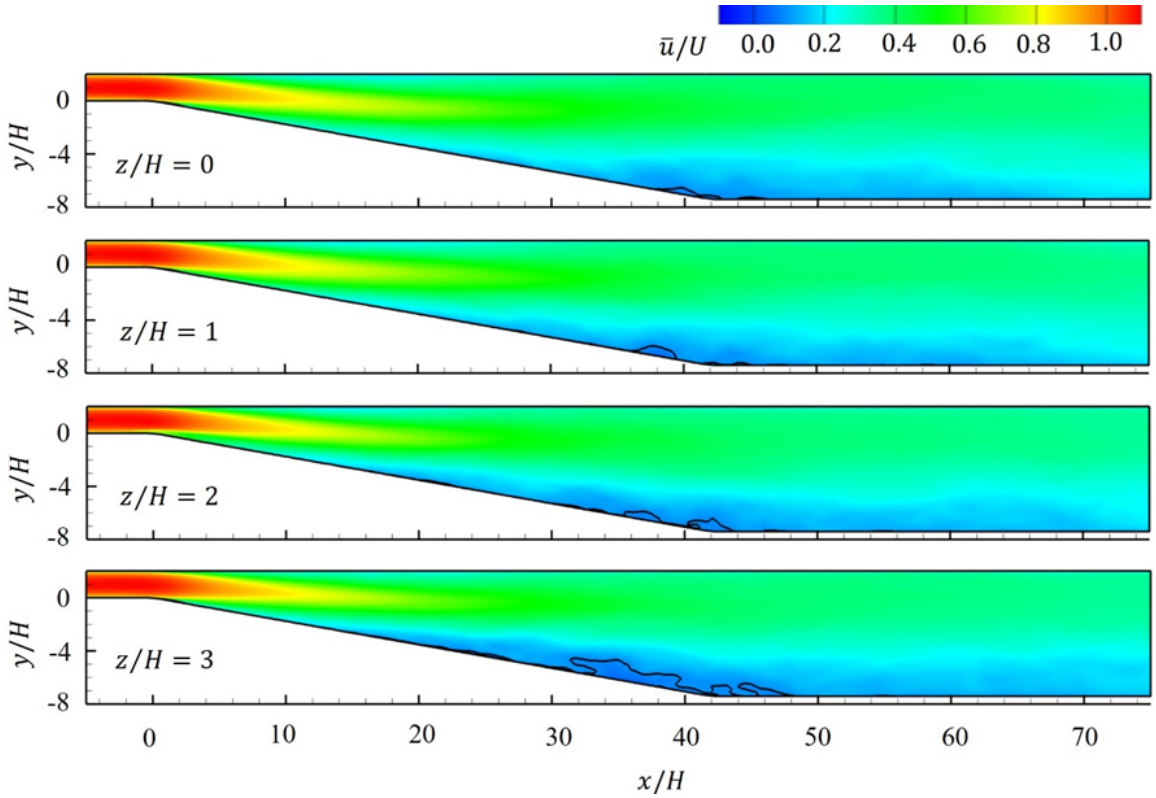

Figure 5.11: Contours of time-averaged streamwise velocity $\bar{u}$ and isolines of $\bar{u} = 0$ in the diffuser with VGs

5.4.2 Analysis of Turbulence Events

The CVP generated by the VGs energizes the near-wall region of the flowfield, thereby reducing separation size. Additionally, the proximity of the CVP to the wall alters the near-wall flowfield, influencing turbulence activity. To further examine these effects, quadrant analysis was employed. Three probe locations were selected near the wall ($0.06H$ above the bottom wall) at streamwise locations of $2H, 3H$, and $4H$, consistent with those in the cases without VG. All these probes were positioned spanwise at $2H$, near the trailing vortex from the right vane.

Under a zero-pressure gradient, Fig. 5.12a shows the JPDF contours and the quadrant contributions in a straight channel with VGs. Compared to Fig. 5.12b,

there is a noticeable alteration in the quadrant contributions, highlighting significant changes in turbulence activity due to the VGs. Near the CVP, the flowfield is dominated by several flow structures (to be detailed in Fig. 5.13). These structures experience pronounced tilting in both the wall-normal and spanwise directions, altering their relative positions to the probe locations. This shift affects the velocity fluctuations and subsequently modifies the turbulence activity. The presence of VGs increases the contributions from inward and outward interaction events. However, a comprehensive understanding of the underlying physics of these phenomena remains outside of the scope of this work. The total contribution of ejection and sweep events was approximately 65%, which is 8% less than in the scenarios without VGs. This reduction in ejection and sweep events corresponds with an 8% increase in outward and inward interaction events.

Under an adverse pressure gradient, the JPDF contours and quadrant contributions in the diffuser equipped with VGs are shown in Fig. 5.12b. The turbulence activity at these probe locations is modified by the adverse pressure gradient imposed by the divergent section of the diffuser. Compared to the straight channel in Fig. 5.12a, the sweep becomes the most prominent event. The contribution of sweep events has increased by $9\%, 5\%$, and 7% at $x = 2H, 3H$, and $4H$, respectively. Overall, sweep events account for an average of 41% of the total turbulence activity at the probe locations. This augmentation in sweep events may arise from potential vortex breakdown, resulting in fluid particle movement towards and away from the wall. It is important to note that sweep events, representing the motion of high-velocity fluid particles toward the probe location, can be considered beneficial in the context of flow separation control. Additionally, a 12% increase in the ejection events was observed at $x = 4H$.

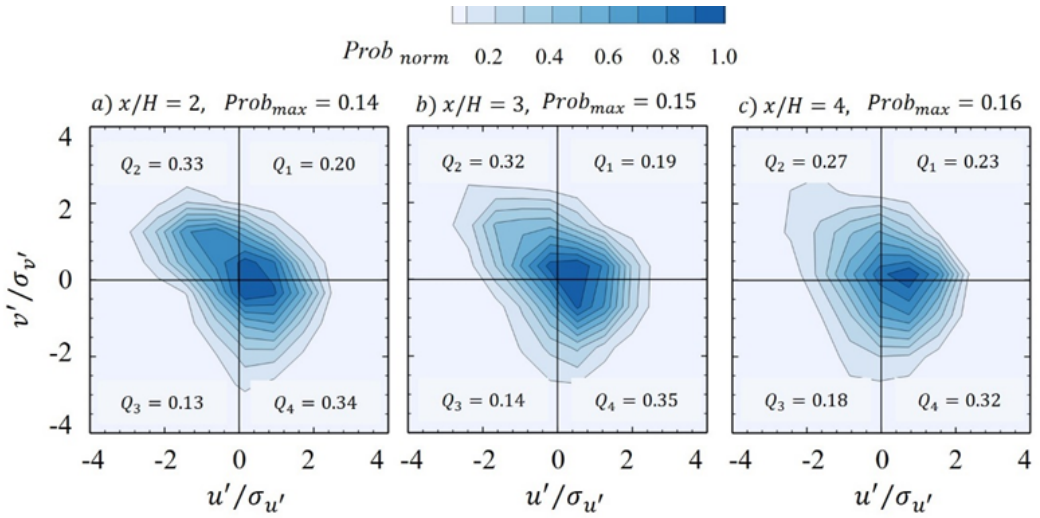

(a) Straight channel

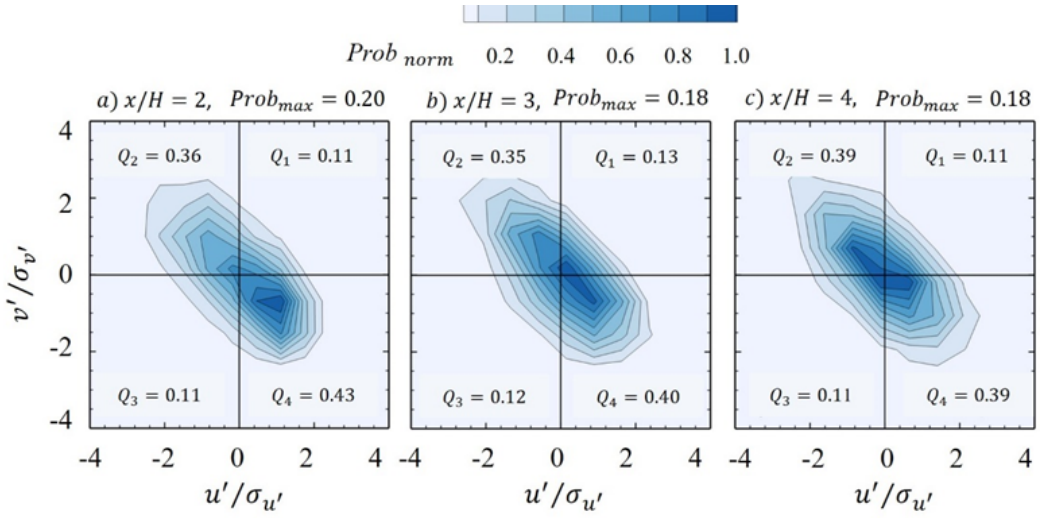

(b) Diffuser

Figure 5.12: Contours of JPDFs and quadrant contributions of fluctuating velocities: (a) in the straight channel with VGs, and (b) in the diffuser with VGs. In both cases, probes are located close to the bottom wall and at a spanwise location near the trailing vortex.

At these near-wall locations, ejection and sweep events accounted for 77% of the total turbulence activity, which is 12% higher than observed in the straight channel with VGs (Fig. 5.12a). The increase in ejection and sweep events may originate from two primary factors: 1) the adverse pressure gradient in the divergent section of the diffuser, and 2) the increased velocity fluctuations stemming from the disintegration of trailing vortices, further detailed in the subsequent section of this manuscript. To specifically assess the contribution of vortex breakdown, an examination of the turbulence within the diffuser-only flow is requisite. The quadrant analysis performed in the diffuser, shown in Fig. 5.7c, indicates that the adverse pressure gradient only slightly contributes to the ejection and sweep events. After compensating for the adverse pressure gradient effects, the contribution of vortex breakdown to the enhanced sweep events is determined to be $8\%, 5\%$, and 5% at $x = 2H, 3H$, and $4H$, respectively. Although not shown here, near the diffuser centerline, the deployment of VGs led to a 7% increase in ejection events and a 5% increase in sweep events. The enhanced prevalence of sweep events highlighted the downward motion of fluid particles due to trailing vortices and their subsequent breakdown.

The following sections present a comprehensive analysis of the vortex breakdown phenomenon and its influence on the downstream flowfield of VGs. A comparative evaluation among three configurations-a straight channel equipped with VGs, a diffuser with VGs, and a diffuser only-is conducted to determine the occurrence of vortex breakdown and its corresponding effects on turbulence activity. Additionally, the TKE production near the anticipated vortex breakdown location is thoroughly investigated.

5.4.3 Vortex Breakdown

Visualization of the trailing vortices emanating from the vanes was achieved by rendering iso-surfaces of the Q-criterion (defined as $Q = \left(\|\Omega\|^2 - \|S\|^2\right)/2$, where Ω is the rotation rate and S is the strain rate), overlaid with two-dimensional streamlines on transverse planes at various streamwise locations. For the sake of clarity, only the trailing vortices stemming from the right vanes are shown. Specific Q-criterion values- 4×10^6 for the straight channel and 1.2×10^7 for the diffuser-were chosen to clearly distinguish the trailing vortices from surrounding flow structures. Figures 5.13 and 5.14 show the visualization results for the straight channel with VGs and the diffuser with VGs, respectively. These trailing vortices, surrounded by multiple flow structures, significantly impact turbulence activity near the wall. As previously noted by Lödgeberg et al. [34], trailing vortices in the straight channel appear persistent until farther downstream locations. However, in the diffuser, the vortices were observed to disintegrate at a streamwise location of approximately $2H$, marked by a steep change in the streamline pattern. Under adverse pressure gradient conditions, trailing vortices can undergo sudden retardation and exhibit abrupt changes in size and shape. These abrupt changes in vortex structure, consistent with observations by Hall et al. [46], are indicative of possible vortex breakdown. Similar findings were reported by Robinson et al. [118].

To further elucidate the observations from Figs. 5.13 and 5.14, the sizes of the trailing vortices emanating from the right vanes were tracked at various streamwise locations. Figures 5.15 and 5.16show the spatial variations of these vortices in the straight channel and the diffuser with VGs, respectively. As shown in Figs. 5.15 and 5.16, the maximum time-averaged streamwise vorticity, $\bar{\omega}_{x,\max}$, undergoes notable variations across different streamwise locations. To enhance visual interpretation, the

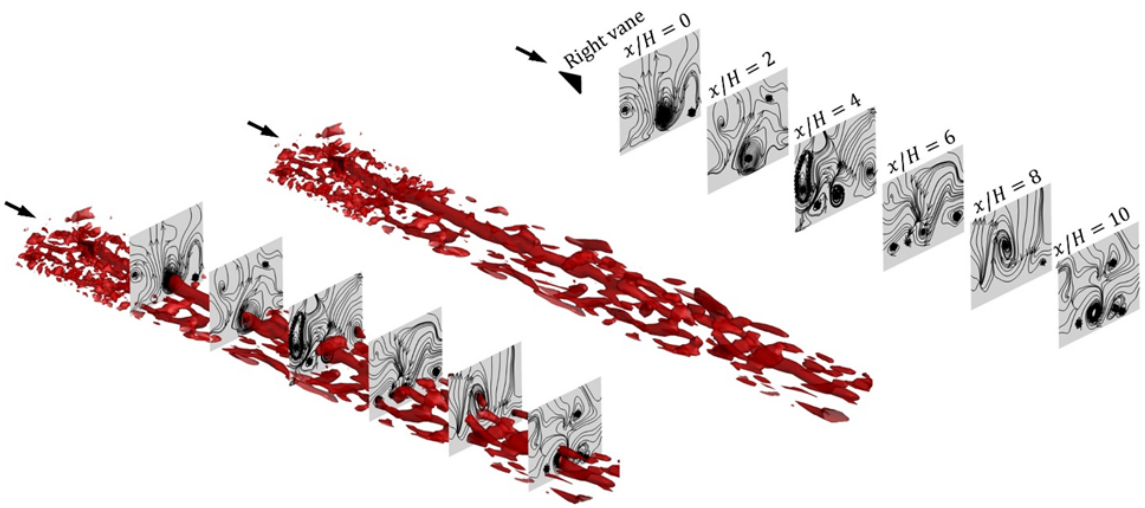

Figure 5.13: Visualization of trailing vortices in the straight channel with VGs: iso-surfaces of $Q = 4 \times 10^6$ and two-dimensional streamlines on transverse planes.

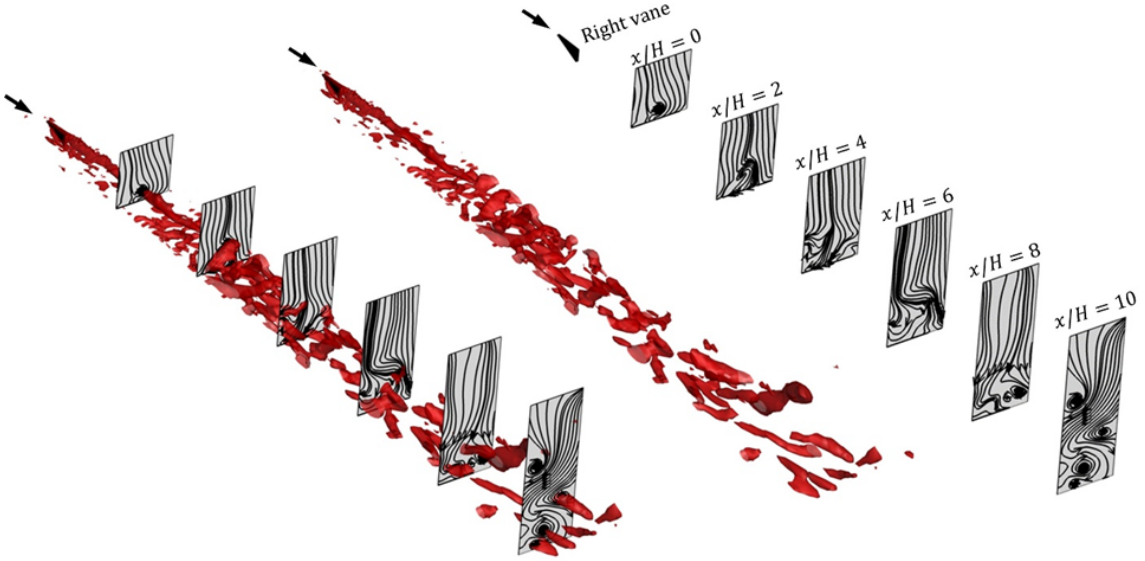

Figure 5.14: Visualization of trailing vortices in the diffuser with VGs: iso-surfaces of $Q = 1.2 \times 10^7$ and two-dimensional streamlines on transverse planes.

time-averaged streamwise vorticity is normalized by its maximum value on the local transverse plane, represented as $\bar{\Omega}_x = \bar{\omega}_x / \bar{\omega}_{x,\max}$. The contours of $\bar{\Omega}_x$ are shown at several streamwise locations to outline the cross-sectional profile of the vortices. The

edge of each vortex at these locations is defined by iso-lines of $\bar{\Omega}_x = 0.2$ (solid black lines), employing a similar criterion to that used by Yao et al. [119] for sizing vortices. This criterion allows the determination of both the horizontal (spanwise) and vertical (wall-normal) dimensions of the vortex, D_1/H and D_2/H, respectively. In the straight channel, the ratios D_1/H and D_2/H are relatively unchanged between adjacent streamwise locations. Conversely, in the diffuser, there are substantial increases-100% in D_1/H and 67% in D_2/H-observed between $x/H = 0$ and 2 [118]. Additionally, the shape of the vortex is significantly distorted in the diffuser, in contrast to its consistent appearance in the straight channel. Integrating observations from the streamline patterns on transverse planes in Fig. 5.14 with the vortex sizes and shapes in Fig. 5.16, the approximate streamwise position of vortex breakdown is identified as $2H$. It is important to note, however, that the location of vortex breakdown may exhibit fluctuations along the streamwise direction [120], reflecting its highly unsteady nature. When these trailing vortices break down, the associated velocity fluctuations modify, consequently altering the turbulence activity at those specific locations, as discussed in Fig. 5.12.

One effect of vortex breakdown is the increase in velocity fluctuations, leading to a subsequent rise in total TKE production. The normalized TKE production at any location in the flowfield can be expressed as follows:

$$\Pi^* = \left(-\overline{u_i{}' u_j'} \frac{\partial \bar{u}_i}{\partial x_j} \right) \frac{H}{U^3} \tag{5.1}$$

where $-\overline{u_i{}' u_j{}'}$ represents the Reynolds stresses, $\partial \bar{u}_i / \partial x_j$ represents the mean strain rate, H is the half-height of the diffuser inlet, and $U = 20$ m/s is the average incoming velocity. In the analysis, only the off-diagonal terms of the Reynolds stress tensor were considered. The normalized TKE production Π^*, includes contributions from

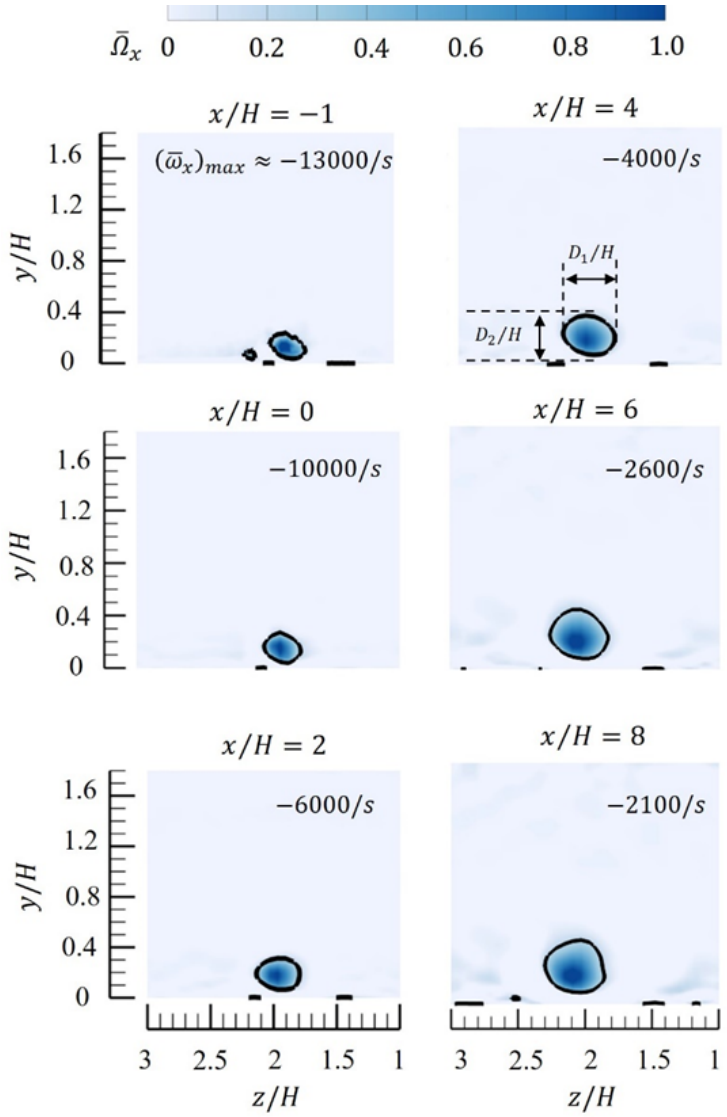

Figure 5.15: Vortex size at different streamwise locations in the straight channel with VGs.

the three components of Reynolds stress and their corresponding mean strain rates, as detailed in reference [121]. It can be decomposed as follows:

$$\Pi^* = [\underbrace{-\overline{u'v'}\left(\frac{\partial \bar{u}}{\partial y} + \frac{\partial \bar{v}}{\partial x}\right)}_{\Pi_{uv}} \underbrace{-\overline{v'w'}\left(\frac{\partial \bar{v}}{\partial z} + \frac{\partial \bar{w}}{\partial y}\right)}_{\Pi_{vw}} \underbrace{-\overline{w'u'}\left(\frac{\partial \bar{w}}{\partial x} + \frac{\partial \bar{u}}{\partial z}\right)}_{\Pi_{wu}}]\frac{H}{U^3} \tag{5.2}$$

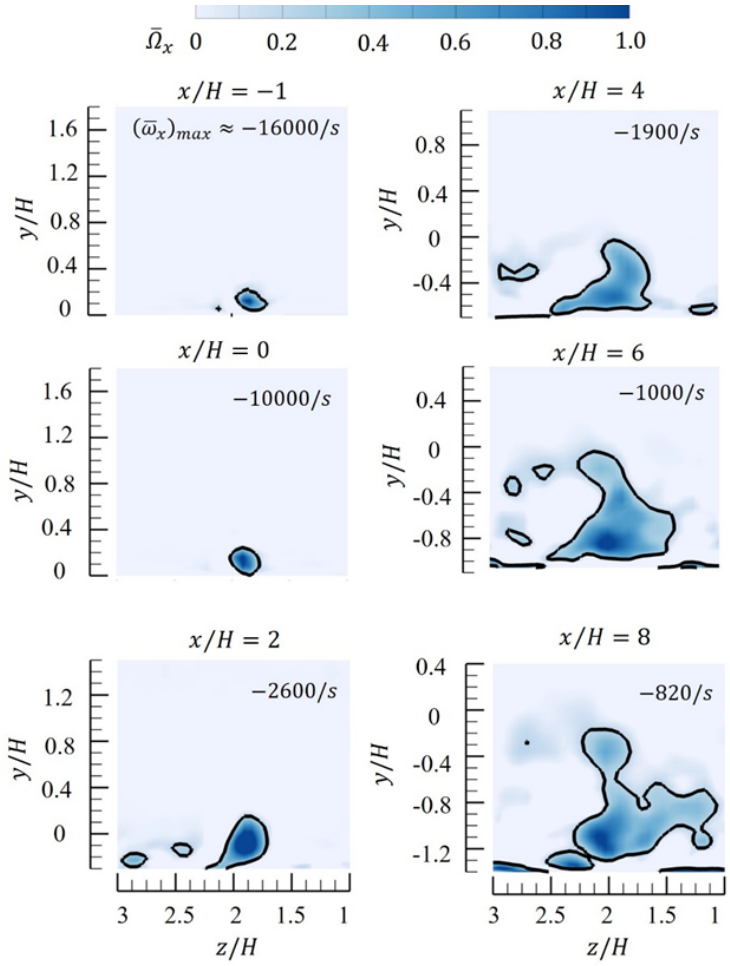

Figure 5.16: Vortex size at different streamwise locations in the diffuser with VGs.

Figure 5.17 shows the contours of Π^* at several spanwise planes. Due to the two-dimensional nature of the flow without VGs, only the Π^* at the mid-span plane is shown in the top image. In all contours presented in Fig 5.17, a peak in Π^* can be observed near the wall. These peaks are attributed to the bursting of alternating low- and high-speed streaks near the wall, commonly observed in wall-bounded turbulent flows and referred to as low-speed streaks (LSS) [116, 122]. A convenient method to visualize LSS is through the contours of $\Omega_y = \omega_y H/U$, the normalized wall-normal component of vorticity. The term $\partial u/\partial z$ in the expression for ω_y captures the vari-

ation of streamwise velocity in the spanwise direction [123], as shown in Fig. 5.18 where the selected plane for visualizing the LSS is located at $y/H = 0.005$.

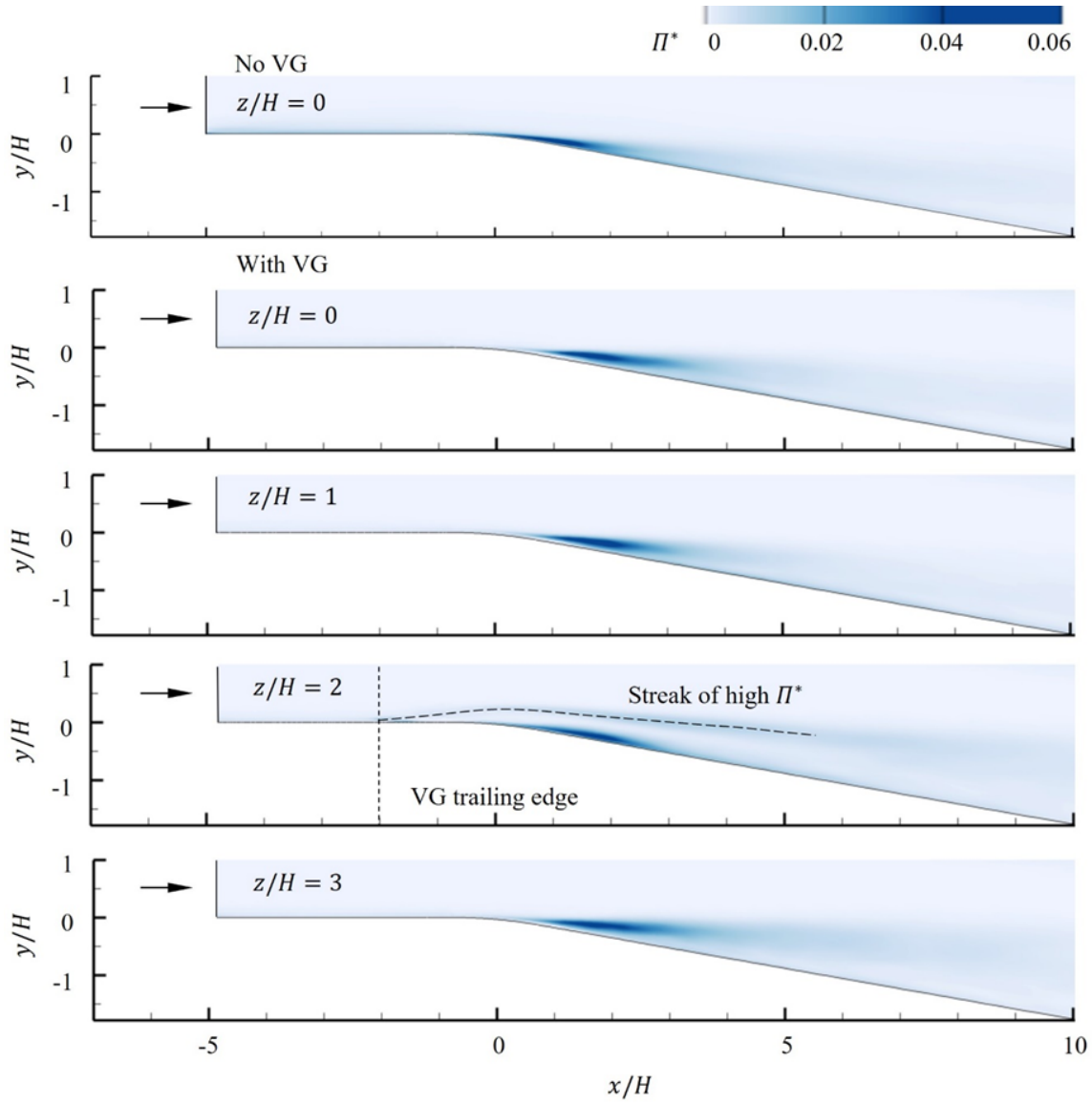

Figure 5.17: Contours of Π^* in the diffuser at different spanwise locations

To provide a detailed analysis, Fig. 5.19 shows the profiles of Π^* at various streamwise ($0H, 2H$ and $4H$) and spanwise ($0H, 1H, 2H$ and $3H$) locations. The

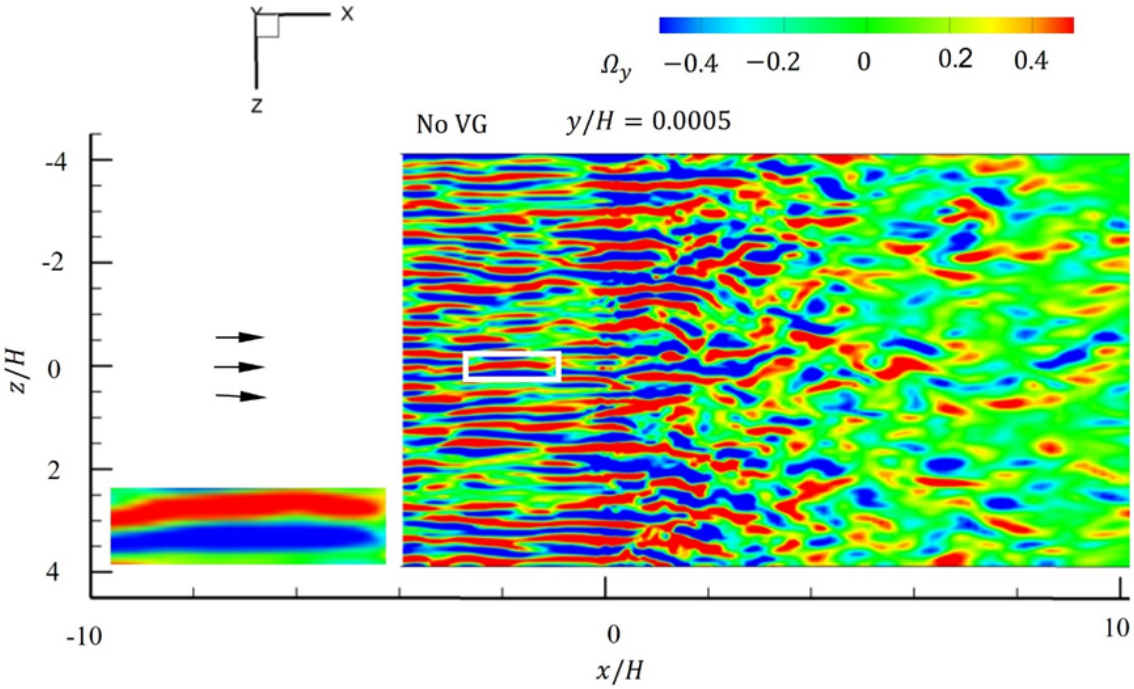

Figure 5.18: Contours of Ω_y near the deflected wall.

streamwise location $0H$ marks the entrance of the divergent section, while the spanwise location $2H$ is proximate to the trailing vortex. Within the straight channel, specifically at the spanwise location close to the trailing vortex ($2H$), an elevation in Π^* was observed. This increase is attributable to heightened velocity fluctuations arising from the presence of trailing vortices. However, these peaks did not exhibit significant enhancement at further spanwise stations. The adverse pressure gradient at the diffuser triggers the breakdown of the LSS and the streamwise vortices emanating from the VG, leading to the amplification of near-wall peaks of Π^*. Particularly near the anticipated vortex breakdown location ($x/H = 2, z/H = 2$), a marked increase in Π^* was noted, likely due to the combined effects of the adverse pressure gradient and vortex breakdown. To isolate the impact of the adverse pressure gradient from that of vortex breakdown, the Π^* profile in the diffuser without VGs (blue line in Fig. 5.19b) serves as a useful comparison. In the diffuser equipped with VGs, the peak Π^*

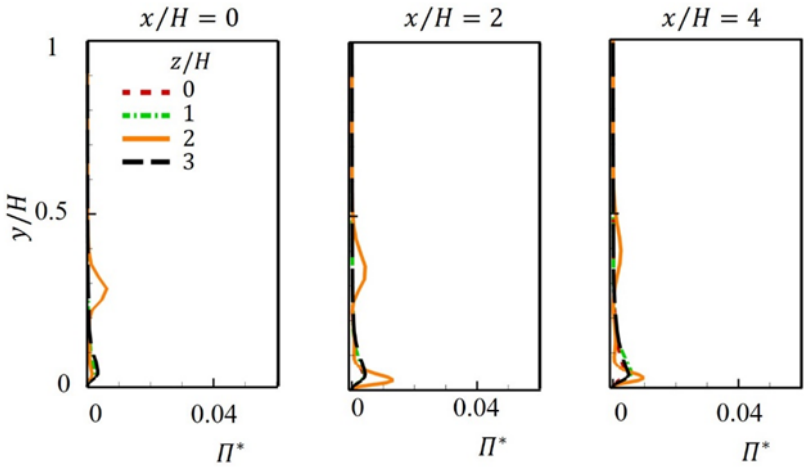

(a) Straight channel

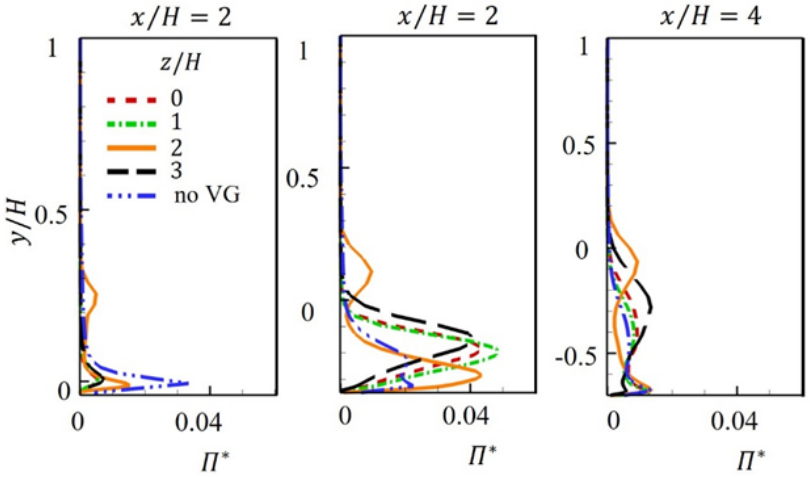

(b) Diffuser

Figure 5.19: Profiles of Π^* at different streamwise and spanwise locations.

value at the vortex breakdown location is twice that observed in the diffuser without VGs, indicating additional TKE production attributable to vortex breakdown.

From the Π^* peaks noted at all considered spanwise locations at $x/H = 2$, it appears that the effect of vortex breakdown at $z/H = 2$ disperses in the spanwise direction. Essentially, the vortex breakdown at the spanwise location $z/H = 2$ causes an increase in TKE production at spanwise locations extending beyond it. The Π^* peaks at all spanwise locations except the breakdown site ($z/H = 2$) also tend to shift

upward in the wall-normal direction by approximately $0.2H$. This upward movement positions the Π^* peaks nearer to the high momentum region within the flowfield, which may be beneficial for flow separation control by aiding in the redistribution of momentum in the wall-normal direction. At the location downstream of the vortex breakdown ($x/H = 4$), the Π^* peak remains evident across all spanwise locations. It is noteworthy that at the diffuser entrance ($x/H = 0$), the peak Π^* value in the absence of VGs is almost double that in the configuration with VGs. This contrast arises because the trailing vortices in the VG configuration energize the LSS, enhancing their resilience against bursting under adverse pressure gradient conditions. In contrast, the LSS in the no-VG setup succumbs to bursting upon encountering the adverse pressure gradient, resulting in a pronounced peak of Π^*. Moreover, another Π^* peak was discerned at locations proximate to the trailing vortices ($y/H \approx 0.2, z/H \approx 2$), as shown in Fig. 5.19. The Π^* contours shown in Fig. 5.17 further reveal a streak of high Π^* originating from the trailing edge of the VG and detectable near the trailing vortices. These elevated Π^* values are associated with the high velocity gradients adjacent to the trailing vortices. Conversely, at spanwise locations distanced from the trailing vortices, such streaks of high Π^* are absent, a consequence of the lack of steep velocity gradients. From the analysis and observations presented above, it is concluded that the trailing vortices emanating from the VGs break down when subjected to an adverse pressure gradient at approximately $x/H = 2, z/H = 2$. This breakdown results in increased TKE production, which spreads in both the spanwise and wall-normal directions, thereby enhancing momentum redistribution.

In this paper, the momentum transfer resulting from velocity fluctuations and the consequent TKE production is specifically termed turbulent momentum transfer, as it pertains solely to turbulent flows. It is understood that controlling flow separation entails energizing the near-wall fluid to withstand adverse pressure gradients.

Within the context of passive flow control, two modes of momentum transfer can be distinguished: 1) the downwash stemming from streamwise vortices generated by VGs (mode-1); and 2) turbulent momentum transfer in the wallnormal direction, attributed to vortex breakdown and the subsequent amplification of TKE production (mode-2) [124]. Given the orientation of the VGs, a downwash occurs in the channel between the vanes, leading to a flowfield dominated by downwash near the plane of symmetry of the domain. Consequently, the influence of mode-1 momentum transfer is more pronounced towards the plane of symmetry. Additionally, mode-2 momentum transfer resulting from vortex breakdown near $z/H \approx 2$ complements mode-1 in mitigating flow separation. Figure 5.11 shows the time-averaged size of the separation region at various spanwise stations, with iso-lines of $\bar{u} = 0$ marking the extent of the separation region. Improved separation control was achieved at $z/H \approx 0$, as evidenced by the reduced size of the separation region.

It is evident from this work that both mode- 1 and mode- 2 momentum transfers play crucial roles in controlling flow separation. Superior separation control was achieved at the mid-span (Fig. 5.11), suggesting the dominance of mode- 1 in the downwash-affected region. The peak Π^* value remains consistent across all spanwise locations (Fig. 5.19), indicating that mode-2 momentum transfer is equally effective throughout. The authors suggest that to gain further insights into the physics of flow separation control, decoupling and separate analysis of mode-1 and mode- 2 are necessary to quantify their individual contributions to total momentum transfer.

5.4.4 Summary

The flowfield downstream of a pair of vane-type VGs in an asymmetric diffuser was studied using LES. The presence of VGs significantly modified the downstream flowfield, making it highly three-dimensional. Iso-surfaces of the Q-criterion and

streamlines on the transverse planes were used to visualize the CVP emanating from the VGs. This CVP induced downwash in the channel between the vanes and energized the near-wall flow near the plane of symmetry. Compared to the uncontrolled flow in the baseline case, the separation region near the plane of symmetry was notably reduced. Using the streamlines on the transverse planes, an increase in the vortex size was observed at a streamwise location $2H$, providing preliminary evidence of vortex breakdown. Vortex breakdown is typically accompanied by a significant increase in vortex size. Upon tracking the vortex size at different streamwise locations, increases of 100% and 67% in the horizontal and vertical extents, respectively, were observed at a streamwise location of $2H$. The approximate streamwise and spanwise locations of the vortex breakdown were thus identified as $x/H \approx 2$ and $z/H \approx 2$. The presence of vortex breakdown increased velocity fluctuations near the breakdown location, resulting in an amplification of Reynolds stress and TKE production.

Two modes of momentum transfer were identified in this study: 1) the downwash from the streamwise vortices emanating from the VGs, termed mode-1, and 2) the turbulent momentum transfer in the wall-normal direction due to the vortex breakdown and the associated increase in TKE production, termed mode-2. While mode-1 was dominant in the channel between the vanes, mode- 2 was dominant at all spanwise locations. It was observed that better separation control was achieved at locations where mode-1 was dominant, particularly at the mid-span plane. Of the two modes, mode-1 appeared to have a greater impact on flow separation control.

CHAPTER 6

SUMMARY AND FUTURE WORKS

6.1 Summary

Flow separation and secondary flows pose significant concerns in internal flows, such as those in curved diffusers used in aircraft. These phenomena can lead to poor pressure recovery and flow distortion. Passive flow control devices, such as vortex generators (VGs), have proven effective in mitigating these issues. However, the literature review reveals that understanding the physical mechanisms related to flow separation control remains insufficient. This study aims to deepen the understanding of the underlying flow physics associated with VG-induced flow separation control in internal flows. For this purpose, a well-documented asymmetric diffuser with a half-height of $H = 0.0075$ m, which exhibits mild flow separation, was selected.

The theoretical framework of this study utilizes the three-dimensional, incompressible conservation equations of mass and momentum, numerically solved across the computational domain via a finite-volume approach. Two turbulence models were employed: 1) SST $k - \omega$ based Reynolds-averaged Navier-Stokes (RANS) simulations, noted for their effectiveness in predicting flow separation, were applied for performance evaluation, and 2) dynamic Smagorinsky-Lilly model-based large eddy simulations (LES), appropriate for wall-bounded flows, were used to examine flow physics. The gradients in the flowfield were assessed using a least square cell-based method. Spatial discretization is achieved using a second-order upwind scheme for inviscid fluxes, and a bounded central differencing scheme for viscous fluxes. Results from both the RANS and LES approaches were validated against existing literature.

The first part of this study, utilizing RANS, analyzes the effects of VGs on flow separation control. Subsequently, an in-depth investigation using LES explores the breakdown of trailing vortices emanating from the VGs and their role in controlling flow separation.

In the first part of the study, the profiles of velocity, surface pressure, and skin friction in the bare diffuser (no VG) were validated against existing experimental and LES data. Despite a slight overprediction of the separation region size, good agreement with the reference data was achieved. To mitigate flow separation and improve pressure recovery, twelve VG configurations were considered, categorized into three types: 1) swept ramp (R), 2) a pair of vanes with upwash between them (Vu), and 3) a pair of vanes with downwash between them (Vd). Each type was subdivided into four sizes. These VGs were deployed upstream of the diffuser inlet. Analysis of skin friction lines (limiting streamlines) in the downstream flowfield revealed varied topological features depending on the VG type and size, which helped identify separation and reattachment locations and determine the separation region size. While ramp-type VGs reduced the separation zone, they inadequately reduced total drag and an increase in the ramp size led to excessive flow blockage, raising device drag. Upwash vanes consistently underperformed in distortion index and diffuser efficiency across all cases. Conversely, downwash vanes Vd3 (height of $0.2H$) and Vd4 (height of $0.4H$) decreased the distortion index by 21% and 46%, respectively, without impacting total drag. Despite being similarly scaled to the ramps, these vanes presented less flow resistance due to the spaces between them, explaining their slight advantages in drag reduction.

In the second part of the study, a high-performing vane pair, Vd3, was selected from the RANS study. Four LES-based simulations were conducted: 1) straight channel without VGs, 2) straight channel with VGs, 3) diffuser without VGs, and 4)

diffuser with VGs. The downstream flowfield was probed at several locations near the curved wall and along the vertical centerline of the diffuser. Turbulence events at these sites were analyzed using the normalized joint probability density function, which indicated highly three-dimensional flows induced by VGs. Comparative studies were conducted to assess the VGs' impact on turbulence under different conditions. In zero pressure gradient conditions (Cases 1 and 2), the presence of VGs resulted in increased inward and outward interaction events near the trailing vortices. Under adverse pressure gradients (Cases 3 and 4), increased ejection and sweep events were detected near the trailing vortices with heightened sweep events occurring at $x/H \approx 2$ and $z/H \approx 2$, enhancing momentum redistribution and energizing the near-wall flow to prevent flow separation.

Visualizations using iso-surfaces of the Q-criterion and streamlines on transverse planes highlighted the downwash and energized near-wall flow induced by the VGs, demonstrating a notable reduction in the separation region near the plane of symmetry. Additionally, a drastic increase in vortex size at $x = 2H$ suggested the onset of vortex breakdown, which was confirmed by tracking the vortex size at various streamwise locations. This tracking revealed increases of 100% and 67% in horizontal and vertical extents, respectively, at $x = 2$H. The breakdown location, approximately at $x/H \approx 2$ and $z/H \approx 2$, exhibited increased ejection and sweep events, velocity fluctuations, Reynolds stress, and turbulent kinetic energy (TKE) production. The peak TKE production shifted transversely and spanwise toward high-momentum regions, aiding in the suppression of flow separation through enhanced momentum redistribution. Two momentum transfer modes were identified: mode-1, characterized by downwash from streamwise vortices, and mode-2, involving turbulent momentum transfer due to vortex breakdown. Mode-1 was predominant in the channel between

vanes and most effective at controlling separation, particularly at the midplane, while mode-2 provided supplementary support across all spanwise locations.

6.2 Recommendation for Future Work

This study captured essential details about the underlying flow physics of VG-induced flow separation control, including vortex breakdown and its effects. Employing a finer grid resolution could further enhance the capture of flow features downstream of the VGs. The instantaneous velocity data collected at various probe locations downstream of the VGs were used to analyze the turbulence activity. Future work could utilize this dataset for a space-time cross-correlation study to gain deeper insights into the highly unsteady flowfield downstream of the VGs.

As discussed by Sarpkaya [49, 53], vortex breakdown modes include spiral, double helix, and bubble, with bubble being the strongest and spiral the weakest. Intense breakdowns can lead to significant velocity fluctuations and increased TKE production, which, as noted in Chapter 5, aid in suppressing flow separation. A stronger breakdown of the counter-rotating vortex pair (CVP) requires a larger adverse pressure gradient, although high gradients can also enhance flow separation and potentially inhibit vortex breakdown, as observed by Sarpkaya [2]. Therefore, an optimal range of adverse pressure gradients likely exists for each VG configuration to effectively promote CVP breakdown. Future studies should explore adjusting the diffuser divergence angle to pinpoint this range and further examine how different breakdown modes impact flow separation control to deepen the understanding of the associated flow dynamics.

REFERENCES

[1] G. Tanguy, D. G. MacManus, and E. Garnier, "Numerical investigation of the unsteady distortion for an s-duct intake with mechanical vortex generators," *International Journal of Heat and Fluid Flow*, vol. 95, p. 108975, 2022.

[2] G. Harloff, B. Reichert, and S. Wellborn, "Navier-Stokes analysis and experimental data comparison of compressible flow in a diffusing s-duct." NASA-TM-105683, 1992, p. 2699.

[3] M. O. L. Hansen, C. M. Velte, S. Øye, R. Hansen, N. N. Sørensen, J. Madsen, and R. Mikkelsen, "Aerodynamically shaped vortex generators," *Wind Energy*, vol. 19, no. 3, pp. 563–567, 2016.

[4] D. Barratt and T. Kim, "A banked wide-angle diffuser with application to electrostatic precipitators," *Proceedings of the Institution of Mechanical Engineers, Part A: Journal of Power and Energy*, vol. 229, no. 1, pp. 88–98, 2015.

[5] T. J. Burrows, B. Vukasinovic, A. Glezer, M. T. Lakebrink, and M. Mani, "Experimental and numerical investigation of active flow control of a serpentine diffuser," *AIAA Journal*, vol. 59, no. 2, pp. 607–620, 2021.

[6] E. Dick, "Fundamentals of turbomachines." Springer, 2015, vol. 109, ch. 2.

[7] S. Sun, L. Zhou, Y. Zhu, H. Zhu, T. Meng, and L. Ji, "PIV investigation on corner separation control in a compressor cascade based on a vortex generator," *Journal of Visualization*, vol. 27, no. 2, pp. 159–175, 2024.

[8] D. G. MacMartin, R. Murray, A. Verma, and J. D. Paduano, "Active control of integrated inlet/compression systems: initial results." Paper 2001-18275, 2001.

[9] W. B. Nicoll and B. R. Ramaprian, "Performance of conical diffusers with annular injection at inlet," *Journal of Basic Engineering*, vol. 92, no. 4, pp. 827–835, 12 1970.

[10] R. D. Joslin and D. N. Miller, *Fundamentals and Applications of Modern Flow Control*. American Institute of Aeronautics and Astronautics, 2009, vol. 231.

[11] D. Greenblatt, E. A. Whalen, and I. J. Wygnanski, "Introduction to the flow control virtual collection," *AIAA Journal*, vol. 57, no. 8, pp. 3111–3114, 2019.

[12] G. Mustafa Serdar, K. Kemal, D. Hacımurat, and A. Halil Hakan, "Traditional and new types of passive flow control techniques to pave the way for high maneuverability and low structural weight for uavs and mavs," in *Autonomous Vehicles*. IntechOpen, 2020, p. Ch. 7.

[13] R. Bur, D. Coponet, and Y. Carpels, "Separation control by vortex generator devices in a transonic channel flow," *Shock Waves*, vol. 19, no. 6, pp. 521–530, 2009.

[14] J. C. Lin, "Review of research on low-profile vortex generators to control boundary-layer separation," *Progress in Aerospace Sciences*, vol. 38, no. 4, pp. 389–420, 2002.

[15] P. R. Ashill, J. L. Fulker, and K. C. Hackett, "A review of recent developments in flow control," *The Aeronautical Journal*, vol. 109, no. 1095, pp. 205–232, 2005.

[16] J. C. Lin, S. K. Robinson, R. J. McGhee, and W. O. Valarezo, "Separation control on high-lift airfoils via micro-vortex generators," *Journal of Aircraft*, vol. 31, no. 6, pp. 1317–1323, 1994.

[17] A. Wortman, "Reduction of fuselage form drag by vortex flows," *Journal of Aircraft*, vol. 36, no. 3, pp. 501–506, 1999.

[18] W. Calarese, W. Crisler, and G. Gustafson, "Afterbody drag reduction by vortex generators." AIAA 1984-354, 1984, p. 354.

[19] R. Bevan, D. Poole, C. Allen, and T. Rendall, "Adaptive surrogate-based optimization of vortex generators for tiltrotor geometry," *Journal of Aircraft*, vol. 54, no. 3, pp. 1011–1024, 2017.

[20] L. Gao, H. Zhang, Y. Liu, and S. Han, "Effects of vortex generators on a blunt trailing-edge airfoil for wind turbines," *Renewable Energy*, vol. 76, pp. 303–311, 2015.

[21] B. Anderson, M. Shur, B. Spalart, M. Strelets, and A. Travin, "Reduction of aerodynamic noise in a flight deck by use of vortex generators." AIAA Paper 2005-0426, p. 426.

[22] A. Holmes, P. H. W. Murphy, and D. Hilton, "The application of sub-boundary layer vortex generators to reduce canopy 'mach rumble' interior noise on the gulfstream III." AIAA Paper 1987-0084, 1987, p. 84.

[23] M. Murayama, K. Yamamoto, T. Takaishi, Y. Ito, H. Ura, Y. Yokokawa, K. Tanaka, and T. Hirai, "Airframe noise reduction of flap side-edge using vortex generators." AIAA Paper 2017-4030, 2017, p. 4030.

[24] S. I. Green, "Wing tip vortices," in *Fluid vortices*. Springer, 1995, pp. 427–469.

[25] S. E. Morris and C. Williamson, "Formation of mini vortex rings arising from a vortex pair impinging on a wavy wall," *Physical Review Fluids*, vol. 2, no. 9, p. 090508, 2017.

[26] S. E. Morris and C. Williamson, "Impingement of a counter-rotating vortex pair on a wavy wall," *Journal of Fluid Mechanics*, vol. 895, p. A25, 2020.

[27] H. J. Bird, S. Otomo, K. K. Ramesh, and I. M. Viola, "A geometrically nonlinear time-domain unsteady lifting-line theory." AIAA Paper 2019-1377, 2019, p. 1377.

[28] I. A. Waitz, Y. J. Qiu, T. A. Manning, A. K. S. Fung, J. K. Elliot, J. M. Kerwin, J. K. Krasnodebski, M. N. O'Sullivan, D. E. Tew, E. M. Greitzer, F. E. Marble, C. S. Tan, and T. G. Tillman, "Enhanced mixing with streamwise vorticity," *Progress in Aerospace Sciences*, vol. 33, no. 5-6, pp. 323–351, 1997.

[29] J. Park, A. Pagan-Vazquez, J. L. Alvarado, L. P. Chamorro, S. M. Lux, and C. P. Marsh, "Characterization of tab-induced counter-rotating vortex pair for mixing applications," *Journal of Fluids Engineering*, vol. 139, no. 3, 2017.

[30] T. Leweke, S. Le Dizes, and C. H. K. Williamson, "Dynamics and instabilities of vortex pairs," *Annual Review of Fluid Mechanics*, vol. 48, pp. 507–541, 2016.

[31] H. K. Moffatt, S. Kida, and K. Ohkitani, "Stretched vortices–the sinews of turbulence; large-reynolds-number asymptotics," *Journal of Fluid Mechanics*, vol. 259, p. 241–264, 1994.

[32] G. B. Schubauer and W. G. Spangenberg, "Forced mixing in boundary layers," *Journal of Fluid Mechanics*, vol. 8, no. 1, p. 10–32, 1960.

[33] Y. Ichikawa, S. Koike, Y. Ito, M. Murayama, K. Nakakita, K. Yamamoto, and K. Kusunose, "Size effects of vane-type rectangular vortex generators installed on high-lift swept-back wing flap on lift force and flow fields," *Experiments in Fluids*, vol. 62, no. 160, 2021.

[34] O. Lögdberg, J. H. M. Fransson, and P. H. Alfredsson, "Streamwise evolution of longitudinal vortices in a turbulent boundary layer," *Journal of Fluid Mechanics*, vol. 623, p. 27–58, 2009.

[35] R. D. Mehta and P. Bradshaw, "Longitudinal vortices imbedded in turbulent boundary layers part 2. vortex pair with 'common flow' upwards," *Journal of Fluid Mechanics*, vol. 188, p. 529–546, 1988.

[36] W. R. Pauley and J. K. Eaton, "Experimental study of the development of longitudinal vortex pairs embedded in a turbulent boundary layer," *AIAA Journal*, vol. 26, no. 7, pp. 816–823, 1988.

[37] G. Godard and M. Stanislas, "Control of a decelerating boundary layer. part 3: Optimization of round jets vortex generators," *Aerospace Science and Technology*, vol. 10, no. 6, pp. 455–464, 2006.

[38] R. Sedney, "A survey of the effects of small protuberances on boundary-layer flows," *AIAA Journal*, vol. 11, no. 6, pp. 782–792, 1973.

[39] C. J. Baker, "The laminar horseshoe vortex," *Journal of Fluid Mechanics*, vol. 95, no. 2, p. 347–367, 1979.

[40] C. J. Baker, "The turbulent horseshoe vortex," *Journal of Wind Engineering and Industrial Aerodynamics*, vol. 6, no. 1, pp. 9–23, 1980.

[41] S. Gildersleeve and M. Amitay, "Vortex dynamics of a low aspect ratio cantilevered cylinder immersed in a boundary layer," *Journal of Fluid Mechanics*, vol. 901, p. A18, 2020.

[42] J. P. Jones, "The calculation of the paths of vortices from a system of vortex generators, and a comparison with experiment," Aeronautical Research Council C.P. No. 361, Tech. Rep., 1957.

[43] G. V. Lachmann, "Boundary layer control," *The Aeronautical Journal*, vol. 59, no. 531, pp. 163–198, 1955.

[44] A. C. Brown, H. F. Nawrocki, and P. N. Paley, "Subsonic diffusers designed integrally with vortex generators," *Journal of Aircraft*, vol. 5, no. 3, pp. 221–229, 1968.

[45] J. Katz and A. Plotkin, *Low-Speed Aerodynamics*, 2nd ed. Cambridge University Press, 2001.

[46] M. G. Hall, "Vortex breakdown," *Annual Review of Fluid Mechanics*, vol. 4, pp. 195–218, 1972.

[47] W. J. Grabowski and S. A. Berger, "Solutions of the Navier-Stokes equations for vortex breakdown," *Journal of Fluid Mechanics*, vol. 75, no. 3, pp. 525–544, 1976.

[48] D. Peckham and S. Atkinson, "Preliminary results of low speed wind tunnel tests on a gothic wing of aspect ratio 1.0," Aeronautical Research Council C.P. No. 508, Tech. Rep., 1960.

[49] T. Sarpkaya, "Vortex breakdown in swirling conical flows," *AIAA Journal*, vol. 9, no. 9, pp. 1792–1799, 1971.

[50] J. H. Faler and S. Leibovich, "Disrupted states of vortex flow and vortex breakdown," *Physics of Fluids*, vol. 20, no. 9, pp. 1385–1400, 1977.

[51] G. E. Treiber, "An experimental investigation of the effect of adverse pressure gradient on vortex breakdown," Doctoral Dissertation, Monterey, California. Naval Postgraduate School, 1973.

[52] O. Lucca-Negro and T. O'Doherty, "Vortex breakdown: a review," *Progress in Energy and Combustion Science*, vol. 27, no. 4, pp. 431–481, 2001.

[53] T. Sarpkaya, "Effect of adverse pressure-gradient on vortex breakdown," *AIAA Journal*, vol. 12, no. 5, pp. 602–607, 1974.

[54] J. M. Delery, "Aspects of vortex breakdown," *Progress in Aerospace Sciences*, vol. 30, no. 1, pp. 1–59, 1994.

[55] M. Escudier, "Confined vortices in flow machinery," *Annual Review of Fluid Mechanics*, vol. 19, no. 1, pp. 27–52, 1987.

[56] H. Schlichting, *Boundary-Layer Theory*, 7th ed. McGraw-Hill, 1979.

[57] G. Sovran and E. D. Klomp, "Experimentally determined optimum geometries for rectilinear diffusers with rectangular, conical or annular cross-section," in *Fluid Mechanics of Internal Flow*. Amsterdam: Elsevier, 1967, pp. 271–319.

[58] S. J. Kline, D. E. Abbott, and R. W. Fox, "Optimum design of straight-walled diffusers," *Journal of Basic Engineering*, vol. 81, no. 3, p. 321–329, 1959.

[59] A. T. McDonald and R. W. Fox, "An experimental investigation of incompressible flow in conical diffusers," *International Journal of Mechanical Sciences*, vol. 8, no. 2, pp. 125–139, 1966.

[60] P. W. Runstadler Jr, "Pressure recovery performance of straight-channel, single-plane divergence diffusers at high mach numbers," *US Army Aviation Materiel Laboratories Report*, pp. 69–56, 1969.

[61] P. W. Runstadler, Jr. and R. C. Dean, Jr., "Straight channel diffuser performance at high inlet mach numbers," *Journal of Basic Engineering*, vol. 91, no. 3, pp. 397–412, 1969.

[62] P. W. Runstadler, Jr. and F. X. Dolan, "Further data on the pressure recovery performance of straight-channel, plane-divergence diffusers at high subsonic mach numbers," *Journal of Basic Engineering*, vol. 95, no. 3, pp. 373–384, 1969.

[63] F. X. Dolan and P. W. Runstadler, Jr., "Pressure recovery performance of conical diffusers at high subsonic mach numbers," NASA CR-2299, Tech. Rep., 1973.

[64] P. W. Runstadler, Jr. and F. X. Dolan, "Diffuser data book," Creare Inc., Tech. Note 186, 1975.

[65] V. A. Sandborn and S. J. Kline, "Flow models in boundary-layer stall inception," *Journal of Basic Engineering*, vol. 83, no. 3, pp. 317–327, 1961.

[66] R. L. Simpson, "Turbulent boundary-layer separation," *Annual Review of Fluid Mechanics*, vol. 21, pp. 205–234, 1989.

[67] S. J. Kline, J. G. Bardina, and R. C. Strawn, "Correlation of the detachment of two-dimensional turbulent boundary layers," *AIAA Journal*, vol. 21, no. 1, pp. 68–73, 1983.

[68] L. Castillo, X. Wang, and W. K. George, "Separation criterion for turbulent boundary layers via similarity analysis," *Journal of Fluids Engineering*, vol. 126, no. 3, pp. 297–304, 2004.

[69] A. K. Vester, R. Örlü, and P. H. Alfredsson, "Turbulent flows in curved pipes: Recent advances in experiments and simulations," *Applied Mechanics Reviews*, vol. 68, no. 5, p. 050802 (25 pages), 2016.

[70] P. R. Bandyopadhyay and A. Ahmed, "Turbulent boundary layers subjected to multiple curvatures and pressure gradients," *Journal of Fluid Mechanics*, vol. 246, pp. 503–527, 1993.

[71] W. S. Saric, "Görtler vortices," *Annual Review of Fluid Mechanics*, vol. 26, no. 1, pp. 379–409, 1994.

[72] A. S. Lopes, U. Piomelli, and J. Palma, "Large-eddy simulation of the flow in an s-duct," *Journal of Turbulence*, no. 7, p. N11, 2006.

[73] F. M. Wang, Y. T. Chew, B. C. Khoo, and K. S. Yeo, "Computation of turbulent flow in a square duct: aspects of the secondary flow and its origin," *Computers and Fluids*, vol. 23, no. 1, pp. 157–176, 1994.

[74] E. Baydar, F. K. Lu, and J. W. Slater, "Vortex generators in a two-dimensional external-compression supersonic inlet," *Journal of Propulsion and Power*, vol. 34, no. 2, pp. 521–538, 2018.

[75] E. Baydar, F. K. Lu, J. W. Slater, and C. J. Trefny, "Vortex generators in a streamline-traced, external-compression supersonic inlet." AIAA Paper 2017-1383, 2017.

[76] J. W. Slater, "Refinement of vortex generators in a streamline traced, external-compression supersonic." AIAA Paper 2019-4423, 2019.

[77] B. C. Heberling, "Inlet vortex generator design for the x-59 low boom flight demonstrator." AIAA Paper 2020-2757, 2020.

[78] J. Li and L. Ji, "Efficient design method for applying vortex generators in turbomachinery," *Journal of Turbomachinery*, vol. 141, no. 8, 2019.

[79] B. A. Reichert and B. J. Wendt, "Improving curved subsonic diffuser performance with vortex generators," *AIAA Journal*, vol. 34, no. 1, pp. 65–72, 1996.

[80] R. K. Sullerey, S. Mishra, and A. M. Pradeep, "Application of boundary layer fences and vortex generators in improving performance of s-duct diffusers," *Journal of Fluids Engineering*, vol. 124, no. 1, pp. 136–142, 2001.

[81] A. R. Paul, P. Ranjan, V. K. Patel, and A. Jain, "Comparative studies on flow control in rectangular s-duct diffuser using submerged-vortex generators," *Aerospace Science and Technology*, vol. 28, no. 1, pp. 332–343, 2013.

[82] C. M. Velte, M. O. L. Hansen, and D. Cavar, "Flow analysis of vortex generators on wing sections by stereoscopic particle image velocimetry measurements," *Environmental Research Letters*, vol. 3, no. 1, p. 015006, 2008.

[83] J. Lin, F. Howard, and G. Selby, "Turbulent flow separation control through passive techniques." AIAA Paper 1989-0976, 1989.

[84] C. Santner, E. Göttlich, A. Marn, J. Hubinka, and B. Paradiso, "The application of low-profile vortex generators in an intermediate turbine diffuser," *Journal of Turbomachinery*, vol. 134, no. 1, 2011, 011023.

[85] T. P. Chong, P. F. Joseph, and P. O. A. L. Davies, "A parametric study of passive flow control for a short, high area ratio 90 deg curved diffuser," *Journal of Fluids Engineering*, vol. 130, no. 11, 2008, 111104.

[86] C. U. Buice, "Experimental investigation of flow through an asymmetric plane diffuser," Doctoral Dissertation, Stanford University, 1997.

[87] H.-J. Kaltenbach, M. Fatica, R. Mittal, T. S. Lund, and P. Moin, "Study of flow in a planar asymmetric diffuser using large-eddy simulation," *Journal of Fluid Mechanics*, vol. 390, pp. 151–185, 1999.

[88] J. Yang, Y. Zhang, H. Chen, and S. Fu, "Unsteady flow control of a plane diffuser based on a karman-vortex generator," *AIP Advances*, vol. 10, no. 5, p. 055314, 2020.

[89] E. M. Cherry, C. J. Elkins, and J. K. Eaton, "Geometric sensitivity of three-dimensional separated flows," *International Journal of Heat and Fluid Flow*, vol. 29, no. 3, pp. 803–811, 2008.

[90] O. Tornblom and A. V. Johansson, "A Reynolds stress closure description of separation control with vortex generators in a plane asymmetric diffuser," *Physics of Fluids*, vol. 19, no. 11, 2007.

[91] Z. Pouransari, L. Vervisch, and A. V. Johansson, "Reynolds number effects on statistics and structure of an isothermal reacting turbulent wall-jet," *Flow, Turbulence and Combustion*, vol. 92, pp. 931–945, 2014.

[92] W. H. Cabot and A. W. Cook, "Reynolds number effects on Rayleigh–Taylor instability with possible implications for type Ia supernovae," *Nature Physics*, vol. 2, no. 8, pp. 562–568, 2006.

[93] S. B. Pope, *Turbulent Flows*. Cambridge University Press, 2000.

[94] F. R. Menter, "Two-equation eddy-viscosity turbulence models for engineering applications," *AIAA Journal*, vol. 32, no. 8, pp. 1598–1605, 1994.

[95] J. Smagorinsky, "General circulation experiments with the primitive equation: I. the basic experiment," *Monthly Weather Review*, vol. 91, no. 3, pp. 99–164, 1963.

[96] M. Germano, U. Piomelli, P. Moin, and W. H. Cabot, "A dynamic subgrid-scale eddy viscosity model," *Physics of Fluids A: Fluid Dynamics*, vol. 3, no. 7, pp. 1760–1765, 1991.

[97] D. K. Lilly, "A proposed modification of the Germano subgrid-scale closure method," *Physics of Fluids A: Fluid Dynamics*, vol. 4, no. 3, pp. 633–635, 1992.

[98] F. Moukalled, L. Mangani, M. Darwish, F. Moukalled, L. Mangani, and M. Darwish, *The Finite Volume Method in Computational Fluid Dynamics*. Springer, 2016, vol. 113.

[99] L. Zhang, "Flow dynamics and scalar mixing of transverse jets into crossflows," Doctoral Dissertation, The Pennsylvania State University, 2010.

[100] R. C. Swanson and E. Turkel, "On central-difference and upwind schemes," *Journal of Computational Physics*, vol. 101, no. 2, pp. 292–306, 1992.

[101] S. Grundmann, E. L. Sayles, C. J. Elkins, and J. K. Eaton, "Sensitivity of an asymmetric 3D diffuser to vortex-generator induced inlet condition perturbations," *Experiments in Fluids*, vol. 52, no. 1, pp. 11–21, 2012.

[102] J. Samareh-Abolhassani, I. Sadrehaghighi, R. E. Smith, and S. N. Tiwari, "Application of lagrangian blending functions for grid generation around airplane geometries," *Journal of Aircraft*, vol. 27, no. 10, p. 873–877, 1990.

[103] P. J. Roache, "Perspective: A method for uniform reporting of grid refinement studies," *Journal of Fluids Engineering*, vol. 116, no. 3, p. 405–413, 1994.

[104] S. J. Kline, "On the nature of stall," *Journal of Basic Engineering*, vol. 81, no. 3, pp. 305–319, 1959.

[105] T. Wei and W. W. Willmarth, "Reynolds-number effects on the structure of a turbulent channel flow," *Journal of Fluid Mechanics*, vol. 204, p. 57–95, 1989.

[106] R. Aungier and S. Farokhi, "Axial-flow compressors: a strategy for aerodynamic design and analysis," *Appl. Mech. Rev.*, vol. 57, no. 4, p. B22, 2004.

[107] S. Abbasi, A. Pirnia, and R. Taghavi-Zenouz, "Investigation of inlet distortion effects on axial compressor performance based on streamline curvature method," *Journal of Theoretical and Applied Mechanics*, vol. 56, no. 4, pp. 1005–1015, 2018.

[108] M. Tobak and D. J. Peake, "Topology of three-dimensional separated flows," *Annual Review of Fluid Mechanics*, vol. 14, no. 1, pp. 61–85, 1982.

[109] L. C. Squire, "The motion of a thin oil sheet under the steady boundary layer on a body," *Journal of Fluid Mechanics*, vol. 11, no. 2, pp. 161–179, 1961.

[110] G. N. Patterson, "Modern diffuser design: the efficient transformation of kinetic energy to pressure," *Aircraft Engineering and Aerospace Technology*, vol. 10, no. 9, pp. 267–273, 1938.

[111] F. K. Lu, S. E. James, and L. Zhang, "Flow separation control and performance evaluation of an asymmetric diffuser using vortex generators," *Aerospace Science and Technology*, p. 108237, 2023.

[112] C. U. Buice and J. K. Eaton, "Experimental investigation of flow through an asymmetric plane diffuser: (data bank contribution)," *Journal of Fluids Engineering*, vol. 122, no. 2, pp. 433–435, 2000.

[113] J. M. Wallace, H. Eckelmann, and R. S. Brodkey, "The wall region in turbulent shear flow," *Journal of Fluid Mechanics*, vol. 54, no. 1, pp. 39–48, 1972.

[114] J. M. Wallace and R. S. Brodkey, "Reynolds stress and joint probability density distributions in the u-v plane of a turbulent channel flow," *The Physics of Fluids*, vol. 20, no. 3, pp. 351–355, 1977.

[115] J. M. Wallace, "Quadrant analysis in turbulence research: history and evolution," *Annual Review of Fluid Mechanics*, vol. 48, no. 1, pp. 131–158, 2016.

[116] R. J. Adrian, "Hairpin vortex organization in wall turbulence," *Physics of Fluids*, vol. 19, no. 4, p. 041301, 2007.

[117] A. Hajaali and T. Stoesser, "Flow separation dynamics in three-dimensional asymmetric diffusers," *Flow, Turbulence and Combustion*, vol. 108, no. 4, pp. 973–999, 2022.

[118] B. A. Robinson, R. M. Barnett, and S. Agrawal, "Simple numerical criterion for vortex breakdown," *AIAA Journal*, vol. 32, no. 1, pp. 116–122, 1994.

[119] C. Yao, J. Lin, and B. Allen, "Flowfield measurement of device-induced embedded streamwise vortex on a flat plate." AIAA Paper 2002-3162, 2002, p. 3162.

[120] I. Gursul and H. Yang, "On fluctuations of vortex breakdown location," *Physics of Fluids*, vol. 7, no. 1, pp. 229–231, 1995.

[121] P. Salizzoni, M. Marro, L. Soulhac, N. Grosjean, and R. J. Perkins, "Turbulent transfer between street canyons and the overlying atmospheric boundary layer," *Boundary-Layer Meteorology*, vol. 141, no. 3, pp. 393–414, 2011.

[122] H. Kim, S. Kline, and W. Reynolds, "The production of turbulence near a smooth wall in a turbulent boundary layer," *Journal of Fluid Mechanics*, vol. 50, no. 1, pp. 133–160, 1971.

[123] X. Jiang, C. Lee, C. Smith, J. Chen, and P. Linden, "Experimental study on low-speed streaks in a turbulent boundary layer at low Reynolds number," *Journal of Fluid Mechanics*, vol. 903, p. A6, 2020.

[124] M. Gad-el Hak and D. M. Bushnell, "Separation control: review," *Journal of Fluids Engineering*, vol. 113, no. 1, pp. 5–30, 1991.

BIOGRAPHICAL STATEMENT

Sandeep Eldho James was born in Kerala, India, in 1989. He received his bachelor's degree in Mechanical Engineering from Cochin University of Science and Technology in 2012 and his master's degree in Propulsion Engineering from University of Kerala in 2015. Followed by that, he worked as a Research Assistant at the Gas Dynamics Laboratory in College of Engineering Trivandrum and an Assistant Professor (ad-hoc) at Government Engineering College Idukki. He joined UTA for his doctoral studies in Fall 2017 and joined the Aerodynamics Research Center in Spring 2018 to work on the dynamics of separated flows in diffusers using vortex generators.